Effect of isoparametric grain refinement on mechanical properties and cleavage fracture toughness in high strength steels

Experimental insights into cleavage fracture

Vishnu Cheekati

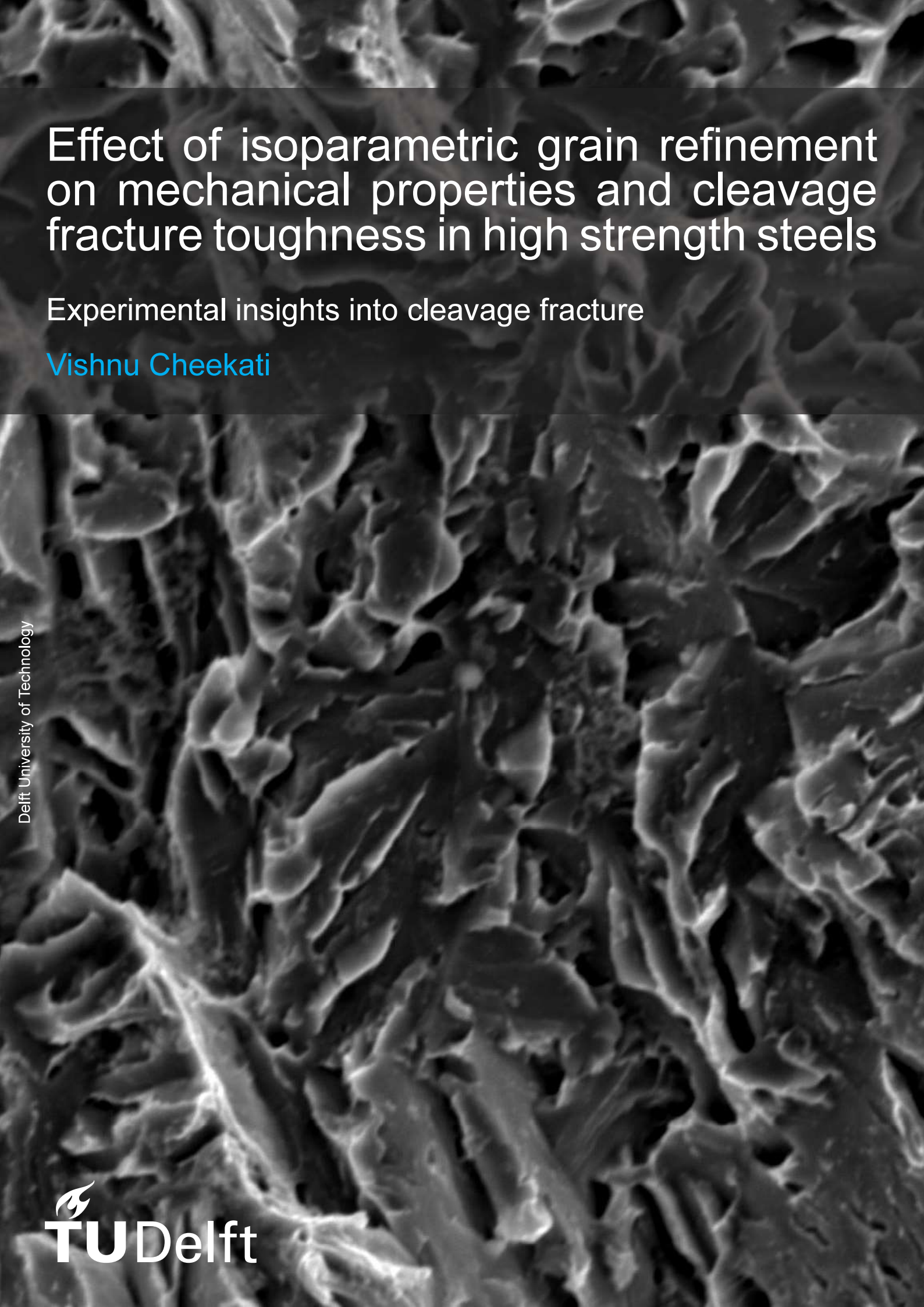

Delft University of Technology

TU Delft

DELFT UNIVERSITY OF TECHNOLOGY

MASTER THESIS

Effect of isoparametric grain refinement on mechanical properties and cleavage fracture toughness in high strength steels

---

VISHNU CHEEKATI

(4894987)

Supervisors:
Dr. V.A. Popovich
V.M. Bertolo (M.Sc)

Thesis committee:
Dr. V.A. Popovich
Dr.ir. M.J.M. Hermans
Dr. P. Dey
V.M. Bertolo (M.Sc)

to obtain the degree of Master of Science
at the Delft University of Technology,
to be defended publicly on ***Monday, 30th May, 2022***

in

Materials Science and Engineering, TU Delft

TU Delft Delft University of Technology

Abstract

In recent decades, high strength steels in thick sections have been increasingly used in offshore structures where they are subjected to harsh service conditions such as freezing temperatures and high static/dynamic loading. At these conditions they are susceptible to a transition from ductile failure to a dangerous brittle (cleavage) predominant type of failure, which occurs well before yielding. One of the main challenges in employing thick sections is the through-thickness heterogeneous variance of microstructures as a result of the processing route owing to a gradient of cooling rates from the surface to the bulk. As the material's mechanical and fracture behaviour strongly depend on the microstructure, the through-thickness microstructural heterogeneity leads to a significant scatter in mechanical and fracture properties, which makes it difficult to predict and control cleavage fracture.

From the body of literature establishing microstructural dependence on cleavage failure, several features contributing to this type failure can be identified. Phases, grain size, grain boundary misorientations and the presence of secondary phase constituents can play a major role in failure through cleavage. Additionally, cleavage failure is also sensitive to the crack depth to width ratio (a/W). This study investigates the microstructural features contributing to cleavage failure in a 100 mm thick S690QT high strength steel plate by performing mechanical and fracture toughness tests. In order to improve mechanical properties and cleavage fracture toughness, an isoparametric study employing rapid cyclic heating with the objective of grain refinement was performed.

The steel plate has coarser prior austenite grain (PAG) sizes, and a larger area and number fraction of inclusions in the middle section. Additionally, segregation bands as a result of solute segregation during the solidification process were observed to be dispersed throughout the middle section. The middle section was also characterized by lower hardness compared to the top section. The detrimental effects of the middle section were evidenced by inferior low temperature tensile properties and cleavage fracture toughness. This was attributed to the larger PAG sizes, larger area and number fractions of inclusions, and segregation bands in the middle section. The specimen orientation with respect to the rolling direction was found to have no effects on the tensile properties. Additionally, different a/W geometries and notch orientations with respect to the rolling direction were used to investigate the role of constraint effect and rolling orientation, respectively, in the fracture behaviour. Shallow-notched specimens representative of the defects found in offshore structures demonstrated a higher fracture toughness than the deep-notched specimens. This was attributed to lower hydrostatic stresses at the crack tip, which reduces stress triaxiality. The isoparametric study resulted in average grain size reduction by 41% and proved to improve micro-hardness, low temperature tensile properties and cleavage fracture toughness by 5%, 13% and 41% respectively. Fractographic analysis on the fracture toughness specimens revealed the presence of O, C-rich regions which are known to promote brittle behaviour.

Keywords: High strength steel, cleavage fracture toughness, crack tip opening displacement, grain size, segregation bands, inclusions, isoparametric grain refinement, gleeble

Acknowledgements

My deep gratitude goes first towards Dr. Vera Popovich who expertly guided me through my master thesis. Vera, the moment I attended your course on the science of failure I knew I wanted to work with you. Your ability to impart constant encouragement, while providing enough freedom was inspiring. I would also like to thank you for your generous support in matters outside my master thesis. Special thanks goes towards Virginia Bertolo, whose invaluable support as part of her PhD not only served as guidance on a daily basis, but also forged a good friendship. I appreciate the talks we had comparing similarities between Brazil and India (sorry for all the weekends I kept you busy with my work!).

I would also like to express my sincere gratitude towards the very friendly, yet professional technicians at the laboratories in the department of Materials Science and Engineering. Ton Riemslag and Hans Hofman, you made sure you were available for me even through your busy schedules, and provided crucial solutions to my rather challenging experiments. The conversations I had with you regarding the Dutch will go a long way in helping me live comfortably in the Netherlands. Special thanks goes towards Elise Reinton, Sander van Asperen, Remko Seijffers, Nico Geerlofs and Sean Scott for allowing me to use equipment on short notice. Huge thanks to Niels Troost helping design a method to convert the tensile cross-head displacement to extensometer strains. You saved me from repeating a lot of low-temperature experiments which always froze my hands! Quanxin Jiang, thank you for your assistance with quantification of inclusions and also for providing a listening ear when my experiments went wrong.

A huge thanks to counsellor Evert Vixseboxse. You helped me get through my darkest days and went out of your way to provide support to help me graduate. Special thanks to all my close friends in Delft for all the late nights and laughs which will be cherished. The lockdown period was certainly a lot easier. Lastly, thanks to my parents for their unending support during my study. You believed in me during times where I did not believe in myself.

Vishnu Cheekati
Delft, May 2022

Contents

List of Figures

List of Tables

List of Abbreviations

HSS	**H**igh **S**trength **S**teel
QT	**Q**uenched and **T**empered
CMS	**C**onventional **M**ild **S**teel
BCC	**B**ody **C**entered **C**ubic
HCP	**H**exagonal **C**losed **P**acked
DBT	**D**uctile to **B**rittle **T**ransition
CTOD	**C**rack **T**ip **O**pening **D**isplacement
DBTT	**D**uctile to **B**rittle **T**ransition **T**emperature
M-A	**M**artensite - **A**ustenite constituents
CE	**C**arbon and **E**quivalent
N	**N**ormalized
TMCP	**T**hermo-mechanical **C**ontrol **P**rocess
TMCR	**T**hermo-mechanical **C**ontrol **R**olled
TRIP	**T**ransformation **I**nduced **P**lasticity
HAZ	**H**eat **A**ffected **Z**one
PAG	**P**rior **A**ustenite **G**rain
AWS	**A**merical **W**elding of **S**ociety
ASTM	**A**merican **S**ociety for **T**esting and **M**aterials
ISO	**I**nternational **S**ociety of **S**tandards
SEN(B)	**S**ingle **E**dge **N**otched **B**end
EBSD	**E**lectron **B**ackscatter **D**iffraction
XRF	**X** **R**ay **F**luorescence
EDS	**E**nergy **D**ispersive X-Ray **S**pectroscopy
IPF	**I**nverse **P**ole **F**igure

Chapter 1

Introduction

1.1 Introduction

In the offshore industry, structures are continually subjected to harsh service conditions such as freezing temperatures, corrosive environments and dynamic loading rates due to huge masses of moving water. In order for these structures to remain safe for operation, the use of thick sections (> 60 mm) is becoming popular. Thick sections may affect the static strengths, buckling behaviour and performance at low temperatures of a certain grade of steel [1]. Therefore, not any grade of steel can be used in thick sections because careful attention must be paid to the mechanical properties such as toughness and strength, and metallurgical properties such as the microstructure [2].

Traditionally, offshore structures were constructed with moderate strength steels (up to 350 MPa) produced by normalizing. However, over the last couple of decades there has been a significant growth in the offshore industry in the use of high strength steels (HSS) due to their excellent combination of properties such as high strength, good toughness and weldability [3]. HSSs are typically quenched and tempered (QT) steels with exceptional formability and machinability. Due to these characteristics, they are being used in not only offshore applications but also in the automotive industry [4]. HSSs are complex materials with multi-phase microstructures resulting from carefully selected chemical compositions and precisely controlled heating and cooling cycles within the processing route [5]. The yield strengths of HSSs typically range between 500 MPa to 700 MPa, although some advanced grades possess strengths over 900 MPa. Figure 1.1 shows the typical performance of a HSS compared to a conventional mild steels (CMS). An advantage HSSs offer over CMSs is that for a specified CMS application, a HSS may be employed with comparable strength but lower weight [6].

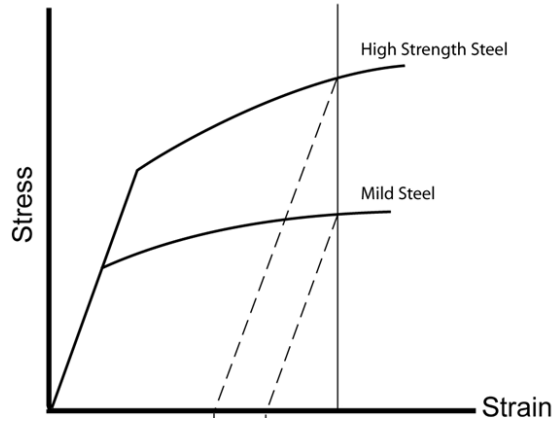

FIGURE 1.1: Mechanical performance of high strength steel and conventional mild steel [7]

One of the benefits of HSSs is their capability to be used in a wide variety of applications ranging from small-scale parts used in pumps, to large scale components in offshore applications. HSSs produced by the QT processing route have traditionally been used offshore in mobile jack-up drilling rigs which do not stay permanently on station and are free to float [3]. Therefore, these structures are subjected to dynamic loading rates. This calls for the use of thick sections to adhere to mechanical demands. They are also extensively used in construction applications such as demolition elements in jaw crushers and dumper-truck chassis. Figure 1.2 shows the typical applications of HSSs.

(A) (B) (C) (D) (E)

FIGURE 1.2: Applications of high strength steels in industrial structures [8] (A) jack-up oilrig legs (B) dumper-truck chassis (C) jaw crusher (D) boom of mobile cranes (E) crawler cranes

1.2 Challenges

It is understood that HSSs possess a good combination of properties due to their complex multi-phase microstructures. When a thick section HSS is produced, the cooling rates on the surface are different than that in the bulk of the material. This creates a gradient of cooling rates which results in varying microstructures through the thickness of the section. Another issue with these thick section steels is the presence of segregation bands in the mid-section, which may be detrimental to fracture properties of the steel [9, 10]. These centreline bands are formed the preferential segregation of certain alloying elements due to their limited solubility in solute [11]. Studies have shown that the toughness of a thick sections is typically higher at the surface of the steel due to finer grains with larger frequency of high-angle misorientation, which is favorable in enhancing deformability [12]. It has been reported that these inhomogenous microstructures lead to a large degree of variability in mechanical properties across the thickness of a HSS [10]. This ultimately raises the question on how

reliable these materials are for thick section applications, especially at low temperatures where HSSs are known to transition towards failure dominated by cleavage.

A major issue with HSSs is the ductile to brittle transition (DBT) behaviour with reduction in temperature. This is particularly of concern when HSSs are employed in offshore applications where the ambient temperatures drop below subzero. Some of these offshore structures are located in arctic environments where the temperatures may reach well below -70 °C. The transition is characterized by a significant decline in the energy absorbed before failure. The mechanism of fracture changes from plastic blunting and tearing (ductile) at higher temperatures to cleavage (brittle) at lower temperatures [3]. Metals with body centered cubic (BCC) and hexagonal close packed (HCP) crystal structures possess limited slip systems available at low temperature, minimising the plastic deformation during the fracture process [13]. Increasing temperature allows more slip systems to operate, yielding general plastic deformation to occur prior to failure [14]. Figure 1.3 shows an illustration of the variation of toughness of a steel with crack tip constraint, loading rate and temperature during DBT. The S shaped curve can be visualised as two shelves, a lower shelf attributed to cleavage failure and an upper shelf attributed to ductile failure. It is seen that an increase in loading rate shifts the curve towards the upper shelf, which results in increased DBTT. A reduction in the crack tip constraint will shift the curve towards the lower shelf, which results in reduced DBTT. However, DBTT is not an invariant property of a steel, even for a specified chemical composition and grain size. Microstructural features such as grain size, phases, inclusions and segregation bands strongly influence cleavage fracture. Studies have shown that the refinement of grains through rapid cyclic heat treatments can result in improved toughness and ductility [15, 16]. External features such as loading rate and stress state (depends on size and geometry of the steel) influence the DBT behaviour of HSSs and consequentially, the DBTT [3]. Therefore, simply operating at a temperature above the DBTT does not automatically guarantee the avoidance of brittle fracture in a structural component.

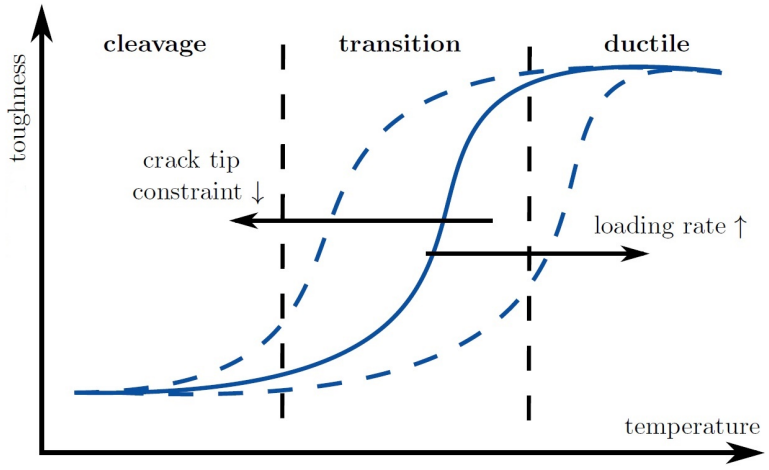

FIGURE 1.3: Variation of toughness of a steel with crack tip constraint, loading rate and temperature [14]

1.3 Research goals

The applications of HSSs may be somewhat limited due to the challenges they present. Based on literature, the microstructure and temperature were found to have a profound effect on cleavage failure. In the present study, a thick sectioned quenched and tempered HSS designated as S690QT was used. The through-thickness microstructural variation was investigated and mechanical tests in the top and middle section were performed in the lower shelf. An isoparametric study was carried out through Gleeble thermo-mechanical simulations with the aim to isolate the effect of individual microstructural features response contributing to cleavage. The chosen microstructural feature to be analysed in this work is the grain size. Fractographic analysis was performed on the fracture toughness specimens to understand the role of secondary phase constituents on cleavage fracture.

The main objectives of this study are:

1. Characterize the microstructure of the as-received S690QT HSS, and determine the tensile and fracture properties by testing at subzero temperatures.
2. Investigate the microstructural, orientation and constraint effects on cleavage failure through fracture toughness tests.
3. Perform isoparametric grain refinement to study the effect of grain size on cleavage fracture behavior.
4. Provide a basis on microstructure-cleavage fracture relationship of high strength steels for future work to improve the performance of these steels.

1.4 Structure of thesis

The subsequent contents of this thesis are divided into 6 chapters are as follows:

- Chapter 2 - Literature review: Prerequisite theories and background necessary for the definition of research objectives.
- Chapter 3 - Materials and methods: Description of the material, specimens, characterization and experimental techniques.
- Chapter 4 - Results and discussion: Microstructural characterization, mechanical properties and fracture toughness behaviour after isoparametric grain refinement.
- Chapter 5 - Conclusion: Answers the research objectives and provides recommendation for future work.
- Chapter 6 - Annex: Supplementary information

Chapter 2

Literature review

2.1 Processing routes of HSS

In general, the strength, toughness and ductility of a steel are controlled by its microstructure which varies according to its chemical composition, deformation processes involved in its production technique and its thermal history. For offshore applications, steels used are often moderate to thick sections (30 - 100 mm) and are required to be readily weldable. For this, they must possess good toughness to avoid the possibility of brittle failure as discussed in chapter 1, in addition to showing good weldability and high strength. Such a combination of properties is quite difficult to achieve because an increase in one of these properties may lead to a decrease in the other. There are a few methods of enhancing strength and toughness such as heat treatments. Moreover, increasing the carbon content (CE) and carbon equivalent (CEV) are other options [17].

HSSs may be delivered for moderate strength applications as normalized (N), or thermo-mechanical control rolled (TMCR), or thermo-mechanical control process (TMCP). At higher strength levels, there are processing thickness restrictions for TMCP steels and normalizing may not produce the strength levels required for these steels. Quenched and tempered (QT) steels are more suitable for these high-strength applications [3]. The limitations that apply to the different processing routes with respect to strength or thickness ranges are shown in Table 2.1. A commonly employed processing route for steel prior to quenching and tempering is hot rolling and is described in the following subsection.

TABLE 2.1: Steel processing routes for production of high strength steels [3]

Normalized	Usually < 460MPa for 50mm plate
Thermo-mechanical control rolled (TMCR)	Thickness restriction especially at higher strengths – usually less than 550MPa at 40mm
Accelerated cooled (TMCP)	Improved properties compared to TMCR but thickness restriction at higher strengths
Quenched & Tempered (QT)	(a) Alloyed route – no real thickness restriction but expensive and costly to weld (b) Micro-alloyed route – thickness and strengths required for offshore can be produced

2.1.1 Hot rolling

In hot rolling, the steel is rolled at a temperature higher than its recrystallization temperature which is usually above 1100 °C. At elevated temperatures, the strength of the steel is reduced. Thus the compressive force required for deformation is comparatively less and therefore smaller capacity rolling stands may be used. This is because the possible plasticity is greater at higher temperatures and the steel becomes more ductile [18]. While maintaining the temperature over 1100 °C, the steel is rolled in consecutive passes, resulting in thickness reduction [19]. A beneficial characteristic of hot rolling is that a large amount of plastic deformation may be imparted without strain hardening [20]. A prolonged effect of strain hardening renders the steel hard and brittle which makes it difficult for it to be deformed without introducing flaws or defects. Hot rolling is generally done to produce structural sections like bars, plates and sheets [20]. These are shown in Figure 2.1. However, an issue with hot rolling is that the temperature used in the rolling passes may affect the microstructure. Temperatures above the full-recrystallization temperature allow for the nucleation of new austenite grains, refining the microstructure, while temperatures below the recrystallization-stop temperature maintain the deformed austenite grains in the elongated shape. It is crucial to choose temperatures and cooling techniques to achieve the desired microstructure [21].

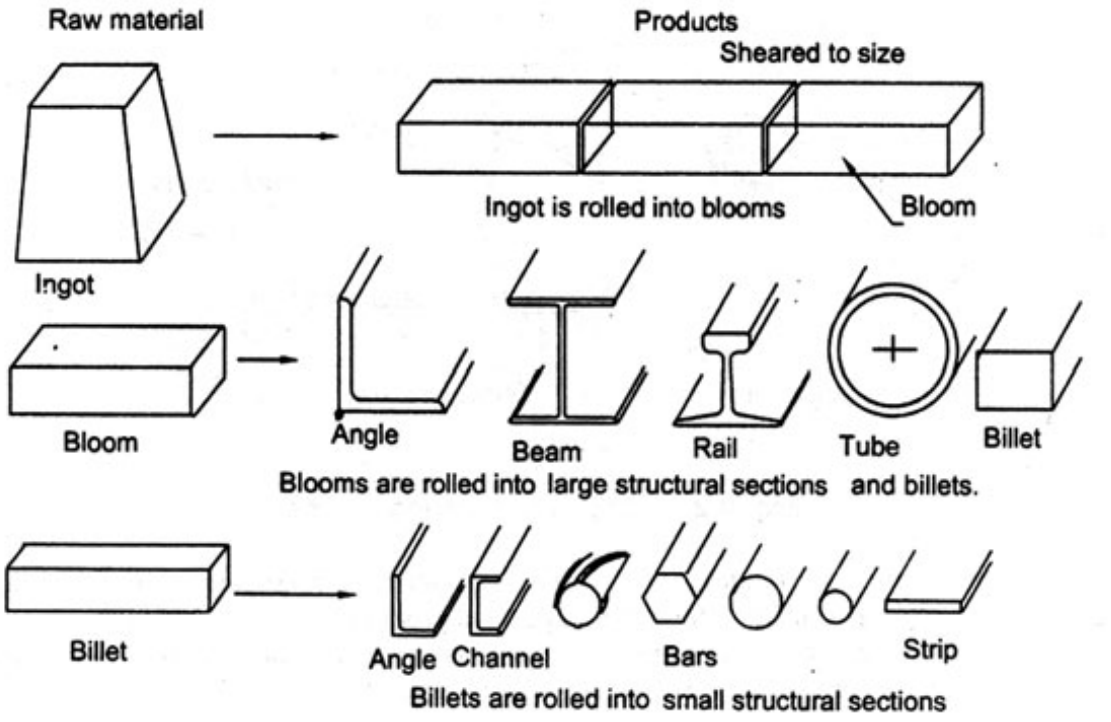

FIGURE 2.1: Geometries produced by hot rolling [20]

2.1.2 Quenching and tempering

The presence of alloying elements makes different kinds of heat treatments possible. Since HSSs are widely used in thick sections in industrial applications especially in offshore operations, quenching and tempering are the most popular heat treatment methods for the production of HSSs.

Quenching and tempering process consists of heating the material to temperatures above the austenitizing temperature for ample time to ensure the material is homogeneously austenitic through the thickness of material. Once this time has passed, the material is immediately quenched (quickly cooled), typically with water, to achieve microstructural transformation from austenite to martensite or bainite. In general, martensite is the hardest phase in steels however, it is also the most brittle phase. These are characteristics resultant from the high cooling rates during martensitic transformation. These are characteristics resultant from the high cooling rates during martensitic transformation. Due to the fast cooling process, carbon carbon diffusion is prevented and, consequently, trapped in interstitial solid solution. The microstructure of lath martensite is shown in Figure 2.2

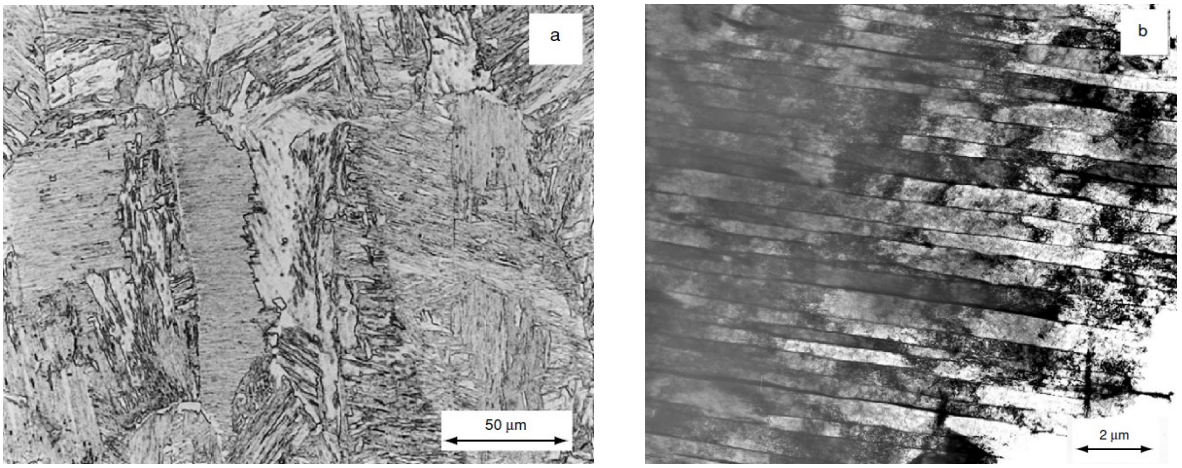

(A) (B)

FIGURE 2.2: (A) Optical microstructure of lath martensite observed in a low-carbon steel obtained by rapid cooling in a weld. (B) Transmission electron micrograph of the same microstructure showing parallel lath martensite plates with high dislocation density [22]

Tempering is a term that comes originally from the heat treatment of martensite [23]. In principle, various physical processes that lead to tempering of martensite start as soon as martensite is heated to about room temperature [24]. These processes occur in stages and are discussed below [22].

1. In the first stage of tempering (100 - 200 °C), ϵ-carbide forms from martensite. The composition of this carbide is close to $Fe_{2.4}C$. In the case of alloyed steels, the iron atoms may be replaced by other elements. After the precipitation of ϵ-carbide in stage I, the martensite is still supersaturated with carbon to certain extent and will undergo further decomposition on heating.

2. In the temperature range of 200 to 350 °C, any retained austenite in the steel decomposes into ferrite and cementite. The composition of the cementite is Fe_3C. In alloyed steels, it is referred as M_3C, where M corresponds to substitutional alloying additions (e.g. Cr, Mn) in addition to Fe. The kinetics of this decomposition are closely related to carbon diffusion in austenite. The untransformed austenite may undergo transformation on application of strain and thus, may affect the toughness of the steel. This is known as

transformation induced plasticity (TRIP). However, the fraction of retained austenite is usually low in steels containing less than 0.2 wt% C.

3. In the temperature range between 250 to 750 °C, cementite precipitates within the martensite. The nucleation of cementite may occur at ϵ-carbide and may grow by dissolution of the ϵ-carbide. With the formation of cementite, most of the carbon in martensite is removed from solid solution. Early stages of cementite growth occur only by carbon diffusion with no significant dissolution of alloying elements. However, with extended tempering, redistribution of alloying elements also occurs between ferrite and cementite.

4. Tempering at higher temperatures (> 700 °C) leads to the precipitation of more equilibrium alloy carbides such as M_7C_3 and $M_{23}C_6$. In steels containing chromium, molybdenum, vanadium and titanium, these carbides are associated with hardening of the steel that is called secondary hardening. The precipitation of these carbides also leads to the dissolution of cementite. At this stage, the recrystallization of martensite lath is more complete, and there is a tendency for the formation of equiaxed grains and extensive grain growth. The alloy carbide formation is shown in Figure 2.3.

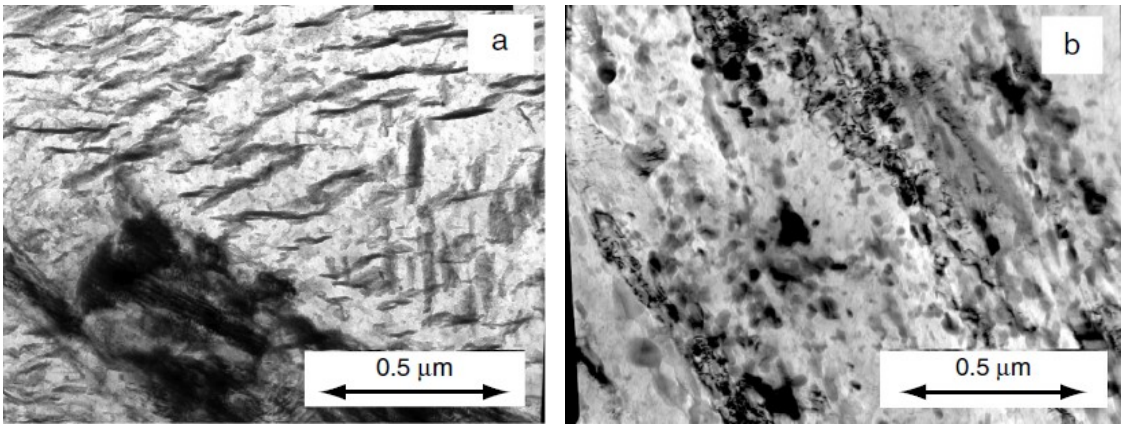

(A) (B)

FIGURE 2.3: Transmission electron micrographs of quenched and tempered steel samples. (A) After tempering at 300 °C for 2 min, showing cementite plates in a martensite lath (B) after tempering at 600 °C for 1 min, showing alloy carbides [22]

2.2 Microstructural features affecting cleavage fracture

The contents of this section describe the influence of the various microstructural features on the behavior of HSSs. It is necessary to determine the material properties of the resulting steel to validate the processing route and its different steps.

2.2.1 Grains

Grains have a strong influence on cleavage fracture of HSSs. Grains mostly influence crack propagation through size, orientation and shape. The presence of prior austenite grains (PAG) also affect the mechanical properties of steels.

2.2.1.1 Grain size

The influence of grain size on the mechanical properties of steel is commonly represented mathematically by equations which have the Hall-Petch form and is given in Equation 2.1 [25]. According to this equation the yield strength of a material increases as the grain size decreases.

$$\sigma_y = \sigma_0 + \frac{K_y}{\sqrt{d}} \tag{2.1}$$

Where σ_y is the yield stress of the material, σ_0 is the resistance stress due to dislocation motion, K_y is the stress intensity and d is the grain size.

An equation of the Hall-Petch form is also useful for predicting the DBTT [26] and is given in Equation 2.2. According to this equation the DBTT of a material reduces with decrease in grain size.

$$T_B = T_0 - \frac{K_B}{\sqrt{d}} \tag{2.2}$$

Where T_B is the DBTT, T_0 is the reference temperature for the onset of DBT, K_B is the stress intensity factor and d is the grain size.

2.2.1.2 Grain orientation

The strength of thick section HSSs is typically higher at the surface due to finer grains with larger frequency of high-angle misorientation, which is favorable in enhancing deformability [12]. During crack propagation, a crack may traverse through multiple grains and this is where high-angle misorientations are favorable. Studies have reported that the orientation of a grain boundary with respect to an advancing crack can significantly affect crack propagation through grain boundaries [27]. The effect of grain boundary angle with respect to advancing crack is shown in Figure 2.4. From the figure, it is seen that the nature of crack propagation changes from trans-granular to intergranular, with increase in grain boundary angle with respect to the advancing crack angle. Higher grain boundary orientation angle with respect to advancing crack shows more of transgranular failure while lower grain boundary angle leads to intergranular failure.

Figure 2.5 shows the crack path as a function of variation in grain boundary angle. In Figure 2.5a, crack propagations through grain boundary angles in the range of 50°– 90°is in the form of transgranular failure type. In the case of transgranular failure, deflection of crack path appears to be higher as GB angle decreases. The greater deflection indicates higher energy required for crack propagation [27]. Intergranular failure and mixed mode failure occur for GB angles with respect to advancing crack varying in the range of 10°– 40°.

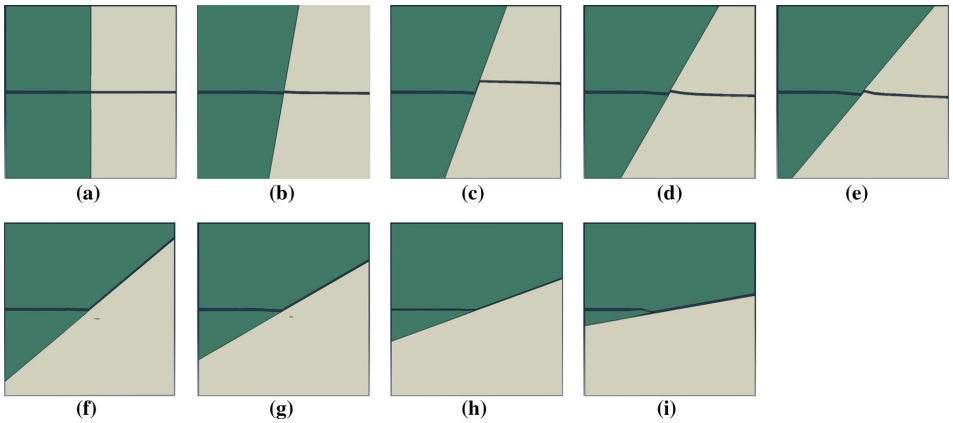

FIGURE 2.4: Effect of grain boundary angle with respect to advancing crack with orientation angle of (a) 90°(b) 80°(c) 70°(d) 60°(e) 50°(f) 40°(g) 30°(h) 20°(i) 10°[27]

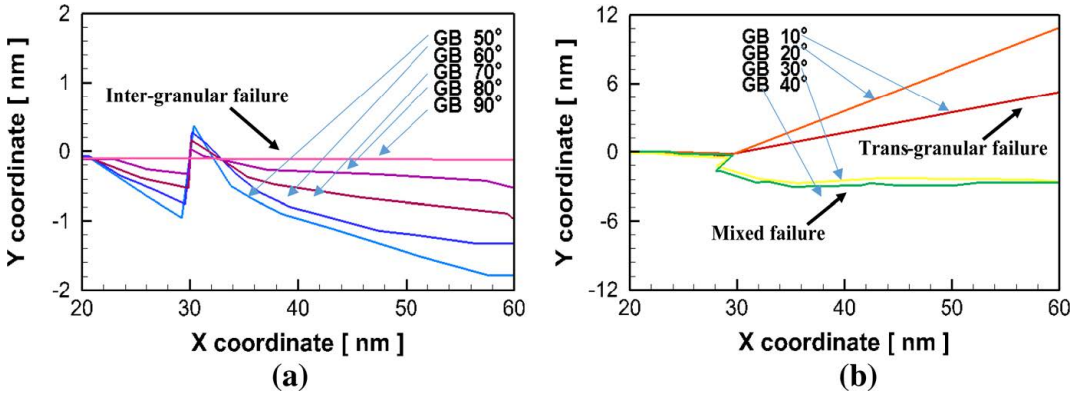

FIGURE 2.5: Crack propagation path as a function of the orientation of grain boundary in the case of (a) intergranular (b) trans-granular failure [27]

2.2.1.3 Prior austenite grains

An important feature of martensitic grains is the presence of prior austenite grains (PAG) which affect the mechanical properties of steels. PAGs may result in a transition from ductile fracture behavior to cleavage dominated failure [28]. During heat treatment of steels, austenite nucleation typically occurs at ferrite-cementite interfaces and begin to grow at these sites. During grain growth, larger austenite grains grow at the expense of smaller grains, which eventually shrink and vanish. The result is the reduction in the total number of grains and increase in the average grain size. Therefore, the austenite grain size obtained after austenitizing depends on the temperature and time of austenitization as well as the grain size and distribution of phases in the starting structure [29]. Upon quenching the austenite transforms to martensite, yet the traits of the austenite grain structures are preserved and carried over into the resulting martensite [30]. Therefore, it is essentially remnants of an austenite grain boundary structure which affects the mechanical properties of steels. Soap bubbles may be used to visualize how grains extend below the surface. A soap model and a schematic of PAG in a complex martensitic structure are shown in Figure 2.6.

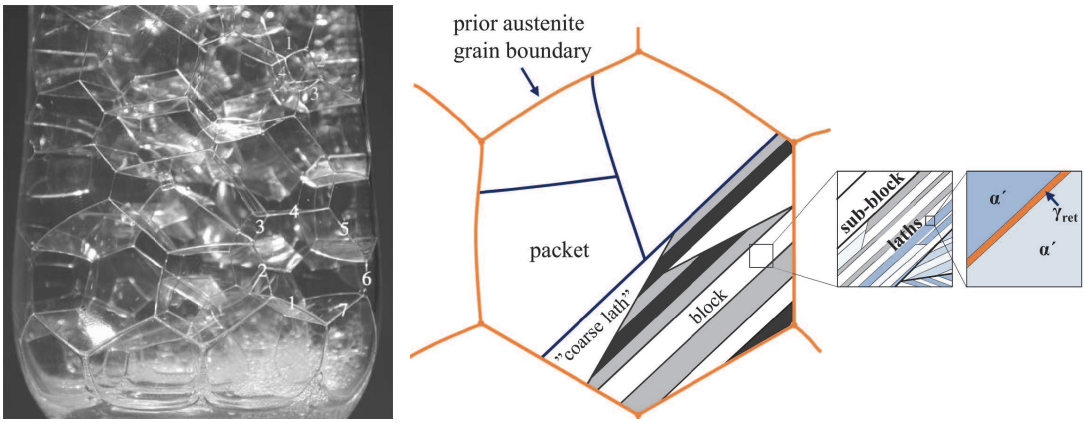

(A) (B)

FIGURE 2.6: (A) Soap model illustration of PAGs (B) Schematic of PAG in a martensite structure [30, 19]

According to Kurdjumov-Sachs (K-S) orientation relationships, there are 24 possible crystallographic relationships between parent austenite and the resulting martensite [31]. This results in four possible packets of distinctly parallel {110} α planes that each have another six possible variants of distinctly parallel directions. A packet may consist of three distinct blocks which are further divided into two sub-blocks formed of laths which are small ferritic units. Laths may be considered as highly dislocated BCC crystals that all have the same {111} γ plane in the parent austenite grain. Laths and sub-block constituents are separated by low-angle grain boundaries that have misorientations between 5°and 10.5°, respectively. Block and packet boundaries are high-angle boundaries with a misorientation of at least 15° [32].

The mechanical properties of non-tempered steels are strongly dependant on in the PAG size. Studies have verified this dependency through morphological observations [29]. Each grain consists of similar number of packets and each packet consists of similar number of blocks. Each block consists of similar number of sub-blocks, which leads to same number of laths. The consequence of these characteristics result in the formation of "barriers" towards plastic deformation and consequentially result in increase in strength. The fracture toughness of steel increases with decrease in grain size. This is due to smaller grains having a larger number of grain boundaries per unit area than larger grains and consequentially, dislocations pile up at grain boundaries and generate internal stresses [33]. Studies have shown that for steels below average grain size of 50 μm the TRIP effect from work hardening diminishes; whereas for grain sizes larger than 50 μm the TRIP effect becomes less pronounced [34]. However, the presence of PAG boundaries may be detrimental to the low temperature toughness of steels. Cold or warm working prior to intercritical annealing of these steels promotes primary recrystallization of a martensite matrix prior to reverse transformation so that the solute-segregated boundaries of the larger PAGs can be eliminated [28]. This effect is commonly referred to as the 'austenite grain boundary break-up' mechanism.

2.2.2 Secondary precipitates and inclusions

Secondary precipitates are formed due the addition of alloying elements in steel-making. The carefully controlled heat treatments allow desirable phases to form from these alloying elements. However, detrimental phases may also form which negatively influence the mechanical properties or sometimes even the corrosion resistance of the resulting steel. Inclusions find their way into steels through manufacturing processes which require certain chemicals for their function (lubricants, chemicals in crucibles) or through consumables during welding. These inclusions may be brittle and can act as stress concentrators, especially during the rolling process and may result in pre-cracks in the as-rolled steel [35]. These inclusions may consequentially act as preferential sources of crack nucleation. Therefore, it is important to study the influence of these secondary precipitates and inclusions on the microstructure and, in turn, the fracture behavior of the resulting steel.

It was seen in the previous sections that an increase in carbon content in small amounts improved the tensile strength of steel. However, all carbides found in steel are brittle and hard and may serve as crack nucleation sites [22]. Carbides are not influenced by the presence of nickel, silicon or aluminium, however, graphitization is accelerated in their presence if no other carbide forming elements are present. The carbide forming elements found in S690QT HSS are chromium, molybdenum, vanadium and titanium with the exception of iron [36].

Heat treatments influence the kinetics formation of these carbides. An increase in annealing temperature of steel results in the evolution of high-angle grain boundaries from low-angle grain boundaries. However, the fine Laves phases $(FeCrSi)_2(MoNb)$ and $(Fe,Cr)_2(Nb,Ti)$ transform to coarse carbide and nitride (Nb,Ti)(C,N) precipitates [37]. These precipitates weaken the pinning grain boundaries effect on inhibition of grain growth resulting in even larger grains with increase in holding time and consequently, decreased tensile strength. Figure 2.7 shows a schematic of precipitate formation in annealed steels.

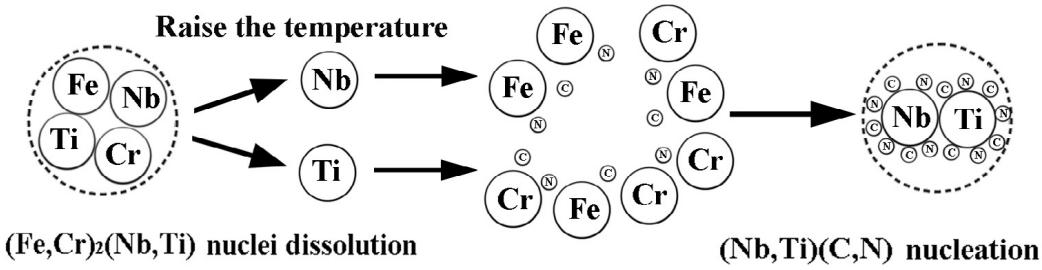

FIGURE 2.7: Schematic of precipitate formation [37]

Carbide parameters such as shape, size and distribution play an important role on the mechanical properties of the steel [38]. During heat treatment, vanadium carbides prevent rapid growth of austenite grains and result in the increase of volume fraction of secondary precipitates. The heterogeneity of vanadium concentration in the matrix may however influence the final mechanical properties of the steel [38].

Acicular ferrite is reported to be a very beneficial phase in steels due to high-angle grain boundaries, improving resistance to crack propagation. Manganese, sulphur and oxygen containing inclusions promote the formation of acicular ferrite which results in increased low temperature mechanical properties of steel [39].

Studies have shown that the presence of large niobium rich inclusions may result in a decrease in toughness. These inclusions may be dispersed as clusters and may act as stress concentrators for crack propagation [40]. These clusters were found to be very close to each other in the middle section, which aid crack propagation. The matrix/inclusion interface and inclusions were found containing cracks which may have originated from the rolling process. This means that crack nucleation will not be required for failure, and therefore, propagation is

the only stage present in the fracture process. This may be one of the contributing factors to the reduction of toughness.

Alloying elements such as titanium, niobium and vanadium are strong nitride formers, as discussed in the previous sections. They promote grain refinement through the Zener pinning effect on the grain boundaries [41]. A widely accepted Ti/N ratio for a steel is 2, or less than the general stoichiometric value 3.42. This Ti/N ratio demonstrates excellent austenite grain control through the pinning effect of grain boundaries [42]. Titanium in the microstructure can result in the promotion of formation of acicular ferrite formation. Titanium rich particles such as TiN, TiN - MnS and Ti(C,N) can be potential nucleation sites for acicular ferrite [43].

Sulphur inclusions may be introduced into steels during steel-making due to their use in crucibles. As discussed in the previous sections, these sulphurs can react with manganese to form MnS inclusions which are detrimental to the surface finish [44]. These sulphides have little or no effect on the yield strength and tensile strength in a longitudinal directions relative to non-sulphurized grades [45]. However, transverse properties are influenced by these sulphides because they introduce a large degree of anisotropy due to an elongated morphology after rolling [42].

2.2.2.1 Segregation bands

An issue with HSSs, especially in the case of thick section steels is the preferential segregation of alloying elements, particularly at the middle section of the material [11]. This phenomenon is known as centreline segregation and it occurs during the casting process due to the limited solubility of certain elements such as molybdenum, chromium and manganese in the solute [9]. A visualization of these bands is shown in Figure 2.8. A study has reported that the presence of centreline segregation bands can negatively influence the fracture toughness of steels [10]. These bands may contain inclusions which serve as nucleation sites for fracture propagation [40]. However, another study has reported that the centreline segregation phenomenon may be beneficial through grain refinement in the bands, which results in increased hardness [19].

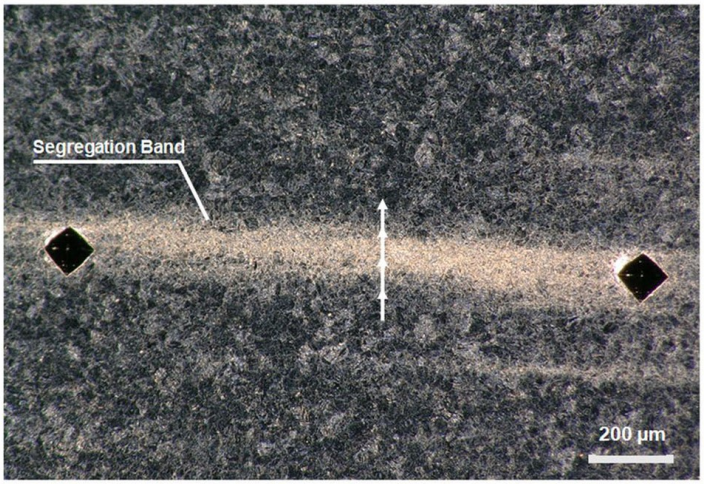

FIGURE 2.8: Segregation band in the middle section of the specimen showing reduction in grain size [40]

2.2.3 Residual stresses

In HSSs, inclusions significantly affect the material performance, especially in terms of mechanical properties [46]. Inclusions picked up during steel-making may lead to the formation of penny - shaped granular layers in the steel matrix. This could result in cracks being formed around the matrix - inclusion interface during deformation operations such as rolling [47]. It is reported that these inclusions in steels can serve as cleavage initiation sites due to large residual stresses around them [48]. Non-metallic inclusions such as Al_2O_3 are often present in steel which develops during melting of the steel, and TiN which develops during casting of the steel [49]. The residual stress distribution of a penny - shaped Al_2O_3 inclusion is shown in Figure 2.9.

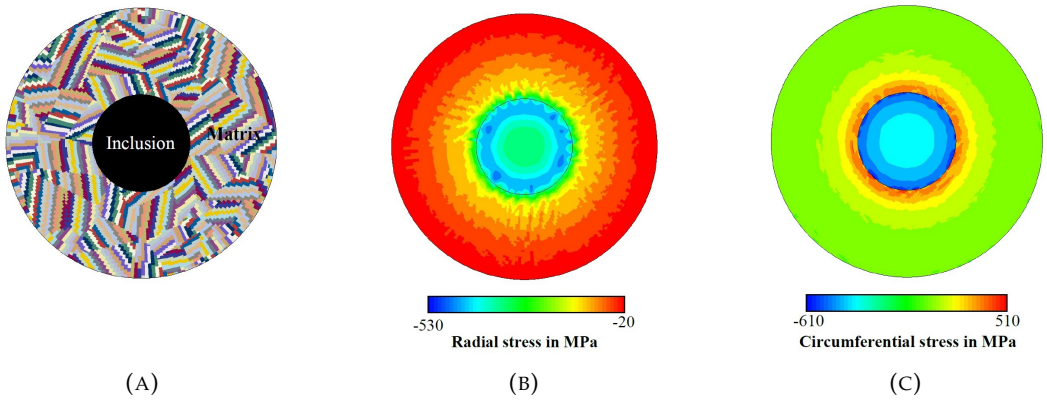

FIGURE 2.9: Residual stress distribution around Al_2O_3 in steel (A) Martensitic microstructure with embedded inclusion (B) Radial stress distribution (C) Circumferential stress distribution [46]

The chemical composition and shape of the inclusion has an effect on the residual stress distribution around the inclusion. Al_2O_3 tends to form spheres while TiN inclusions are irregularly shaped [49]. Figure 2.10 shows the residual stress distributions around different types of inclusions. It is observed that the stress fields around irregularly shaped inclusions are lower in magnitude than that of circular inclusions.

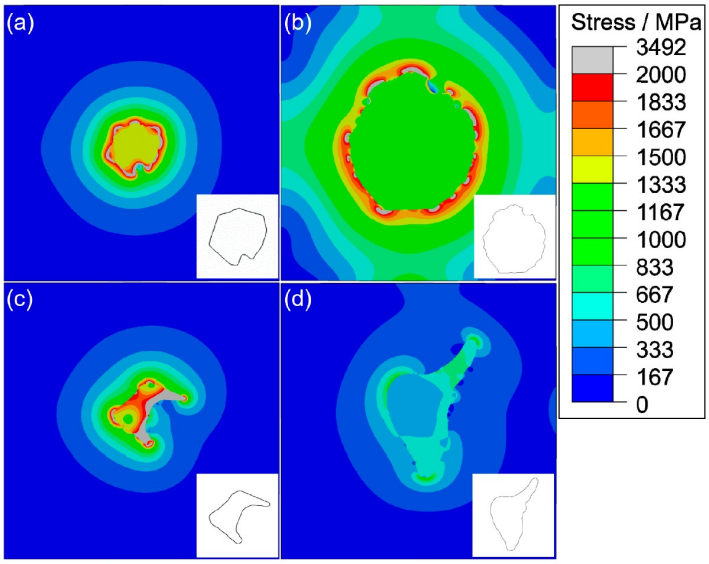

FIGURE 2.10: Residual stress distributions around the inclusions with their shapes. (A) Mg-Al-O (B) Al-Ca-O-S (C) TiN (D) MnS [49]

Inclusions are, however, not the only factors responsible for residual stresses in steels. Thermo-mechanical processes such as welding and mechanical/heat treatments may also introduce residual stresses. Residual stresses in welds originate due to a variety of stress gradients forming in and around the weld zones by solidification shrinkage. The combination of tensile and compressive stresses in the weld and HAZ result in residual stresses present in the resulting steel [50]. Figure 2.11 shows the stereogram and projection of the longitudinal residual stress distribution in a S690 HSS weld. A gradient of residual stress is observed around the weld and the magnitude of stress is larger at the weld zone.

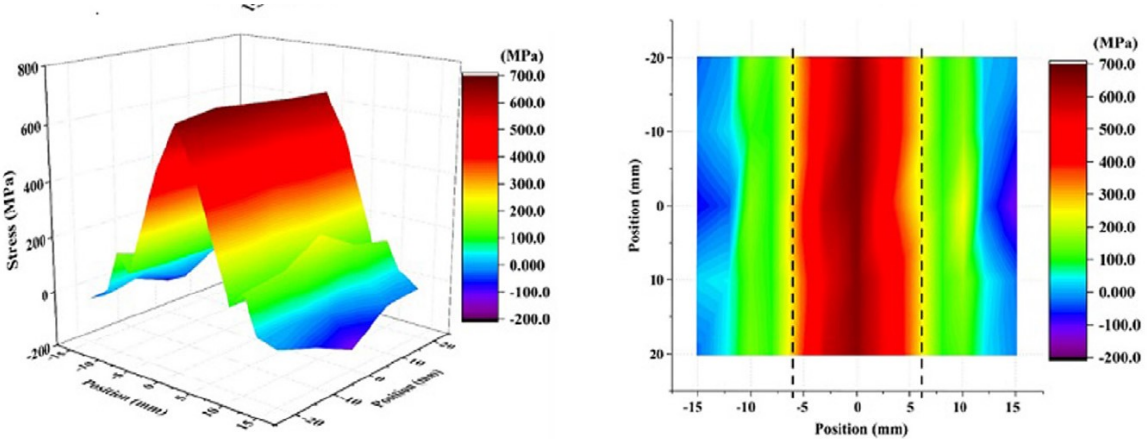

FIGURE 2.11: Stereogram and projection of the longitudinal residual stress distribution in a S690 weld [50]

2.3 Fracture mechanics

In order to understand the effects of the microstructural features discussed in this chapter on the crack initiation and propagation in HSSs, it is necessary to understand fracture mechanics in steels. Fracture mechanics is the field of mechanics concerned with the study of propagation of cracks in materials. In fracture mechanics attention is typically focused on a single crack. Analytic techniques determine whether a certain crack will propagate under a given load and if so, the speed and direction with which it will propagate. Fracture mechanics is a crucial study which is necessary to prevent failure of structures.

2.3.1 Types of fracture

The deformability of a material and mode of fracture depend on internal and external factors. Internal factors are typically metallurgical in nature such as chemical composition, microstructure, impurities (inclusions/precipitates) and residual stresses. External factors are constraints such as temperature, loading rate, stress state and stress concentrations [13]. These factors influence the mode of failure of a given specimen and result in different types of fractures.

2.3.1.1 Ductile fracture

Ductile fracture is a high energy mechanism which is caused by overload and is associated with extensive plastic deformation in the vicinity of an advancing crack. The crack propagates at a slow pace and is said to be stable because it resists any further extension unless there is an increase in the applied stress. The appearance of a ductile fracture is dull and is illustrated in Figure 2.12. Ductile fracture may or may not demonstrate contraction depending on the constraint (thickness) of the specimen [51] Specimens with little constraint will show significant amounts of contraction while specimens with high constraint typically do not show any noticeable contraction [51].

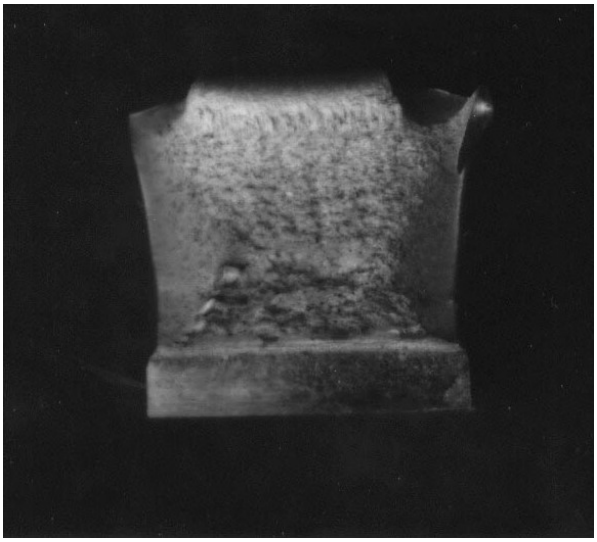

FIGURE 2.12: Ductile fracture surface of impact specimen [51]

Ductile fracture is characterized by microvoid coalescence and occurs in three stages [52]:

1. After onset of plastic deformation, cavities/voids form usually at inclusions or precipitates, in the deformed region.
2. These voids grow and it eventually leads to their coalescence into dimples resulting in formation of crack that grows outward in a direction perpendicular to the application of stress.
3. Failure involves rapid crack propagation at about 45°to the direction of the applied stress. This angle represents the direction of maximum shear stress that causes shear slip in the final stage.

The formation of dimples is reliant on the type of loading and is illustrated in Figure 2.13. Uniaxial tensile loading typically results in the formation of spherical/equi-axed dimples. Failures caused by shear will produce elongated dimples that point in opposite directions on the matching fracture surfaces. Tensile tearing also produce elongated dimples but they point in the same direction on matching fracture surfaces [51].

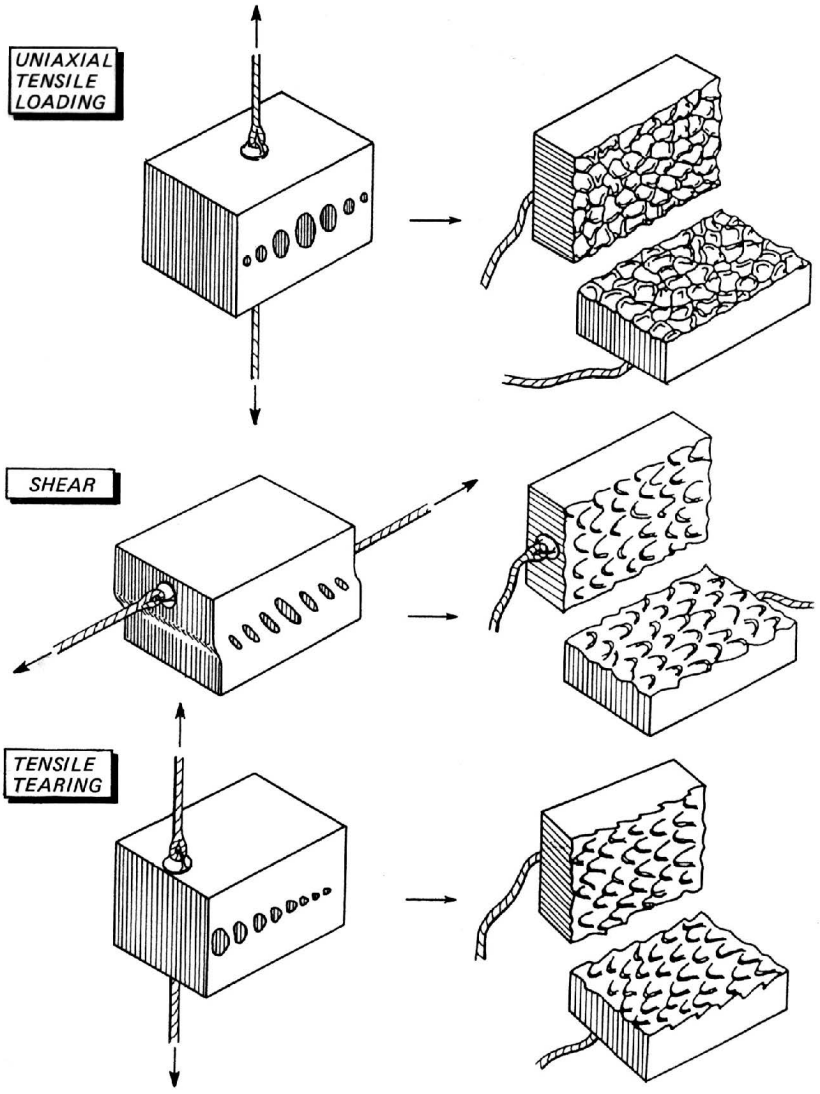

FIGURE 2.13: Dimple formation owing to uniaxial tensile loading, shear and tensile tearing [51]

2.3.1.2 Brittle fracture

Brittle fracture arises in materials which lack ductility. It is a low energy mechanism which occurs when there is restriction of plastic deformation at the crack tip. Typically, the crack travels through grains by splitting atomic bonds along lattice planes. This mechanism is called intra or transgranular cleavage. The crack is unstable and unlike ductile fracture, it propagates rapidly and will continue spontaneously without an increase in magnitude of the applied stress. Ideally, a cleavage fracture would comprise of flat, featureless perfectly matching faces. However, structural materials are poly-crystalline with grains randomly oriented. The crack that propagates through one grain may change direction as it crosses another grain which makes it shiny and faceted [51]. There is relatively little to no observable contraction in the material. The appearance of a cleavage fracture is shown in Figure 2.14.

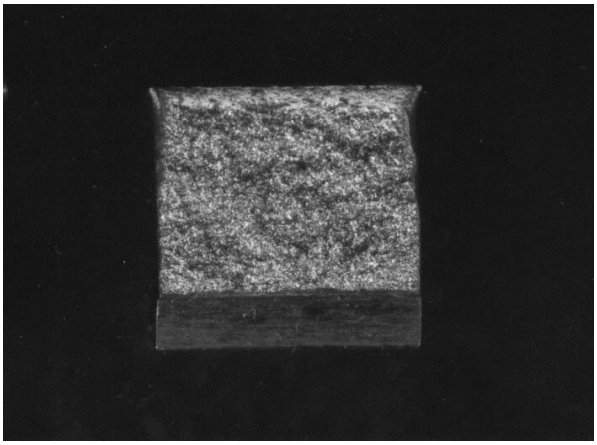

FIGURE 2.14: Brittle fracture surface of impact specimen [51].

Although cleavage is attributed to intragranular fracture, brittle fracture may also arise in an intergranular manner along grain boundaries. This mechanism occurs when grain boundaries are weakened or embrittled by grain boundary segregation of impurities such as Cr, Mo [53]. This fracture mode prevails in materials with little or no close-packed planes, having HCP or BCC structures. It is also observed when plastic deformation is limited due to low temperature or high strain rate, i.e, DBT. Figure 2.15 illustrates the types of cleavage fractures.

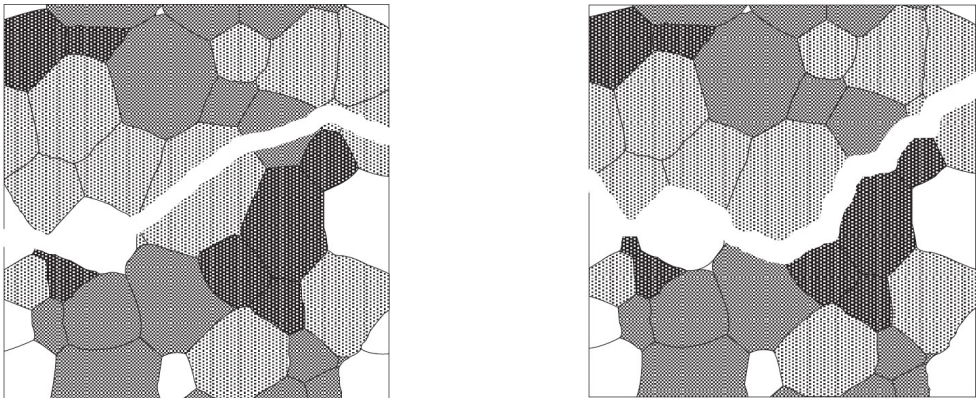

(A) (B)

FIGURE 2.15: Types of cleavage fracture. (A) intragranular (B) intergranular [54]

The process of cleavage micro-cracking is accepted to be a slip-induced process and is composed of three stages which are sequential and non-stop [55]:

1. Nucleation and extension of cleavage crack in a secondary phase particle as a result of pileup of dislocations, and the tensile stress induced by the dislocation pileup, shown in Figure 2.16a and Figure 2.16b. The criterion for this stage is:

$$\epsilon_p \geq \epsilon_{pc} \tag{2.3}$$

   Where ϵ_{p} is the plastic strain, ϵ_{pc} is the fracture plastic strain.

2. Propagation of the nucleated crack through the boundary between the particle and grain, driven by the combination of applied tensile stress and the tensile stress due to dislocation pileup, shown in Figure 2.16c. The criterion for this stage is:

$$\sigma_{yy} \geq \sigma_{f(c)} \tag{2.4}$$

   Where σ_{yy} is the normal stress, $\sigma_{\mathrm{f(c)}}$ is the local cleavage fracture stress of the secondary phase particle.

3. Propagation of the crack through grain boundaries into adjacent grains, driven by the applied tensile stress, shown in Figure 2.16d. The criterion for this stage is:

$$\sigma_{yy} \geq \sigma_{f(f)} \tag{2.5}$$

   Where σ_{yy} is the normal stress, $\sigma_{\mathrm{f(f)}}$ is the local cleavage fracture stress of the grain.

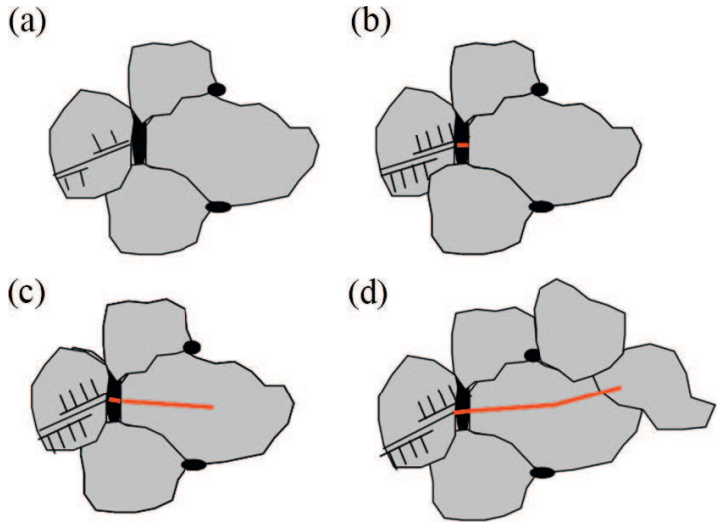

FIGURE 2.16: Schematic of the three sequential stages composing cleavage cracking on the microscopic scale. (a) and (b) nucleation and extension of a micro-crack in a second-phase particle (c) propagation of the nucleated crack into the matrix grain (d) propagation of the grain-sized crack across grains [55]

2.3.2 Fracture mechanics concepts

Fracture mechanics is commonly studied as Linear Elastic Fracture Mechanics (LEFM) and Elastic-Plastic Fracture Mechanics (EPFM). A large field of fracture mechanics uses concepts in which linear elastic material behavior is an assumption and this is the case for LEFM. Under LEFM conditions, there is limited plasticity at and around the crack tip. When there is a large plastic zone around the crack tip, the assumptions from LEFM are no longer valid and this is the case for EPFM. The materials that demonstrate this behavior are non-linear elastic (polymers, composites). Both theories are discussed in the following subsections.

2.3.2.1 Linear Elastic Fracture Mechanics (LEFM)

The initial assumption of linear elastic material behavior results in infinite stresses at the crack tip. This is the result of the cross-sectional area of the crack tip being zero. However, a material cannot exhibit elasticity while being subjected to infinite stresses at the crack tip. When the stresses at the crack tip exceed the yield strength, plastic deformation will occur in the crack tip region. The crack tip plastic zone is approximated using yield criteria (von Mises, Tresca) and when the plastic zone is very small (small-scale yielding), LEFM concepts are used [52]. Prediction of crack growth is based on an energy balance approach or a stress-based approach.

2.3.2.1.1 Griffith energy balance approach Griffith postulated that crack growth will occur when there is enough energy available to generate new crack surface [56]. Griffith performed analysis on the energy balance of an infinite plate with a through-thickness crack under stress and developed a relation for the stress required for crack propagation. This is given in Equation 2.6. The criterion for Griffith crack extension is given in Equation 2.7

$$\sigma = \sqrt{\frac{2\gamma E}{\pi a}} \tag{2.6}$$

Where σ is the applied stress, γ is the surface energy of the plate, E is the elastic modulus of the plate, a is the crack length.

$$\frac{\sigma^2 \pi a}{E} > 2\gamma \tag{2.7}$$

Irwin designated the left-hand side of Equation 2.7 as the energy release rate G, which represents the energy per unit of new crack area that is available for infinitesimal crack extension. The right-hand side of Equation 2.7 represents the surface energy increase per new crack area that would occur due to infinitesimal crack extension and is designated the crack resistance R.

The Griffith approach is only valid for very brittle materials. For materials which exhibit a certain amount of elasticity, the calculated crack resistance falls short because of surface energy being the only variable to promote crack growth [51]. The energy dissipation in the energy balance is neglected. For brittle materials, the dissipation is very low while ductile materials demonstrate large values of dissipation (G may be 10^5 times R). Therefore, the energy release rate G defined by Irwin becomes an essential quantity in energy balance criteria. The resulting crack growth criterion is referred to as being global, because a large volume of material is considered [52], and is given in Equation 2.8.

$$G = \frac{\pi \sigma^2 a}{E} \tag{2.8}$$

For crack growth to occur, it follows that G must be greater than R. If R is a constant, this means that G must exceed a critical value G_c = R.

2.3.2.1.2 Stress-based approach The assumption of linear elastic material behavior resulted in infinite stresses at the crack tip. However, a material cannot exhibit elasticity while being subjected to infinite stresses at the crack tip. This led to a stress-based approach developed by Irwin to define a stress field around the crack tip, resulting in a criterion called stress intensity factor (K) which gives the magnitude of elastic stress field [51].

Irwin also identified the standard modes of loading cracks and the resulting crack surface displacements [52]. The various modes of loading are shown in Figure 2.17.

1. Mode I is the opening mode. The stresses are normal to the crack plane and the crack surface displacements are perpendicular to the crack plane.
2. Mode II is the sliding mode. The crack tip is subjected to in-plane shear stress and the crack surface displacements are on the crack plane, perpendicular to the crack front.
3. Mode III is the tearing mode. The crack tip is subjected to out-of-plane shear stresses and the crack surface displacements are on the crack plane, parallel to the crack front.

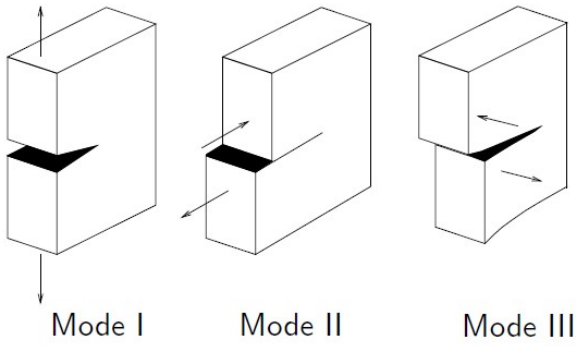

FIGURE 2.17: Standard loading modes of a crack [52]

The stress intensity factor not only depends on the applied stress, but also the geometry of the crack as well as the specimen. The relation for the stress intensity factor is given in Equation 2.9

$$K_I = C\sigma\sqrt{\pi a} \tag{2.9}$$

Where K_I is the stress intensity factor (mode I), C = f(a/W) is the geometric parameter, σ is the applied stress, a is the crack length. Crack growth occurs when the magnitude of stress intensity factor reaches a critical value. This critical value is called the critical stress intensity factor K_C [51]. For linear elastic material behavior, the relationship between G_c and K_c is given in Equation 2.10.

$$G_c = \frac{{K_c}^2}{E} \tag{2.10}$$

2.3.2.2 Elastic-Plastic Fracture Mechanics (EPFM)

When small-scale yielding can no longer be assumed, the linear elastic material behavior is no longer a valid assumption and LEFM concepts cannot be applied. The analysis of stress fields around a crack tip are carried out elasto-plastically.

The failure criterion is determined by the Crack Tip Opening Displacement (CTOD) or the J-Integral method.

2.3.2.2.1 Crack Tip Opening Displacement (CTOD) Wells developed the CTOD approach which focused on strains in the crack tip region instead of stresses, contrary to the stress intensity approach. In the presence of plasticity, a crack tip was postulated to experience blunting and is shown in Figure 2.18. The observations led to the development of the fracture parameter CTOD (δ) which is a measure of fracture toughness.

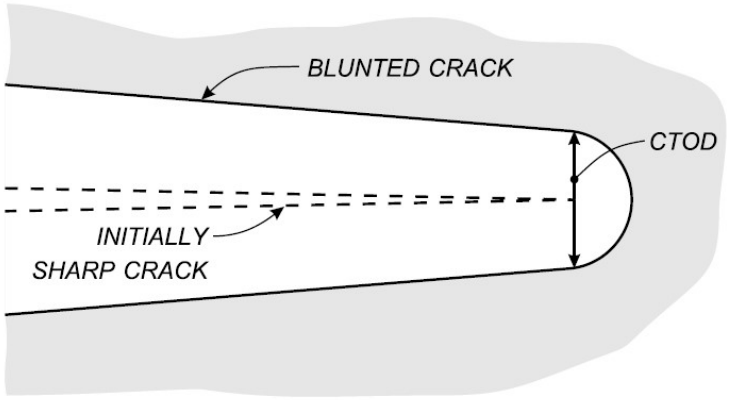

FIGURE 2.18: Crack tip opening displacement [51]

Wells suggested that the CTOD may be used in a crack growth criterion, when the plasticity at the crack tip is taken into account and the actual crack length is replaced by the effective crack length [57]. The effective crack length is the actual crack length plus the length of the plastic zone in front of the crack tip (r_y) and was initially suggested by Irwin. The Irwin correction is shown in Figure 2.19.

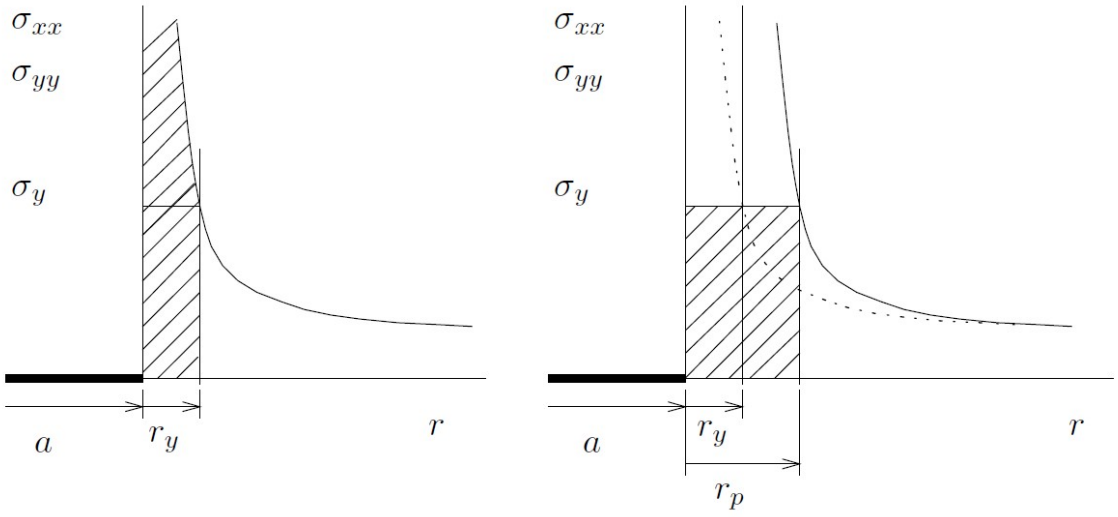

FIGURE 2.19: Irwin plastic zone correction [52]

The displacement behind the crack tip u_y is given in Equation 2.11

$$u_y = \frac{4}{E'} K_I \sqrt{\frac{r_y}{2\pi}} \tag{2.11}$$

where K_I is the stress intensity factor (mode I), r_y is the plastic zone in front of the tip and E' is the effective elastic modulus. The Irwin plastic zone correction is given in Equation 2.12.

$$r_y = \frac{1}{2\pi} \left(\frac{K_I}{\sigma} \right)^2 \tag{2.12}$$

The CTOD (δ) is evaluated as twice the displacement behind the crack tip and is given in Equation 2.13.

$$\delta = 2u_y = \frac{4}{\pi} \frac{{K_I}^2}{\sigma_{ys} E} \tag{2.13}$$

Where E is the elastic modulus of the material, K_I is the stress intensity factor and σ_{ys} is the yield stress. CTOD can also be correlated with the energy release rate G and is given in Equation 2.14 [58].

$$\delta = \frac{4}{\pi} \frac{G}{\sigma_{ys}} \tag{2.14}$$

Another method for calculating fracture is the J-integral approach, which utilizes finite element calculations for simple loads and geometries. This method will not be employed in this study.

2.4 Mechanical testing

Mechanical testing is an essential practice in order to assess the mechanical performance of steels, which demonstrates the behavior of these steels in linear-elastic and elastic-plastic regimes. A variety of experimental tests and methods for measuring parameters such as yield strength, tensile strength, and fracture toughness parameters such as impact toughness, K and CTOD exist. These parameters are determined by following standards established by international organizations such as American Welding Society (AWS), American Society for Testing and Materials (ASTM) and the International Institute of Standards (ISO). A few industrially accepted mechanical testing methods are elaborated in the following sub-sections.

2.4.1 Tensile testing

Uniaxial tensile test is a basic and universally accepted testing method to determine material parameters such as yield strength, tensile strength, elongation percentage, area reduction percentage and the elastic modulus. The test is carried out by applying a longitudinal or axial load at a specific extensional rate to a standard tensile specimens with known dimensions such as gauge length and cross sectional area until failure. The applied tensile load and resultant extension at each instant are recorded during the test for the calculation of stress and strain [59].

ASTM E8 / 8M-16a is the widely accepted standard test method for tension testing of metallic materials. The test utilises a cylindrical specimen with a reduced cross-section. Figure 2.20 shows the standard cylindrical specimen where G is the gauge length, D is the diameter, R is the filet radius and A is the length of the reduced parallel section [60]. To study the tensile properties at low temperature, modifications to the test setup must be made for steel to be tested at cryogenic temperatures. A schematic of a cryogenic tensile test setup is shown in Figure 2.21.

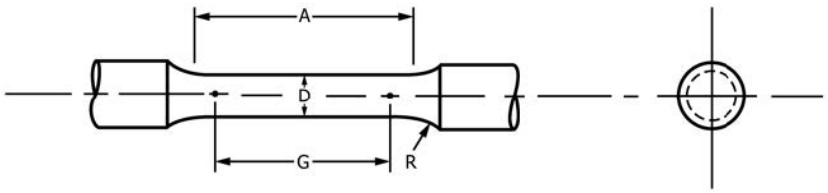

FIGURE 2.20: Standard cylindrical tensile specimen [60]

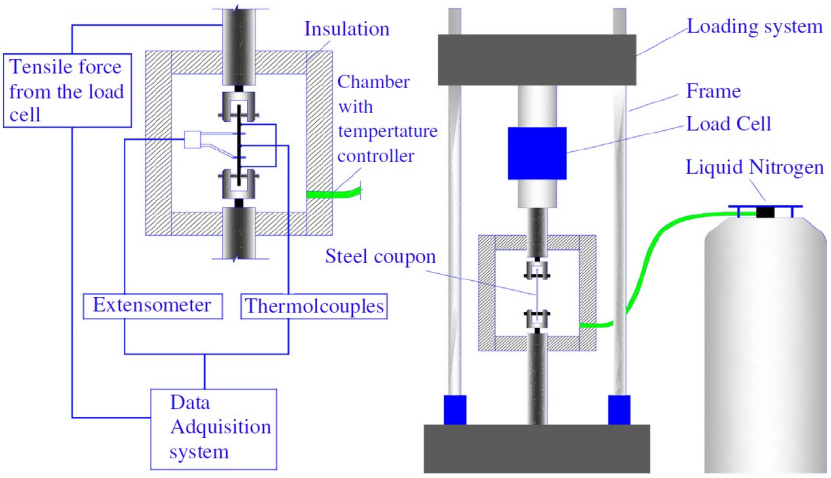

FIGURE 2.21: Schematic of a cryogenic tensile test setup [61]

2.4.2 Fracture toughness testing

A single edge notched bend (SEN(B)) test is the most commonly used fracture toughness test method. Important fracture toughness parameters such as K, CTOD and J-integral are obtained from this test. ASTM E1820 and ISO 12135 are the most widely accepted standard test methods for the measurement of fracture toughness of a material [62, 63, 64]. Figure 2.22a shows a standard three-point bend test setup.

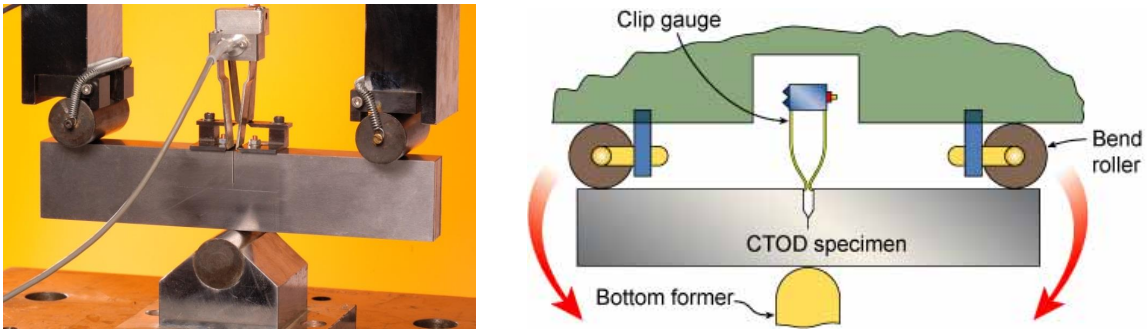

(A) (B)

FIGURE 2.22: Three-point bend test (A) Standard setup (B) Schematic the setup [62]

SEN(B) specimens are highly constrained and contain a notch with a sharp pre-crack to represent defects in metals. The high constraint means that the test results will not overestimate the actual material fracture toughness behaviour of a sharp pre-crack under typical service loading conditions [62].

In order to allow the crack to propagate in the LEFM domain, the plastic zone around the crack tip must be restricted to allow small-scale yielding. This is done by extending the notch by applying cycling loading and the result is a sharp fatigue pre-crack. The test is carried out by applying controlled loading through bend rollers. The displacement at the crack mouth is measured by a clip gauge and the CTOD is calculated from the K_I values obtained from the SEN(B) test [59]. Equation 2.15 gives the value of K_I from the SEN(B) test.

$$K_{(i)} = \left[\frac{P_i S}{(B B_N)^{1/2} W^{3/2}} \right] f\left(a_i/W\right) \tag{2.15}$$

Where the geometric parameter $f(a_i/W)$ is given by Equation 2.16:

$$f\left(\frac{a_i}{W}\right) = \frac{3\left(\frac{a_i}{W}\right)^{1/2}\left[1.99 - \left(\frac{a_i}{W}\right)\left(1-\frac{a_i}{W}\right)\left(2.15 - 3.93\left(\frac{a_i}{W}\right) + 2.7\left(\frac{a_i}{W}\right)^2\right)\right]}{2\left(1+2\frac{a_i}{W}\right)\left(1-\frac{a_i}{W}\right)^{3/2}} \tag{2.16}$$

Where P_i is the applied load, S is the span of the specimen between the cylindrical rollers, B_N is the net specimen thickness (B_N=B if no side grooves are present), W is the width of the specimen and a_i is the crack length [64].

2.5 Post-process thermo-mechanical treatments

Post-process thermo-mechanical treatments, which are not part of the processing route, are useful to perform heat treatments for research purposes. They are useful when it is not possible to use conventional heat treatments for research purposes. Thermo-mechanical simulation has been a useful development in the steel-making industry.

2.5.1 Gleeble simulator

Gleeble is the one of the most well known physical simulator and is used to simulate heat treatments and the heat affected zone (HAZ) in welds. Although it might appear easier to simply test actual weld HAZs than to use equipment like Gleeble, a complex mixture of microstructures within a very narrow zone makes it difficult to perform localized tests in the HAZ [65]. The layout of Gleeble 540 simulator is shown in Figure 2.23. Although welding was not explored in this study, regardless, Gleeble is still a very valuable and essential tool because of the flexibility it offers. It is possible to carefully control the rate of heating and cooling of the specimen to develop desirable microstructures and in turn, allows for the simulation of a variety of different heat treatment processes. The sample may be clamped on both ends and different loading conditions may be applied on the specimen during heating/cooling. The heat treatment is performed at a limited area in the middle of the specimen and is shown in Figure 2.24.

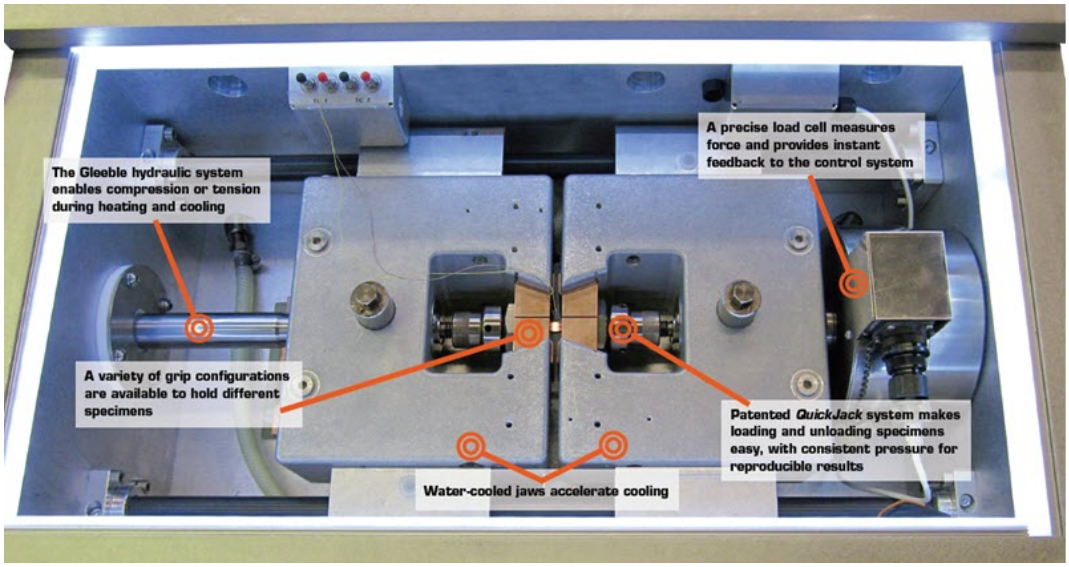

FIGURE 2.23: General layout of Gleeble 540 simulator [66]

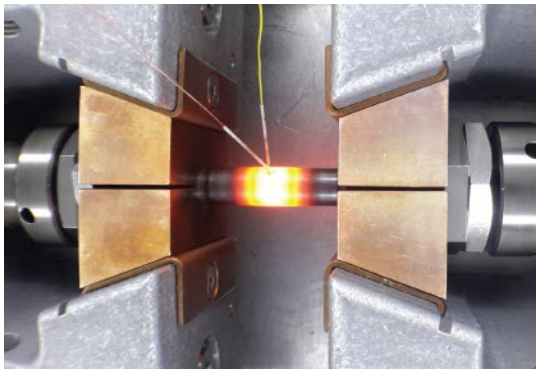

FIGURE 2.24: Heat treatment at a localized region in the specimen [66]

A study using Gleeble simulators has shown the effect of tempering on the toughness of steels [67]. Figure 2.25 shows the variation in toughness with tempering temperatures, in different tempering processes. For the SS400 steel, a linear incremental trend with increasing tempering is observed for the toughness values with a holding time of 40 s. The maximum toughness values for a holding time of 30 or 50 s are obtained at tempering temperatures of 620 °C. At tempering temperatures of 560 and 620 °C, the the total amount of cementite gradually increases. This is due to new cementite being dispersed, which are nucleated with increase in holding time. As the tempering temperature and the holding time increases, the cementite precipitates are coarsened [67].

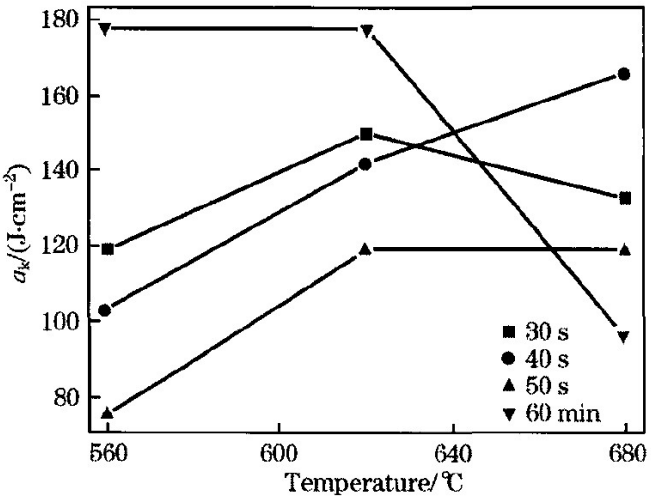

FIGURE 2.25: Variation of impact values with various tempering temperatures at -40°C with Gleeble simulator [67]

A study has shown that steels for a certain application may be engineered through Gleeble simulations using the TMCP method [68]. A 800 MPa grade steel, initially only delivered as quenched and tempered was engineered through a simulated TMCP method. The microstructure in resulting steel was primarily composed of lower bainite and granular bainite. The process curve for the simulated TMCP is shown in Figure 2.26.

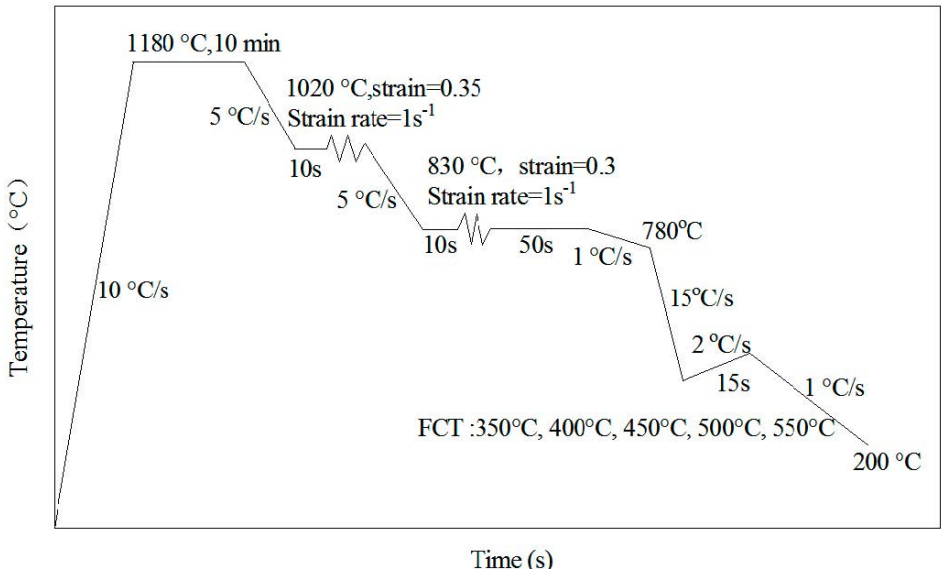

FIGURE 2.26: Process curve of simulated TMCP with Gleeble simulator [68]

It was said in the earlier sections that high-angle grain misorientations are beneficial for hindering trans-granular crack propagation. Studies have shown that it is possible to engineer grain boundaries through thermo-mechanical simulations [69]. A series of high-temperature compression tests were performed to simulate isothermal forming conditions, with varying strain rates. The electron back-scattered diffractometer (EBSD) band contrast maps of RR1000 steel for varying strain rates are shown in Figure 2.27.

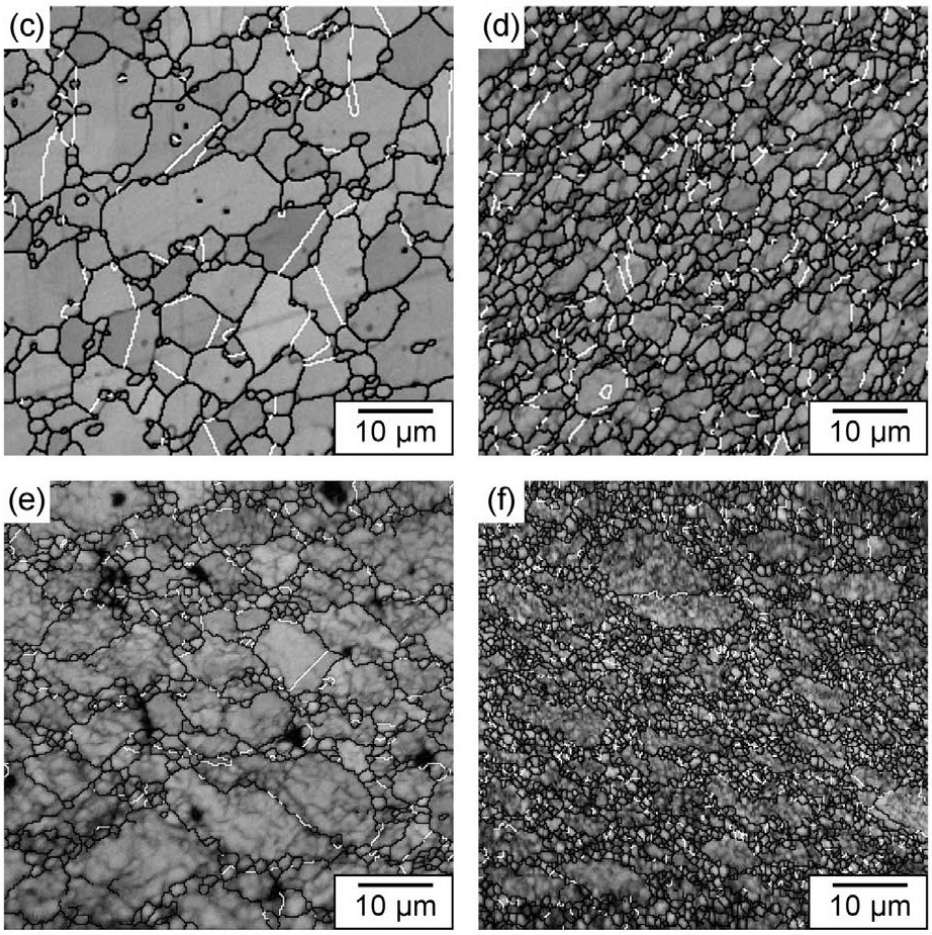

FIGURE 2.27: EBSD band contrast maps for RR1000 steel after deformation at (c) 1100°C - 0.001/s (d) 1020°C - 0.05/s (e) 1060°C - 0.01/s (f) 1020°C - 0.1/s [68]

2.6 Summary

Thick section high strength steels are popularly used in offshore applications, where temperatures may be in the subzero range. These steels are known to transition from ductile behavior to cleavage dominated fracture behavior with reduction in temperature. Literature has shown that although cleavage failure is sensitive to the service temperature, there are other underlying microstructural features which strongly influence cleavage in these steels. Microstructural features such as phases, grains, segregation bands and precipitates/inclusions influence cleavage initiation in high strength steels. From the reviewed literature, is observed that there is a gap in the knowledge about the link between microstructural features and cleavage fracture behaviour, especially on the effects of grain size on cleavage fracture toughness.

Chapter 3

Material and methods

The contents of this chapter describe the material used the study and the experimental techniques employed. Microstructure characterization involved phase identification, inclusion analysis and quantification, grain size measurements and crystallographic characterization. Mechanical tests performed in this study were hardness measurements, fracture toughness and tensile tests. Thermo-mechanical tests such as dilatometry and an isoparametric grain refinement process using Gleeble simulator were also employed in this study.

3.1 Material

The material used in this study is a commercially available 100 mm thick hot rolled, quenched and tempered S690 HSS (designated as S690QT) plate. The material is used in the offshore industry, subject to high loading rates [70]. The chemical composition of the as-received plate was determined by LECO combustion analysis (for C, N, S) and X-Ray fluorescence (other elements) for the through-thickness. Smaller blocks of dimensions 100 mm x 740 mm x 180 mm for the extraction of tensile and fracture toughness specimens were machined from the plate using a metal cutting band saw.

3.2 Microstructural characterization

3.2.1 Sample preparation

To study the variation in microstructure of the through-thickness of the as-received plate, specimens were machined for the top and middle sections using a Struers metallographic cutting machine. The specimens were then embedded in hard epoxy mounts and sanded from P80 (coarse) to P2000 (fine) grit papers. The sanding time for the coarse grit paper was approximately 60 seconds and increments of 30 seconds were made for every change in grit size. The use of silicon carbide sanding paper showed particles from the paper becoming embedded within the matrix, so aluminium oxide sanding papers were used instead. Subsequently, the specimens were polished using 3 μ and 1 μ diamond slurry for approximately 20 minutes for each step until a fine mirror finish was obtained. Isopropanol was used as a cleaning agent instead of water due to rapid corrosion of the polished surface.

Two different etching reagents were used depending on the type of microstructural study and are given in Table 3.1. Henceforth, these reagents will be referred to as type 1 and type 2. The top and middle sections were both etched with type 1 reagent for 5 - 8 seconds to reveal the phases in the microstructure. For the PAG study, specimens were swab etched with type 2 reagent for 8 minutes to reveal the PAG boundaries [71]. Similar cutting, sanding, polishing and etching techniques were followed for the isoparametric study. The specimens were then observed by means of optical microscopy (Leica DMLM), digital microscope (Keyence VHX-5000) and SEM (Jeol JSM IT-100). The microscopes were used primarily to identify phases present in the top and middle sections, and also observe the grain structure. For the heat treated specimens, optical microscopy and SEM was used to observe the evolution in microstructure in comparison to the as-received material.

TABLE 3.1: Etching reagents used for microstructural study

Reagent	Components	Amount
Type 1	Nital	2 %
Type 2	Sodium dodecyl benzene sulfonate Saturated aqueous picric acid sol.	0.1 g 20 mL

3.2.2 Inclusion study

To study the inclusion size, morphology and chemical composition in the as-received material, SEM was used with energy dispersive X-Ray spectroscopy (EDS). For the inclusion quantification, SEM was used in accordance with the ASTM E1245:03 standard [72]. In this study, the size of the inclusions were determined using the major axis using ImageJ software. An example of the inclusion size analysis is shown in Figure 3.1. To quantify the inclusions in the material, the area and number fraction of the inclusions were determined. 200 frames for both top and middle sections were captured at random locations in the matrix. A magnification of 900x was used to have an area large enough to contain at most 3 inclusions. Inclusion analysis and quantification were not performed in the isoparametric study.

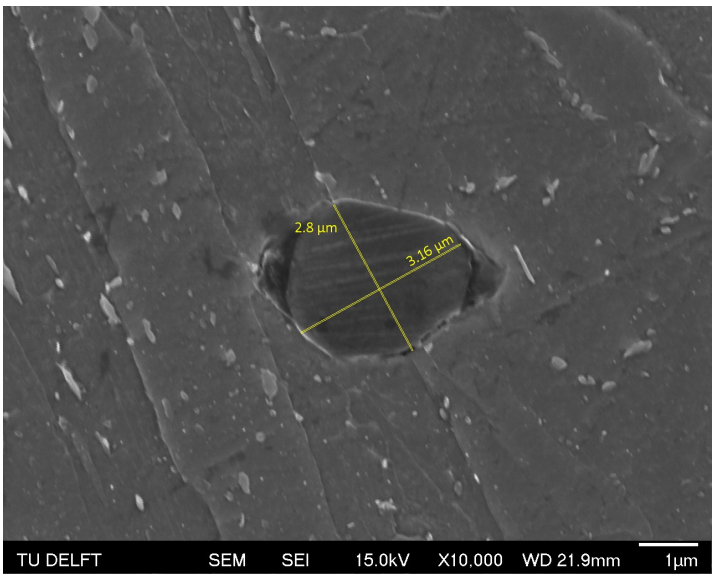

FIGURE 3.1: Example of inclusion size analysis in a spherical type inclusion. Major axis is approximately 3.2 μm

3.2.3 Grain size measurements

The PAG average grain size measurements were made in accordance with the ASTM E112-13 standard [73]. ImageJ software was used for the Heyn line intercept method. For the middle section, 5 frames each were captured in regions inside the segregation bands, outside the segregation bands and regions including segregation bands. For the top specimen, only 5 frames at random positions were captured. Figure 3.2 shows the line intercept method for a middle section specimen in a region including a segregation band. Two red lines of length 700 μm were drawn and the number of grain boundaries intercepts with respect to the base lines were recorded. An intersection was assigned a weight of 1, a triple point was assigned a weight of 2 and a tangent was assigned a weight of 0.5. The total number of each intercept type was multiplied with its respective weight and to obtain a weighted intercept count. The ratio of the base line length (700 μm) to the weighted intercept count is the average grain intercept. The arithmetic mean of the average grain intercept for both base lines is the average grain size. This method was applied for the isoparametric study.

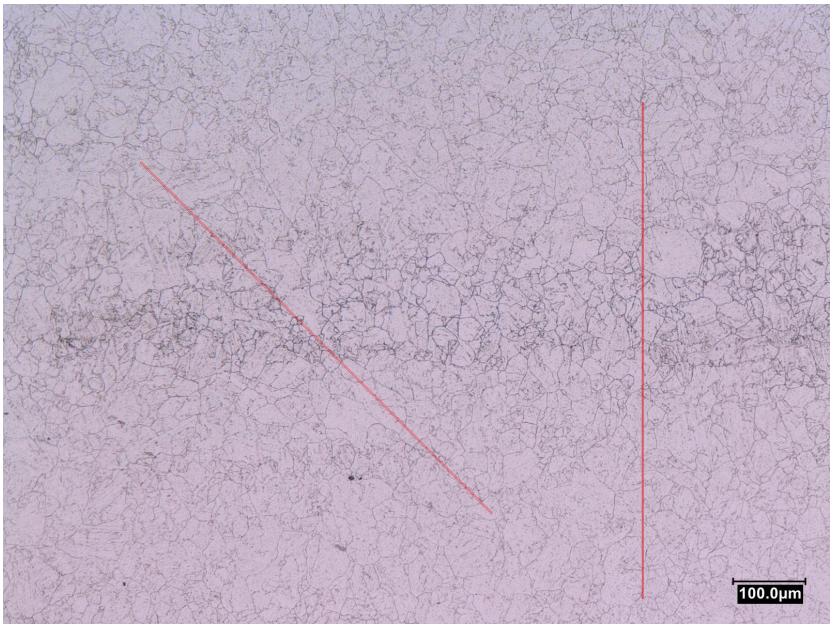

FIGURE 3.2: Heyn line intercept method for PAG size measurement

3.2.4 Hardness measurements

Specimens for the hardness measurements were prepared following the same methods as for the microstructural characterization specimens. However, the etching process was eliminated. To observe the variation in through-thickness hardness, a specimen was machined from the block to include the entire thickness. A set of 5 measurements were made with 100 indentations for each set ranging through the entire thickness of the specimen. The apparatus used was a Durascan micro-hardness tester supplied with Ecos workflow. The loading condition for these measurements was set at HV_3 (3 kgf) for all specimens. Hardness measurements were also made for specimens from the isoparametric study. 2 sets of 10 hardness measurements each were made for two specimens to have representative results.

3.2.5 EBSD

EBSD was used to obtain microstructural information such as grain size distribution, misorientation angle, texture and grain aspect ratio. The equipment used was a ThermoFisher Helios G4. The specimens for EBSD analysis were prepared using cutting, sanding and polishing techniques similar to that for the microstructural characterization specimens. The polishing times for the EBSD specimens were approximately 40 minutes for the 3 μ and 1 μ steps instead of 20 minutes to ensure good diffraction patterns. An addition polishing stage was carried out with 0.4 μ OPS liquid with a speed of 200 rpm for 20 minutes which slightly revealed the microstructures of the polished surfaces.

For the top section, 3 scans were performed at random positions in the matrix. For the middle section the regions of interest were inside the segregation bands, the matrix without the bands and regions containing both matrix and segregation bands. To mark the locations of the segregation bands, polished specimens were first etched with type 2 reagent. Then the start and end positions of the bands were marked by a micro-hardness indenter. The specimens were polished again with the 3μ, 1μ and OP-S steps. 3 scans were performed in each of these regions. The scans were performed over an area of approximately 320 μm x 255 μm for each specimen at a magnification of 1300x with a step size of 0.45 μm. The scans were analysed with TSL OIM v7.3 software. Prior to processing the data a cleanup process was first performed. For the cleanup, the techniques employed were grain fit standardization (grain tolerance angle = 5°, minimum grain size = 2, minimum CI = 0), neighbour orientation correlation (grain tolerance angle = 5°) and neighbour phase correlation (minimum CI = 0.1). An example of the effect of cleanup process on an inverse pole figure (IPF) is shown in Figure 3.3. High angle grain boundaries were generated using a threshold misorientation rotation angle 15°. For the PAG boundary reconstruction, ARPGE software developed by Cayron was used [74]. The grains were reconstructed in automatic mode using quadruplets as the reconstruction method, with tolerance for parent grain nucleation and growth equal to 3°and 6°[70]. The misorientation angles, major and minor axes of the grains were determined by using boundaries between identified grains only. This method was also applied to the specimens from the isoparametric study.

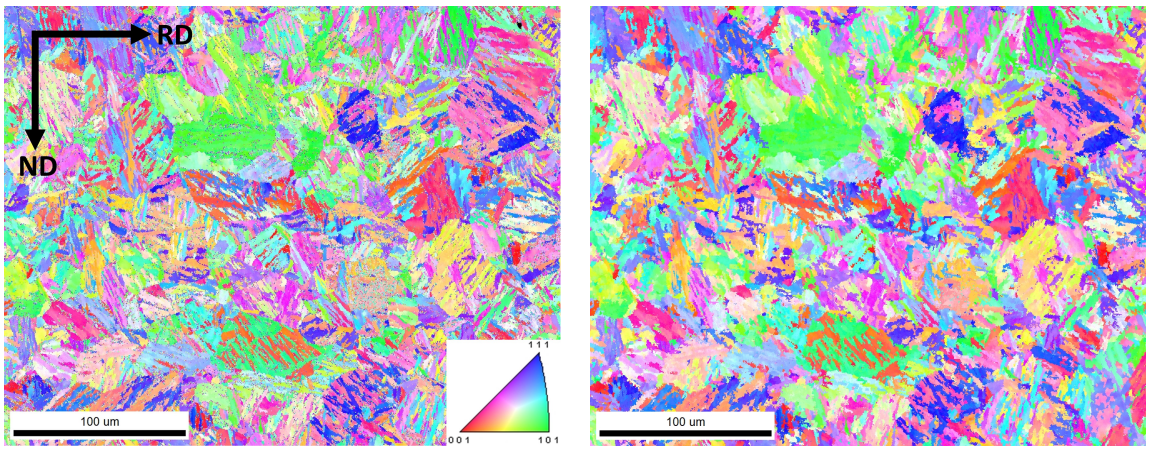

(A) (B)

FIGURE 3.3: Effect of cleanup process on IPF (A) Prior cleanup (B) Post cleanup

3.3 Mechanical tests

3.3.1 Tensile tests

Tensile tests were performed for the as-received material and specimens from the isoparametric study for a comparative investigation. The specimens were machined in accordance with ASTM E8 / 8M-16a standard [60]. The dimensions of these specimens are given in Figure 3.5. For the as-received material, cylindrical specimens were machined from both top and middle sections at three different orientations. The orientations were parallel to the rolling direction, perpendicular to the rolling direction and 45°to the rolling direction. For the as-received material, the tests were performed at -130 °C to ensure failure occurred in the lower shelf. Threaded gripping ends were machined ensure ice formation in the setup would not cause slippage. An example of the orientation of the specimens with respect to the rolling direction is shown in Figure 3.4. For the isoparametric study, specimens were machined from the middle section perpendicular to the rolling direction. A lower gauge length was used in order to have a large homogeneously heat treated region.

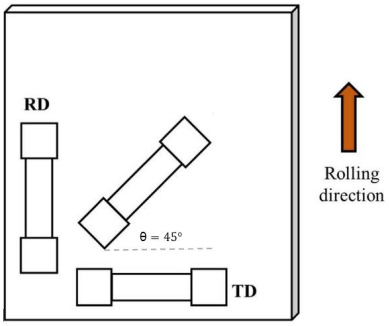

FIGURE 3.4: Example of the orientations of tensile specimens with respect to rolling direction [75]

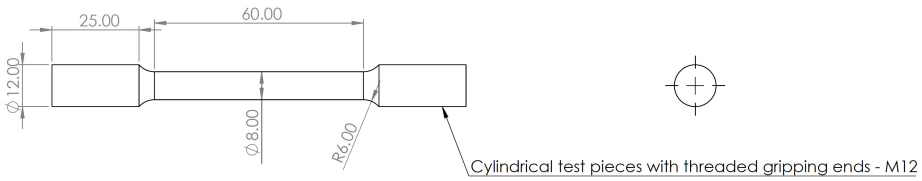

(A)

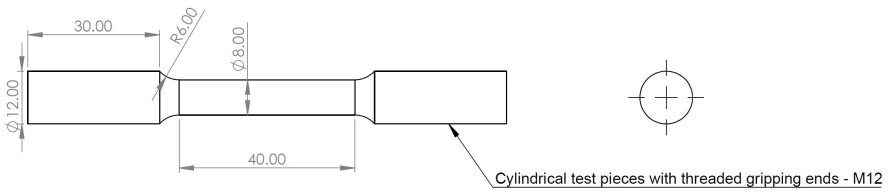

(B)

FIGURE 3.5: Dimensions of tensile specimens (A) As-received material (B) Isoparametric study

3.3.1.1 As-received material

For the as-received material tensile tests at -130 °C, a Zwick universal testing machine was used with an environmental chamber built around it and is shown in Figure 3.6a. The entire test setup for these specimens is shown in Figure 3.6. The specimen (1) with threaded gripping ends was screwed into cylindrical clamps (2). The clamps with the specimen in place were then attached to the upper and lower fixtures (3) by bolts (4). The extensometer (5) was subsequently fixed to the specimen at the ends of the gauge. In order to monitor the temperature of the specimen, two sets of thermocouples were spot welded to regions on either end of the gauge, within the rage of the extensometer. The test was initiated when the mean of both thermocouples measured -130 °C. The above steps were followed for all specimens from different sections machined at different orientations. At least three valid results were required from each test condition in order to have representative results. The strain rate used for the as-received material tensile specimens with gauge length of 60 mm was 1.2 mm/s, which was similar to the strain rate used for the fracture toughness tests.

After testing all tensile specimens from the as-received material, it was observed that only 1/3rd of the results had extensometer data. Fortunately, cross-head travel data was still preserved in the results. Although the yield and ultimate tensile stresses remained unchanged, the Young's modulus could not be measured from the cross-head travel because the movement of components within the machine added to the total displacement of the specimen. A method was designed to convert the cross-head travel to extensometer strain by eliminating the machine displacement in the cross-head. In order to keep the contents of this section concise, the method is not discussed here. Refer to appendix 6 for the cross-head displacement travel conversion.

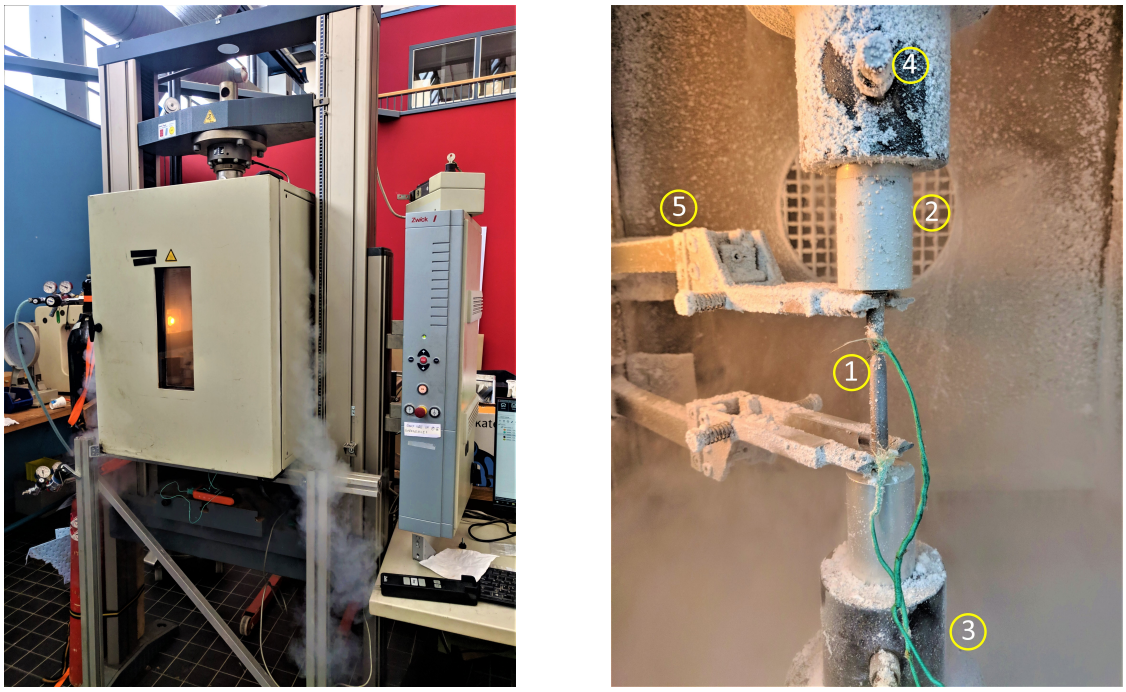

(A) (B)

FIGURE 3.6: As-received material tensile tests (A) Zwick universal testing machine with environmental chamber (B) Tensile test setup (1) specimen (2) cylindrical clamps (3) fixtures (4) bolts (5) extensometer

3.3.1.2 Heat treated specimens

For the heat treated tensile specimens, the tensile tests were performed at room temperature with an Instron 5500R universal testing machine. Prior to performing the tensile tests, it was observed that the tensile specimens after heat treatment in the Gleeble welding simulator exhibited deformation. The specimens were subsequently straightened out in a turning machine. The turning operation required the threads at the gripping ends to be removed in order to be clamped into the turning machine. The diameter of the specimens were reduced until no more deformation was observed. From the experiments in the Gleeble simulator, it was estimated that a region of approximately 18 - 20 mm was homogeneously heat treated. Therefore the heat treated region was machined with a 50% reduction in cross-section in a 10 mm gauge to maintain homogeneity. This double dog-bone geometry was performed to ensure that failure would occur in the heat treated region. This geometry is shown in Figure 3.7a, after failure.

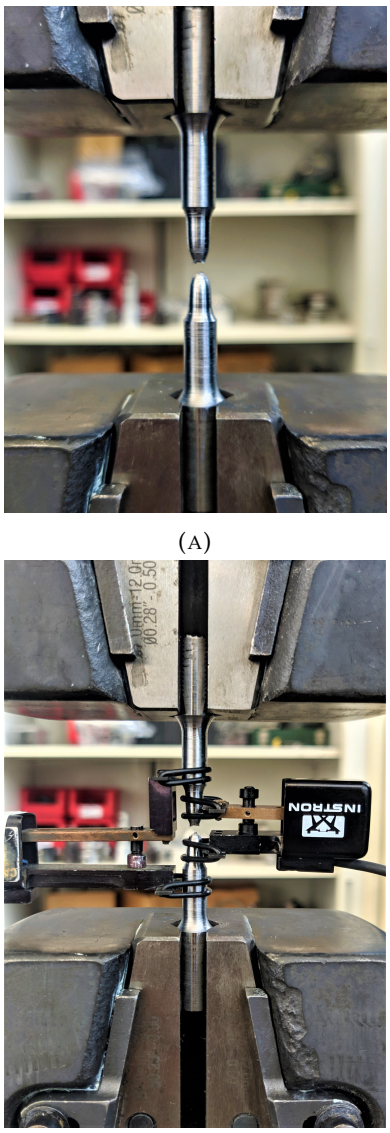

(A)

(B)

FIGURE 3.7: Heat treated specimen tensile tests (A) Double dog-bone geometry (B) Tensile test setup with double extensometer construction

To determine the strain rate for the reduced gauge, a reduction in strain rate was performed due to the linear relationship between strain rate and gauge length. In the previous subsection, the strain rate used for a gauge length of 60 mm was 1.2 mm/s. Following the linear relationship, the new strain rate for a gauge length of 10 mm was determined to be 0.2 mm/s. For the final tests, a double extensometer construction was used. The first extensometer was placed in the inner gauge corresponding to the heat treated zone. The second extensometer was placed in the outer gauge to investigate possible plastic extension in the specimen outside the heat treated zone. This construction is shown in Figure 3.7b. Contrary to the as-received material specimens which had threaded gripping ends, the heat treated specimens had smooth cylindrical profiles. For this profile wedge clamps were used and were tightened with sufficient torque by hand, with the specimen protection feature switched on to prevent damage to the gripping ends. To estimate the yield stress and ultimate tensile strength at -130 °C, the respective stresses at room temperature are related with the assessment temperature in accordance with the BS 7910 + A1 standard [76]. The relations are a widely accepted standard when tensile properties are unavailable at the assessment temperature, and are given in Equation 3.1 and Equation 3.2.

$$\sigma_{y\ (low\ temp)} = \sigma_{y\ (room\ temp)} + \frac{10^5}{(491 + 1.8T)} - 189 \tag{3.1}$$

$$\sigma_{u\ (low\ temp)} = \sigma_{u\ (room\ temp)} \left(0.7857 + 0.2423\ exp\left(- \frac{T}{170.646} \right) \right) \tag{3.2}$$

Where σ_{y} is the yield stress, σ_{u} is the ultimate tensile stress and T is the assessment temperature.

3.4 Fracture toughness

Three point bend tests were performed at -130 °C for the as-received material and specimens from the isoparametric study in accordance with ISO 12135 standard for a comparative investigation [63]. This temperature ensured that the specimens failed in the lower shelf. In order to study the effect of inhomogenous through-thickness microstructure on cleavage fracture, SENB specimens were machined from the top and middle sections with the notches parallel and perpendicular to the rolling direction (T-L and L-T orientations). The dimensions and orientations are shown in Figure 3.8. Two different constraint conditions were tested (a/W ratios of 0.5 and 0.25) to present a comparative study between high and low constraint conditions for both top and middle sections. Defects observed in structural components were observed to be shallow cracks resulting in a low constraint condition, unlike deep cracks resulting in a high constraint condition [77]. For the low constraint condition, notches of length 3.5 mm were machined and for the high constraint condition, notches of length 8.5 mm were machined. For the isoparametric study, specimens were machined from the middle section in a high constraint T-L orientation with the same dimensions.

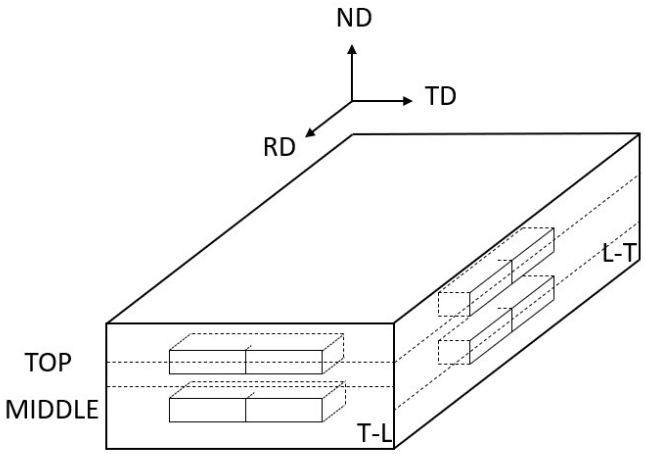

(A)

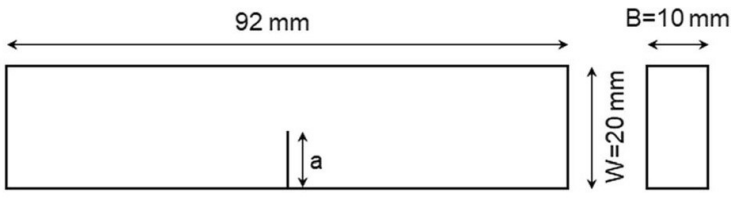

(B)

FIGURE 3.8: Schematic showing the orientations and dimensions of SENB specimens (A) Extraction of T-L and L-T specimens from the blocks (B) Dimensions of SENB specimen with notch length *a* [70]

3.4.1 Test setup

The fracture toughness tests were performed using a 350 kN MTS 858 servo hydraulic. Prior to testing, the notches for both low and high constraint conditions were extended by 1.3 mm through cyclic loading at room temperature to reach the final notch lengths. The 1.3 mm length was divided into 3 equal regions by a horizontal scribing tool. The specimen was then placed on cylindrical rollers of diameter 20 mm and a span of 80 mm. For the first region cyclic loading was performed until the crack initiation began. The amplitude and target set-point for the force was determined using the known fracture toughness of a S690QT steel with similar composition. For the second and third regions the amplitudes and target set-points were calculated through the equation for stress intensity factor, keeping the stress intensity factor fixed as 25 and changing the value for a as the crack propagated. This allow the extension of the crack to be carefully controlled and also avoid a large plastic region around the crack tip. This method was followed for all specimens and the setup is shown in Figure 3.9. After completely immersing in liquid nitrogen, the specimen was subsequently placed on the rollers with foam insulation to prevent rapid heat exchange between the metallic surfaces and the extensometer was attached quickly. When the thermocouples measured -130 °C then test was performed with a loading rate of 2 mm/s which is the loading rate experienced in offshore structures. The temperature was sufficient to result in cleavage fracture in the lower shelf. This method was followed for the SENB specimens from the as-received material as well as from the isoparametric study.

FIGURE 3.9: MTS test setup for the fatigue crack extension at room temperature

3.4.2 Fractographic analysis

In order to perform fracture surface analysis, the specimens were cooled to -185 °C again and overloaded in the MTS setup to obtain clean halves. The fracture surfaces were cleaned with isopropanol, coupled together and stored in a desiccator. The fatigue crack extensions were measured by means of Keyence in accordance with ISO 12135 standard [63]. River lines leading up to the fracture initiation zone were observed and the presence of inclusions in the initiation zones were validated by a combination of SEM and EDS. The distance between the fatigue extended crack and the fracture initiation zone were measured.

3.5 Isoparametric study

3.5.1 Dilatometry

In order for the process curves for the heat treatment to be designed, it was important to first determine the critical temperatures of the S690QT steel. The critical temperature at which all ferrite completely transforms into austenite is the austenite transformation temperature (AC_3) [78]. The AC_3 for S690QT was determined by dilatometry. ThermoCalc was also used to determine the AC_3 to compare with the results from dilatometry. The objective of using ThermoCalc to determine the AC_3 was that the need for performing a time consuming experiment could be eliminated if the results from both studies concurred. The specimen for dilatometry was machined with dimensions of 20 mm x 10 mm x 5 mm. The heating rate was set at 1 °C/s from room temperature to 1000 °C followed by quenching at a cooling rate of approximately 85 °C/s. The AC_3 was determined from the plot using the tangent method. Figure 3.10 shows an example to help visualize the results from dilatometry.

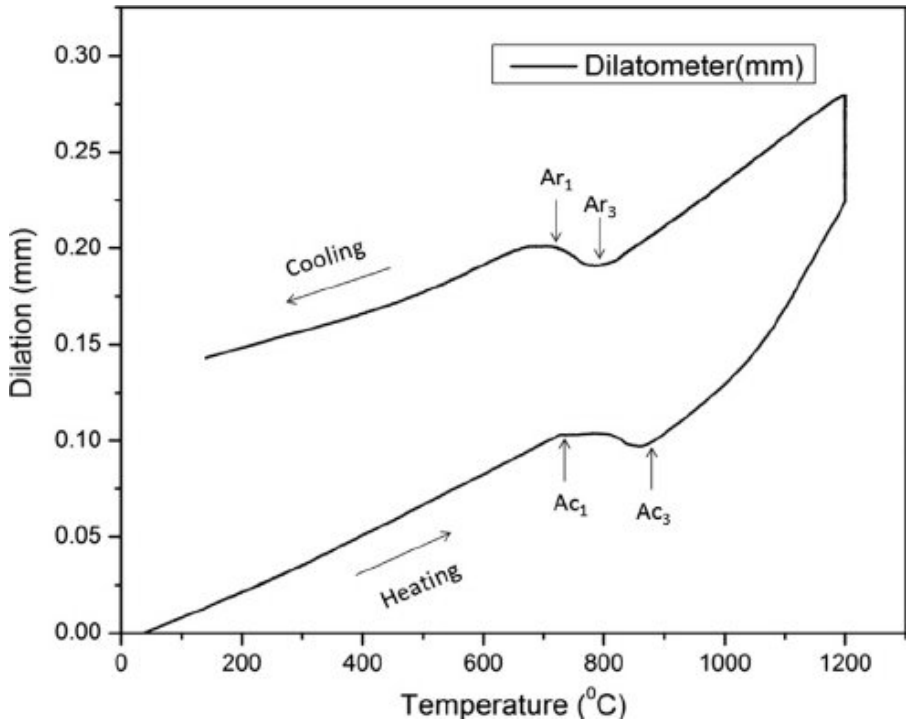

FIGURE 3.10: Dilatometry example for a low C, Nb-Ti steel demonstrating the various critical temperatures [79]

3.5.2 Heat treatment

3.5.2.1 Heating profile

According to the Hall-Petch equation described in chapter 2, the mechanical properties of steels can be improved by grain size reduction. The objective of the heat treatment in this study was to reduce the grain size while retaining the microstructure of the as-received material, i.e. grain refinement. S690QT and other low-carbon steels typically have high AC_3 temperatures [80]. To avoid grain growth, shorter heating and holding times were employed in this study, along with higher heating rates. Studies have also shown that cyclic heat treatments promote the effect of grain refinement [81]. A recommendation for the number of cycles to improve toughness and ductility is a maximum of four [15].

A quench and temper profile for a S690QT grade HSS with a similar composition was followed. For the grain refinement, a fast heating rate was followed from room temperature to 870 °C (25 °C above the AC_3) in under 1 minute, followed by a holding time of a couple of minutes. The objective of rapid heating to just above the AC_3 and holding for a short time was to facilitate complete austenitic transformation, while preventing excessive grain growth. This was followed by a fast cooling in a few seconds to room temperature. The high cooling rate promotes a martensitic microstructure with refined grains [82]. For the industrial quench, the same heating rate was followed from room temperature to a temperature between 870 °C and 950 °C in under 1 minute, with the same holding time. This was followed by air cooling to room temperature in a couple of minutes. The same heating rate was followed for tempering from room temperature to a temperature between 600 °C and 650 °C, with a slightly longer holding time. This was followed by a slower air cooling to room temperature in around 5 minutes at a slow cooling rate.

3.5.2.2 Gleeble

Gleeble 1500 and 3800 welding simulators were used in this study for the post-process thermo-mechanical treatments. The apparatus performs heat treatments through resistive heating, i.e, with high current. Heat treatments for the as-received material were first performed on cylindrical specimens of diameter 6 mm and length 80 mm in the Gleeble 1500 apparatus. The objective was to characterize the heat treated microstructure prior to employing the method to the tensile and fracture toughness specimens. For the cylindrical specimens, one set of thermocouples were spot welded to the mid-section of the specimen which served as the control. Additional two sets monitoring thermocouples were welded 15 mm on either side in order to determine the length of homogeneously heat treated zone. Microstructural characterization in the homogeneously heat treated region was performed after employing sanding, polishing and etching techniques in section 3.2.

For the fracture toughness specimens in high constraint (a/W = 0.5) T-L condition, a homogeneously heat treated length of 5 - 8 mm was obtained. The construction is shown in Figure 3.11. It was found that the cooling rate for the fast cooling could not be achieved due to the larger volume of the specimens even after increasing the water pressure. Microstructural characterization was done to study the effect of change in cooling rate. For the tensile specimens, the threaded gripping ends could not be accommodated in the clamps. Hexagonal nuts were used as sleeves and this construction is shown in Figure 3.12.

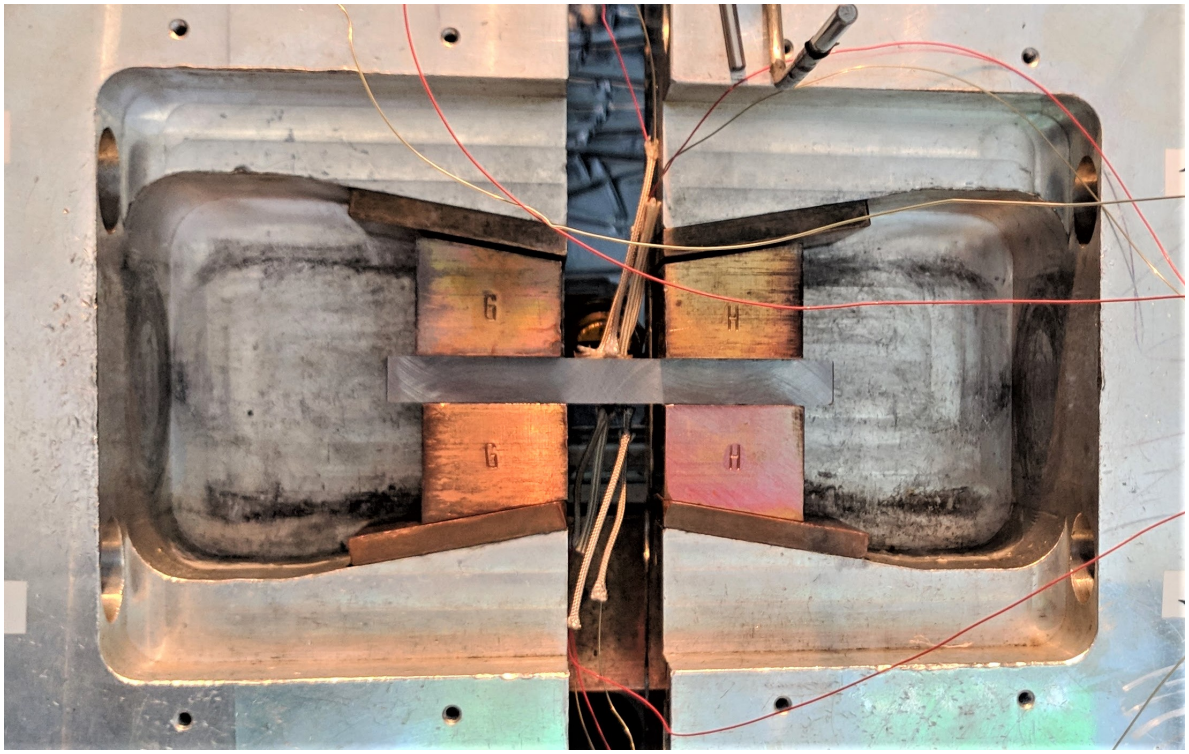

FIGURE 3.11: Fracture toughness specimen construction in Gleeble 1500 simulator

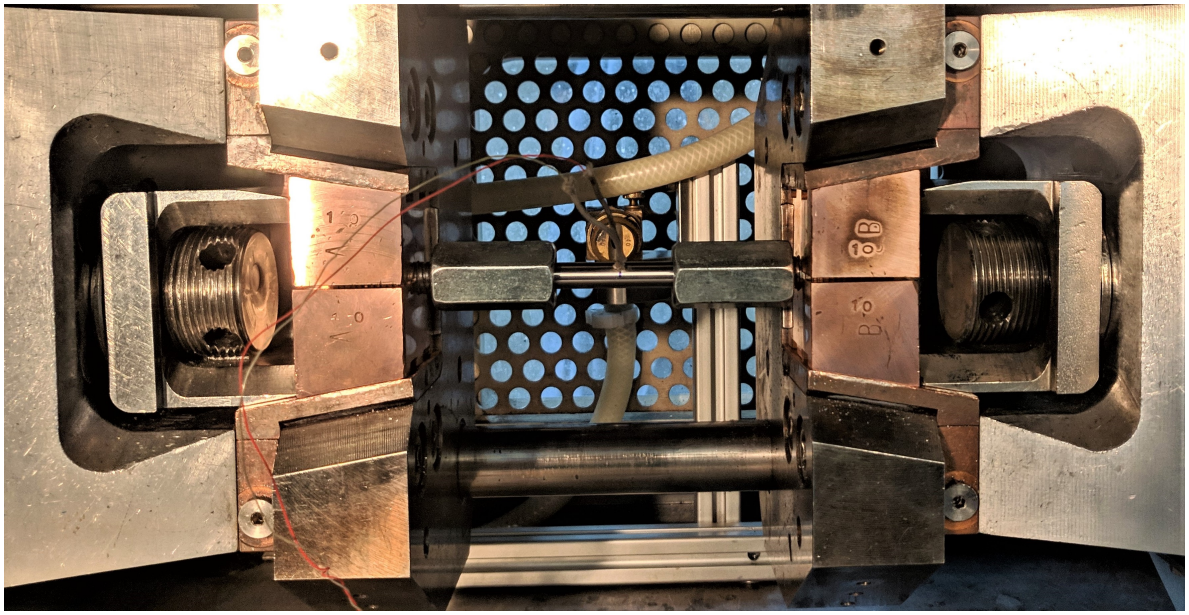

FIGURE 3.12: Tensile specimen construction in Gleeble 3800 simulator

Chapter 4

Results and discussion

4.1 Microstructural characterization

The content of this section discusses the microstructural study of S690QT HSSs with emphasis on chemical composition, phases present, inclusion analysis and quantification, grain size and hardness measurements. The results of the microstructural evolution of the isoparametric study are also presented and discussed. Subsequently the base material and heat treated material are compared.

4.1.1 Chemical composition

The chemical compositions for the top and middle sections for the as-received material are given in Table 4.1. The distribution of all elements throughout the plate may be considered homogeneous. It was observed that the C concentration is marginally higher for the top section. A large difference in scatter for Si was observed between the two sections. Industrial process parameters showed that the cooling rates were approximately 5 °C/s in the middle section and 7 °C/s the top section for the quench. Since the top section cools faster than the middle, it is expected that the microstructure varies from a completely martensitic structure at the surface to a martensitic-bainitic structure towards the middle [83].

TABLE 4.1: Through-thickness chemical composition of as-received S690QT

wt. (%)	Fe	C	Ni	Mn	Cr	Mo	S	Cu	Al	Si	V	P	N
Top	Bal.	0.103 ± 0.006	1.91 ± 0.10	0.98 ± 0.06	0.71 ± 0.07	0.44 ± 0.02	0.005 ± 0.001	0.29 ± 0.09	0.08 ± 0.01	0.072 ± 0.004	0.03 ± 0.01	0.006 ± 0.001	<0.002
Middle	Bal.	0.097 ± 0.001	1.98 ± 0.20	0.94 ± 0.03	0.71 ± 0.02	0.43 ± 0.02	0.004 ± 0.001	0.30 ± 0.05	0.06 ± 0.01	0.07 ± 0.02	0.04 ± 0.02	0.006 ± 0.002	<0.002

4.1.2 Microstructure of as-received and heat treated S690

Microstructural observation of the as-received material under SEM revealed a complex microstructure in both top and middle sections, and is seen in Figure 4.1. The top section presented what appears to be a tempered martensitic microstructure, with carbides and laths oriented in multiple directions [84]. It is likely that the top section also contains tempered bainite and is difficult to distinguish from tempered martensite. The middle section presented what appears to be a mixture of tempered martensite and tempered bainite with larger PAG sizes compared to the top section. It should be noted that the constituents of tempered bainite and tempered martensite are similar in morphology and are not easily distinguishable from each other [70]. The three-level morphology of a martensitic structure comprised of lath, block and packet are seen in Figure 4.2 [85]. Tempering caused carbide precipitation in between laths, blocks and along grain boundaries [86]. SEM observation of the as-received material revealed such a morphology with carbides found in between laths and along grain boundaries and is shown in Figure 4.2a. Similar sub-structures were observed in the heat treated material and is shown in Figure 4.2b. However, far less carbide precipitation was observed between laths after grain refinement.

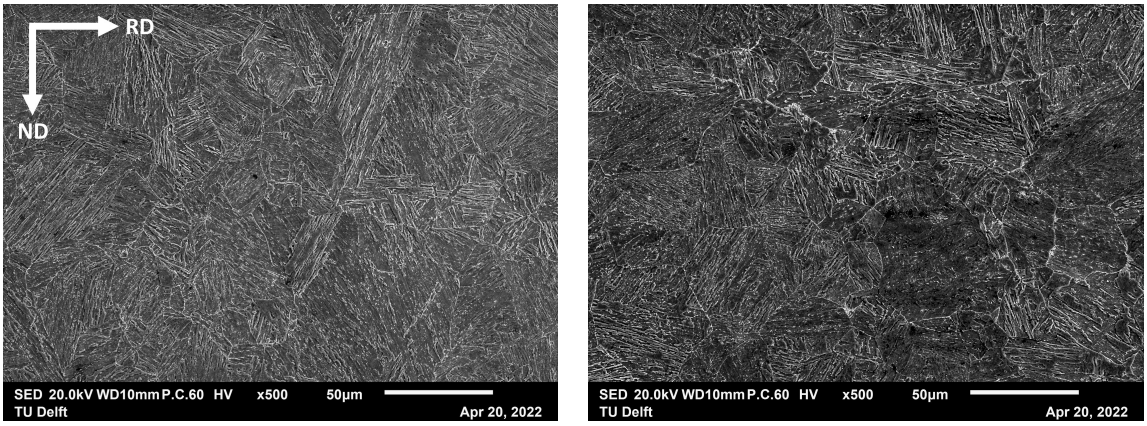

(A) (B)

FIGURE 4.1: SEM micrographs of as-received S690QT (A) top section (B) middle sections

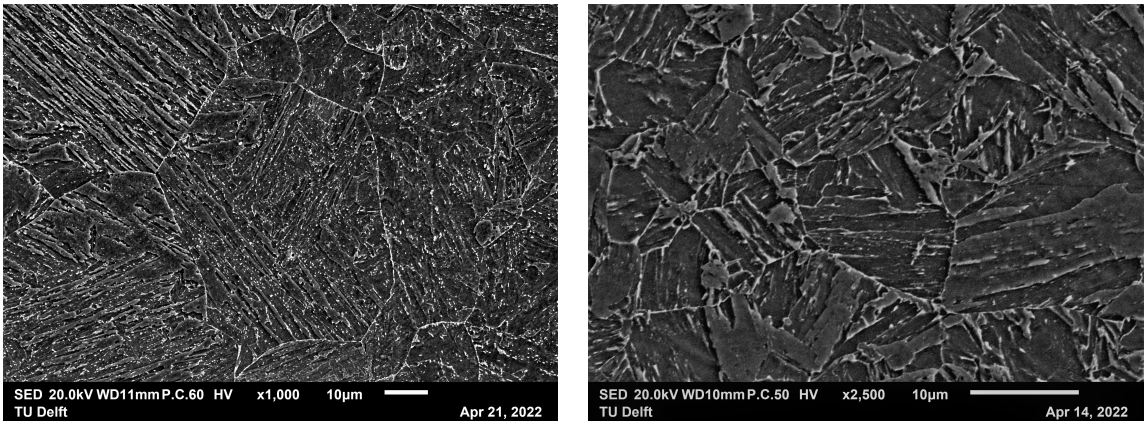

(A) (B)

FIGURE 4.2: Substructure constituents from the middle section (A) as-received S690QT (D) heat treated material

Observations in middle section of the as-received material revealed the presence of centreline segregation bands. These bands are formed due to solute segregation during the solidification process and are pancaked during the rolling process [70]. The width of these bands were measured between 25 to 200 μm, demonstrating an inhomogenous size distribution. The bands were observed to be discontinuous and dispersed throughout the entire middle section of the material. These bands were also observed in the heat treated specimens. The width of these bands were observed to remain unchanged and continued to range between 20 to 200 μm. The distribution of segregation bands from the as-received material and the heat treated specimens are shown in Figure 4.3. An SEM micrograph of the middle section of the heat treated material is shown in Figure 4.4b. Clear differences in grain size can be observed after the post-process heat treatment. Although grain refinement was successfully achieved, differences in sub-structure constituents were observed in the refined grains. The refined grains showed less carbide precipitation between laths. Observation of the microstructure hinted large blocks within the smaller PAGs, comprised of laths aligned towards the same direction. A study has explained that refinement in PAGs shifts the martensite start temperature (M_S) to lower values, and also favors the formation of blocks through an 'autocatalytic effect' [87]. The effect describes small PAGs to be attributed to higher densities of pre-existing nucleation sites for martensite. The first nucleation increases interfacial and elastic strain energy. Rapid nucleation of laths in a specific orientation follows in order to lower the energy, leading to the formation of blocks.

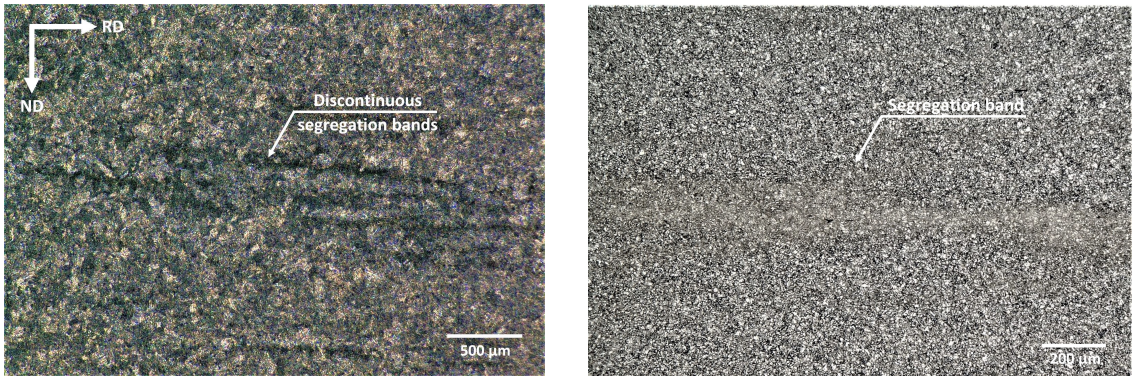

(A) (B)

FIGURE 4.3: Comparison of segregation bands distribution in the middle section (A) as-received material (B) heat treated material

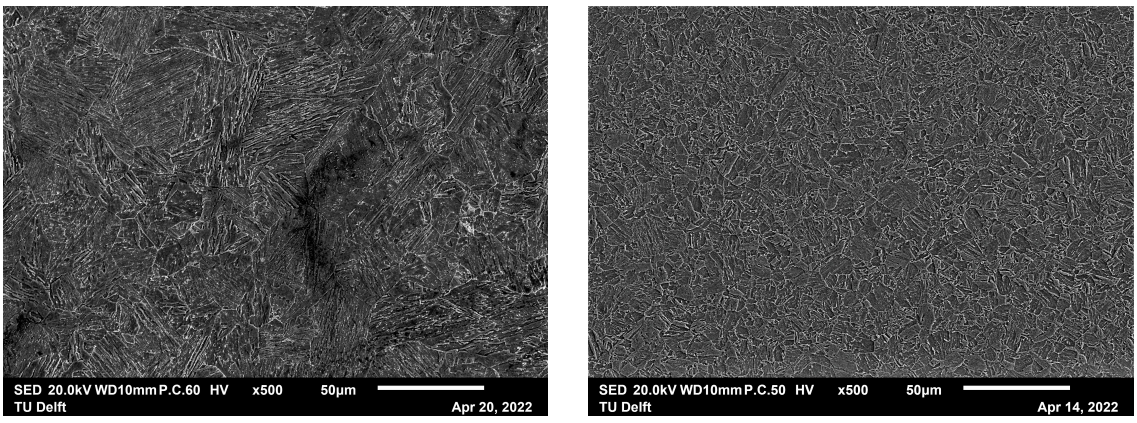

(A) (B)

FIGURE 4.4: Comparison of microstructures from middle section (A) as-received material (B) heat treated material

Dilatometry and ThermoCalc were employed for the middle section to determine the AC_3 for a comparative analysis. Using the tangent method from the dilatometry results, the AC_3 for the middle section was determined as 845 °C. From the phase diagram computed in ThermoCalc, the AC_3 for the middle section was determined as 795 °C. The comparison of results from dilatometry and ThermoCalc are shown in Figure 4.5. In the isoparametric study the maximum permissible tolerance for temperatures was $\pm$ 15 °C. This is because the objective was to have a temperature sufficient for austenite nucleation, but not growth. The difference of 50 °C from the computation was considered to be out of range and the result from dilatometry was used as the AC_3. To investigate the phases that form in the middle section during the quench a CCT diagram was computed in JMatPro software and is shown in Figure 4.6. A grain size of 25 μm and a cooling rate of 5 °C/s was used to simulate the industrial quench to observe critical temperatures for martensite formation. Although subsequent tempering (slow cooling) stage typically results in the formation of some bainite, it is not crucial for the primary phase formation. The martensitic start temperature from dilatometry was determined as 420 °C and concurred with the result from the CCT diagram. From the CCT diagram, it is likely that the middle section is comprised of a martensitic-bainitic microstructure, which is then tempered. It is apparent that the critical cooling rate for the formation of complete martensite is much higher than 5 °C/s.

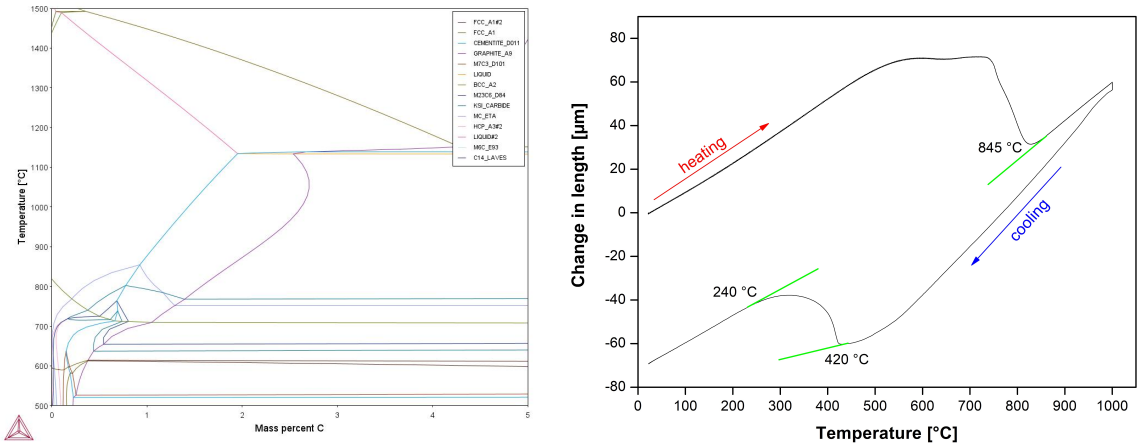

(A) (B)

FIGURE 4.5: Comparison of results to determine the AC_3 of the middle section (A) ThermoCalc phase diagram (B) dilatometric curve

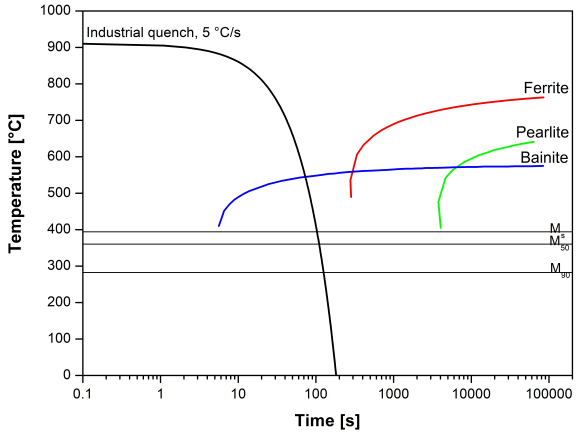

FIGURE 4.6: CCT diagram computed in JMatPro software for middle section of S690QT for PAG size of 25 μm and 5 °C/s cooling rate

Inclusions of both metallic and non-metallic type were observed to be distributed throughout the matrix in the as-received material. The most commonly found inclusions in the plate possess complex compositions comprised of oxides and nitrides and are shown in Figure 4.7. A study has shown for a HSSs with similar composition, inclusions in the middle section were coupled with voids and cracks in the surrounding matrix [70]. No such observations were made in this study. Table 4.2 presents the type of inclusions and their quantification. The inclusions in the top section were measured to be slightly smaller in size compared to middle section and were also found to be sparsely distributed compared to the middle section.

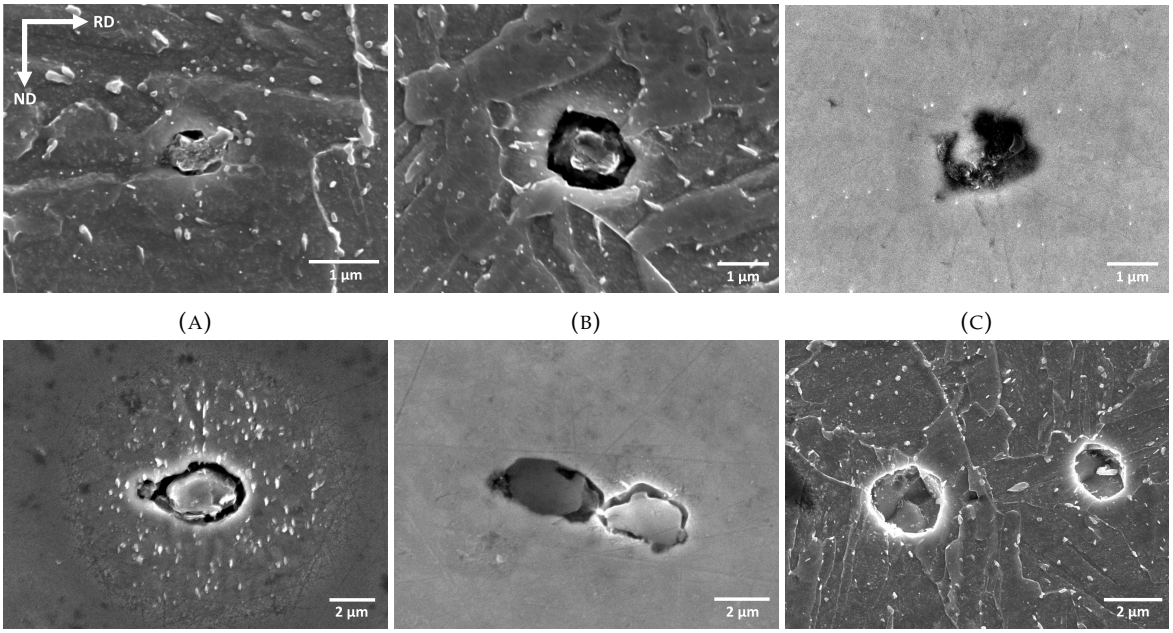

FIGURE 4.7: SEM micrographs of (A) (Al, Ti)(N), (B) (Al, Ti, Ca)(O, N), (C) (Al, Mg)(O) in the top section and (D) (Mg, Al, Ti, Ca)(O, N, S), (E) (Mg, Al)(O, S), (F) (Ti)(P, N) in the middle section of as-received S690QT

TABLE 4.2: Inclusion morphology, diameter, area fraction and number fraction in the top and middle sections of as-received S690QT

Position	**Composition**	**Average diameter range major axis (μm)**	**Area fraction**	**Number fraction (/μm^2)**
Top	(Al, Ti, Ca)(O, N) (Al, Mg)(O) (Al, Ti)(N)	0.6 - 2	1×10^{-5} $\pm$ 7×10^{-7}	7×10^{-6} $\pm$ 6×10^{-6}
Middle	(Mg, Al, Ti, Ca)(O, N, S) (Mg, Al)(O, S) (Ti)(P, N)	0.7 - 2.1	2×10^{-5} $\pm$ 7×10^{-7}	1×10^{-5} $\pm$ 3×10^{-6}

Hardness measurements along the entire thickness of the as-received S690QT revealed a gradient of hardness values, reaching a valley in the middle section of the plate. The hardness profile for the as-received S690QT is shown in Figure 4.8. The hardness in the middle section was observed to be lower than the top section. This is attributed to the larger PAG sizes observed in the middle section, and also a larger fraction of bainite in the middle section. The presence of bainite typically contributes to the softening characteristics [88]. A large scatter was observed as hardness measurements were made in the middle section of the plate. This is likely due to the presence of segregation bands in the middle section of the plate which may function as barriers towards plastic deformation [70]. Hardness measurements on the specimens from the isoparametric study reported an increase in hardness. The hardness of the refined microstructure in the middle section was improved by 13% in comparison with the as-received material. This is consistent with the interpretations of the Hall-Petch equation where hardness increases with grain refinement [25]. A large scatter was observed similar to the as-received material, likely because the width of segregation bands remained unchanged after grain refinement. The hardness comparison between middle sections of the as-received material and the specimens from the isoparametric study is shown in Figure 4.9.

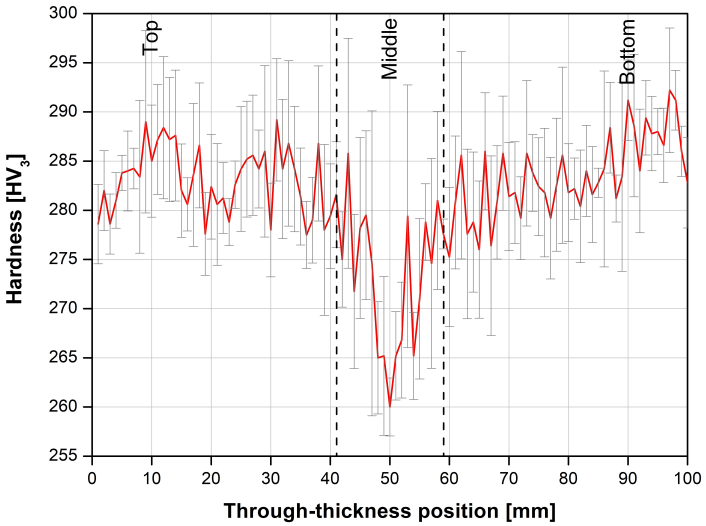

FIGURE 4.8: Through-thickness hardness profile of as-received S690QT plate

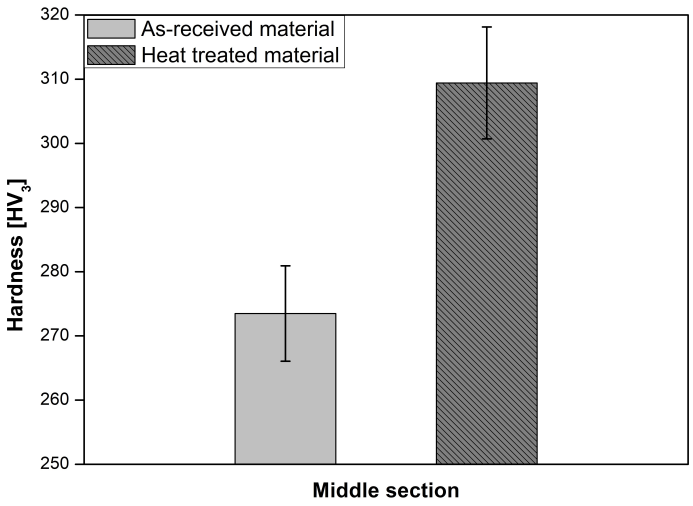

FIGURE 4.9: Hardness comparison between the middle sections of as-received S690QT plate and heat treated material

For the as-received material, reconstructed PAGs through ARPGE software for the EBSD scans showed grains with varying sizes distributed across the entire through-thickness. The grains appeared elongated in no specific direction for both top and middle sections. Inverse pole figures of these sections did not reveal a strong texture. These EBSD scans are shown in Figure 4.10. Similar observations were made in the heat treated material, with the exception of grain refinement. A comparison of reconstructed PAGs and inverse pole figures for the as-received material and heat treated material is shown in Figure 4.11.

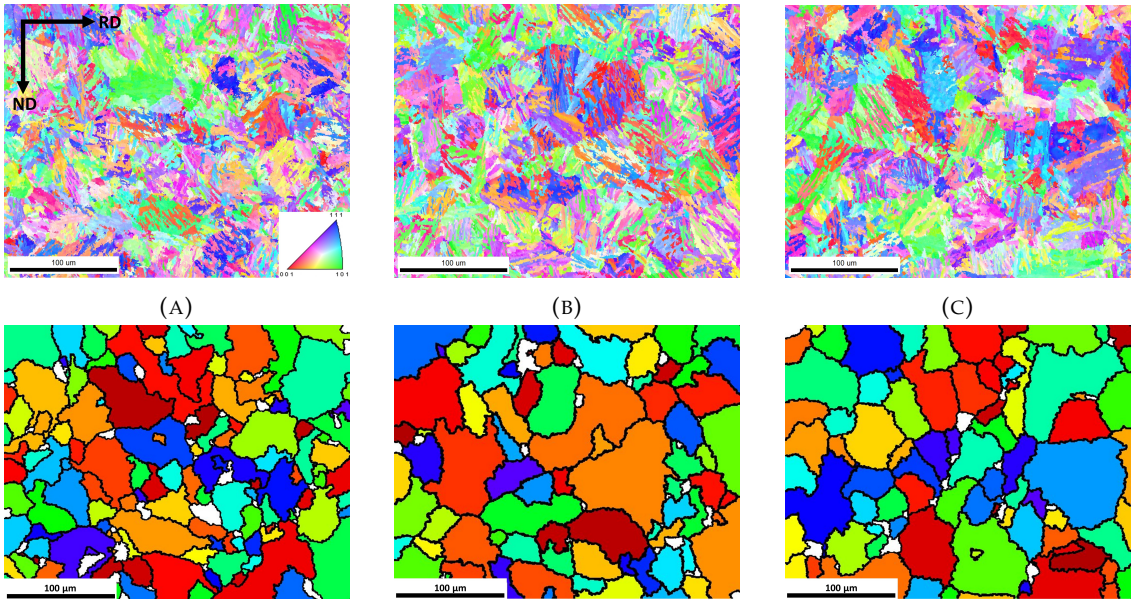

FIGURE 4.10: Inverse pole figures and reconstructed PAGs for (A),(D) top section; (B),(E) middle section outside segregation bands; (C)(F) middle section including segregation bands in the as-received S690QT

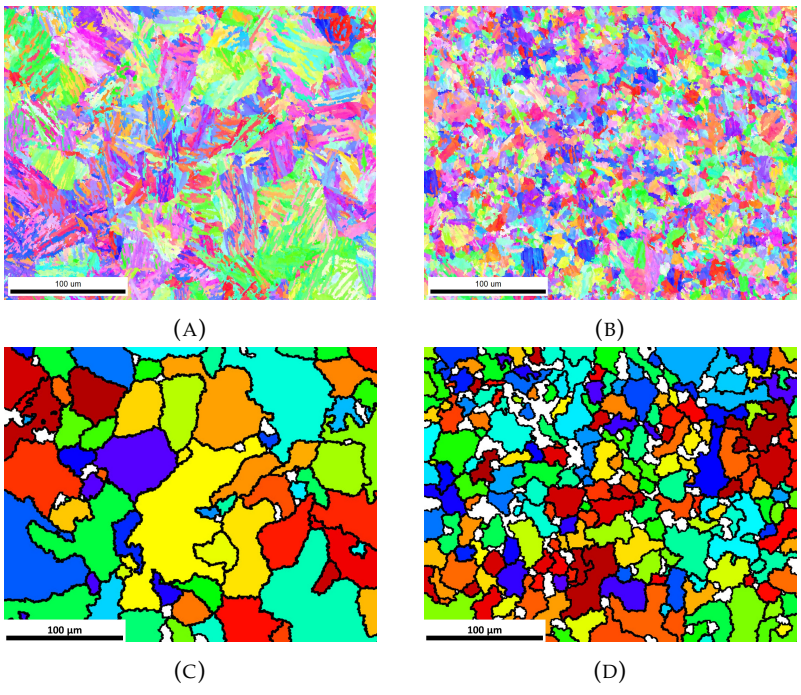

FIGURE 4.11: Comparison of middle section inverse pole figures and reconstructed PAGs for (A),(C) as-received material; (B),(D) heat treated material

The weighted average PAG aspect ratio in the through-thickness for the as-received material was determined to be 0.47. For the heat treated specimen no change in the weighted average PAG aspect ratio was observed. The major and minor axes in the as-received material showed distributions ranging between 3 to 60 μm and 2 to 34 μm respectively. In the heat treated specimen, the major and minor axes showed distributions ranging between 2 to 50 μm and 0.4 to 20 μm respectively. The average PAG aspect ratios, major and minor axes for the as-received and heat treated material are shown in Table 4.3. The frequency distribution of major and minor axes for the as-received and heat treated material are shown in Figure 4.12 and Figure 4.13. It is important to note that although 3 areas were analysed for each region of interest, the results from only one area are presented in the axes distribution. From literature it was seen that there was no standard method of representing the grain for PAGs. Both major and minor axes may be used to represent PAG sizes. In this study, the major axis was used to represent the PAG size. This is because the major axis gives an estimate of the largest grains in the material and these large grains have a direct effect on the mechanical properties. For the as-received material, the top section appeared to be comprised of smaller PAGs than the middle section. In the middle section, segregation bands were observed to have an insignificant effect on the PAG size. The PAG size of the heat treated material was determined to be 13.9 μm , demonstrating grain refinement by 41%.

Grain boundary misorientation angles for the as-received material and the heat treated material revealed interesting insights and is shown in Figure 4.14. Low angle misorientations are typically distributed between laths while high angle misorientation are distributed within PAG boundaries [89]. A large frequency of high angle misorientations were observed for both top and middle sections in the as-received material. These high angle misorientations are beneficial for the toughness of the material because they are effective barriers towards dislocation motion during deformation and cause cracks to deviate [82, 90]. The misorientations related to martensite and bainite boundaries vary between 48°- 55° for bainite and 57°- 65° for martensite [91] and are observed in the as-received material. The high angle misorientations include packet and block boundaries. Contrary to a study where large fractions of misorientations were present in the top section [70], in this study a higher frequency of high angle misorientations were observed in the middle section outside the segregation bands. In the heat treated material a large frequency of low angle misorientations (5°-10°) were observed. This indicates the presence of a high number of sub-block boundaries [92, 93]. A study concluded that for very small PAG sizes (< 10 μm) the entire PAG may be dominated by a single packet or block [94], which is in agreement with the microstructural observations of the heat treated material where large blocks were observed within the PAGs. For grains of this size, accommodation of transformation strain may occur across the austenite boundaries, which results in deformed PAGs after transformation to martensite. The deformation due to self-accommodation of strain can introduce dislocation boundaries with low misorientation [95]. In this study it is likely the refined PAGs were composed primarily of a single block, with a large number of sub-block structures resulting in a high frequency of low angle misorientations.

TABLE 4.3: Distribution of PAG aspect ratio, major axis and minor axis in as-received S690QT and heat treated material

Area	PAG aspect ratio	PAG major axis (μm)	PAG minor axis (μm)
Top	0.46 ± 0.02	19.0 ± 1.9	8.4 ± 0.3
Middle outside SB	0.47 ± 0.01	23.9 ± 0.1	10.8 ± 0.3
Middle including SB	0.47 ± 0.01	23.6 ± 1.3	10.7 ± 0.5
Heat treated material	0.47 ± 0.01	13.9 ± 0.1	6.3 ± 0.1

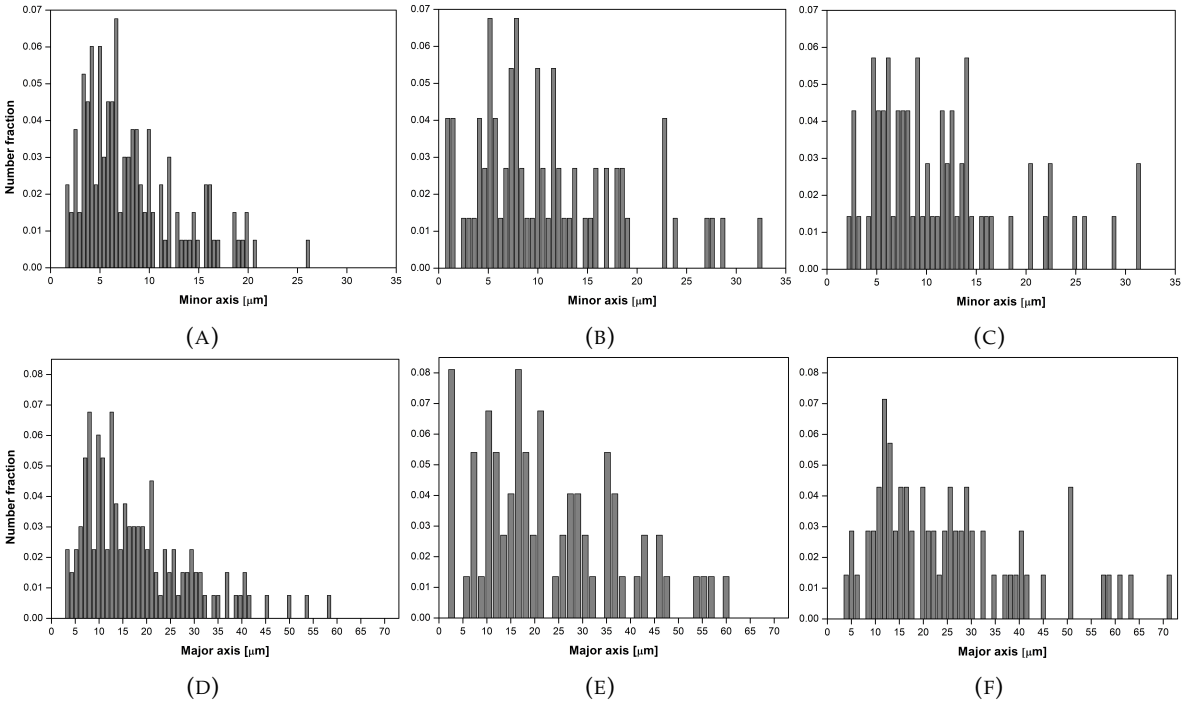

FIGURE 4.12: PAG minor and major axes distributions in the as-received material (A),(D) top section; (B),(E) middle section outside segregation bands; (C),(F) middle section including segregation bands

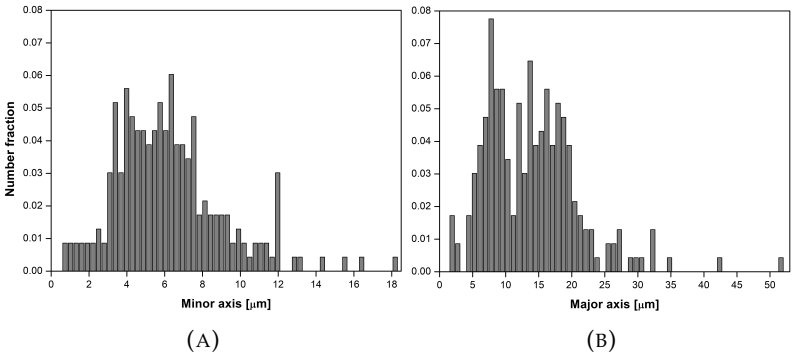

FIGURE 4.13: PAG minor and major axes distributions in the heat treated material (A) minor axis (B) major axis

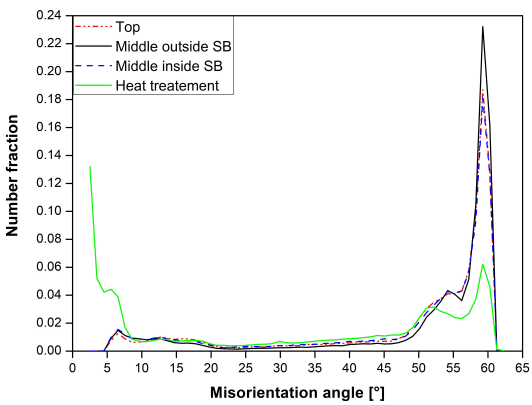

FIGURE 4.14: Misorientation distribution of as-received and heat treated material

4.2 Tensile properties

4.2.1 As-received material

Tensile tests performed on the as-received S690QT at -130 °C for orientations 0° (parallel), 45°and 90° (perpendicular) to the rolling direction revealed interesting insights. The variation of yield strength and ultimate tensile strengths with respect to the rolling direction are shown in Figure 4.15. For both top and middle sections, considering the scatters observed, it may be concluded that orientation with respect to the rolling direction did not affect the tensile properties. In general, the top section was observed to be stronger than the middle section. However, the difference in strengths was within 20 MPa, which was not very significant. The small difference in strengths may be attributed to coarser grains, larger number and area fraction of inclusions, and the presence of segregation bands in the middle section which may be detrimental to the tensile properties.

Due to the nature of testing which required the conversion of cross-head displacement travel into extensometer strains for the specimen with missing extensometer data, it was not possible to accurately determine the Young's modulus for each orientation. After the conversion the Young's modulus was observed to range between 96 to 160 GPa, which is outside of the range for high strength steels. This inaccuracy is likely due to elasticity from the testing apparatus not being eliminated completely in the conversion method. The average Young's modulus was instead calculated from the specimens with valid extensometer data and was determined to be 238 GPa at -130 °C for the as-received S690QT, which is in the expected range for this material.

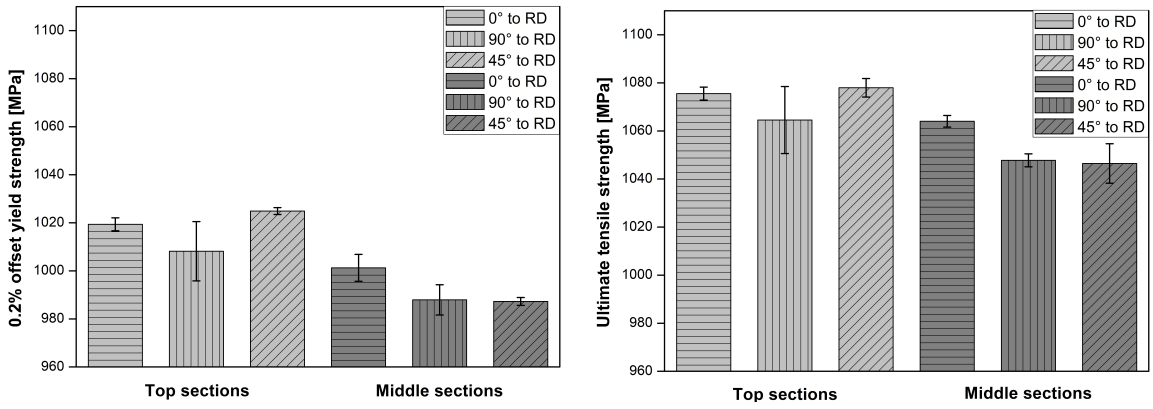

FIGURE 4.15: Effect of different orientations w.r.t rolling direction on (A) yield strength (B) ultimate tensile strength for as-received S690QT at -130°C

4.2.2 Heat treated material

For the middle section heat treated specimens at an orientation 90° to the rolling direction, tensile tests reported an improvement in yield and ultimate tensile strengths by 5% and 13% respectively. The effects of the heat treatment in comparison with the as-received material under the same conditions are shown in Figure 3.12. It is important to note that the tests were performed on the heat treated specimens at room temperature and the tensile properties were subsequently estimated at -130 °C using Equation 3.1 and Equation 3.2 in accordance with BS 7910 + A1 standard [76]. These results are consistent with the interpretations of the Hall-Petch equation, where tensile properties increase with grain refinement [25]. The improvement in tensile properties may also be attributed to the large fraction of low angle misorientations. Some studies have shown that high fractions of low angle misorientations can result in improvement of yield and tensile strengths [96, 97, 98]. Lath boundaries are low angle misorientations, which can result in accumulation of dislocations at these boundaries and effectively restrict transgranular movement of dislocations [99].

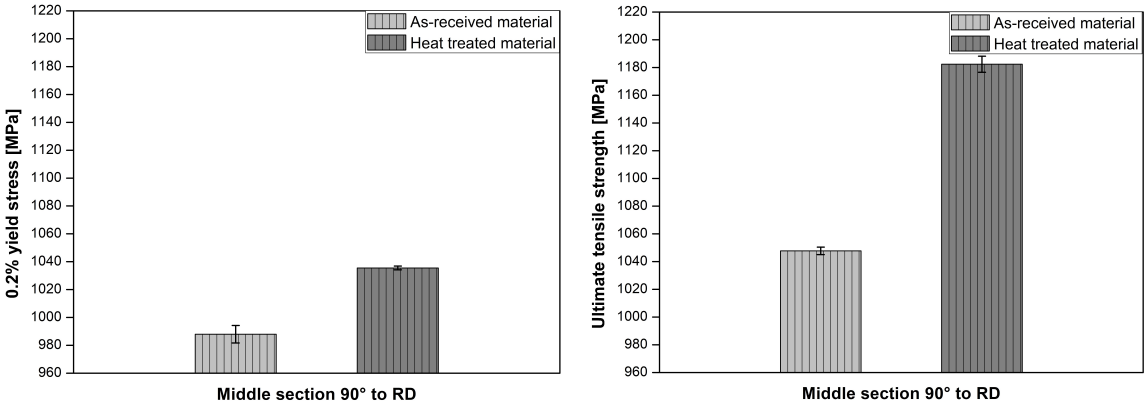

(A) (B)

FIGURE 4.16: Effect of heat treatment on (A) yield strength (B) ultimate tensile strength on the middle section 90° to the rolling direction at -130 °C

4.3 Fracture toughness

An overview of CTOD results at -130 °C for the as-received and heat treated materials is shown in Table 4.4 and Figure 4.17. The comparison of CTOD results at -130 °C for the middle section for as-received and heat treated material is shown in Figure 4.18.

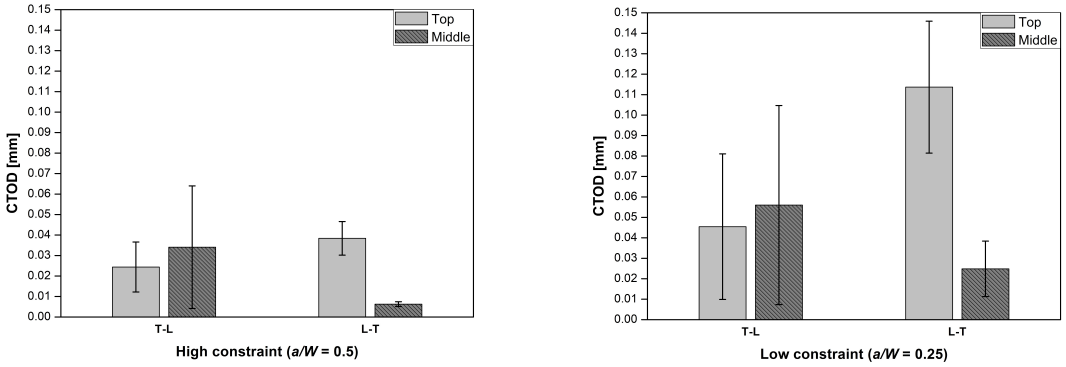

(A) (B)

FIGURE 4.17: CTOD results at -130 °C for the top and middle sections from the as-received S690QT in (A) high constraint (a/W = 0.5) (B) low constraint (a/W = 0.25) conditions at various specimen orientations

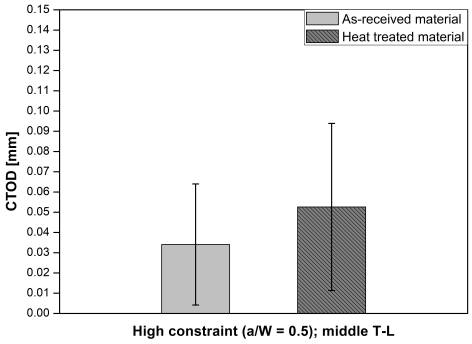

FIGURE 4.18: Comparison of middle section CTOD results at -130 °C for as-received and heat treated material in high constraint condition (a/W = 0.5) and T-L orientation

TABLE 4.4: CTOD results at -130 °C for different constraints and orientations at different thickness positions in the as-received and heat treated materials

Material	Condition	Position	Orientation and no. of specimens	Minimum CTOD (mm)	Maximum CTOD (mm)	Average CTOD (mm)
As-received	**High constraint (a/W = 0.50)**	**Top**	**T-L (3)**	0.01	0.03	0.02 ± 0.01
			L-T (3)	0.03	0.05	0.04 ± 0.01
		Middle	**T-L (10)**	0.01	0.1	0.03 ± 0.03
			L-T (5)	0.005	0.008	0.006 ± 0.001
	Low constraint (a/W = 0.25)	**Top**	**T-L (3)**	0.02	0.09	0.05 ± 0.04
			L-T (3)	0.09	0.16	0.11 ± 0.03
		Middle	**T-L (15)**	0.01	0.15	0.06 ± 0.04
			L-T (4)	0.01	0.04	0.02 ± 0.01
Heat treated	**High constraint (a/W = 0.50)**	**Middle**	**T-L (11)**	0.02	0.14	0.05 ± 0.04

4.3.1 As-received material

4.3.1.1 High constraint condition (*a/W* = 0.5)

In the high constraint condition (*a/W* = 0.5), a trend was observed for both top and middle sections in the fracture performance of various orientations. The middle section appeared to perform better than the top section in the T-L orientation, and was performed worse in the L-T orientation. However, it should be noted for the middle section in the T-L orientation a high scatter can be observed. Out of 10 specimens that were tested in this condition, 2 specimens presented high CTOD values and may be considered as outliers. After excluding these 2 specimens the middle section was found to have lower fracture toughness than the top section in both T-L and L-T orientations, which has a good agreement with another study employing a HSS with similar composition [40]. This can be attributed to the middle section containing coarser PAGs, inclusions in larger area and number fraction compared to the top section, and also due to the presence of segregation bands. The top section also appeared to possess a higher fraction of high angle misorientations, which is beneficial for high fracture toughness.

Comparing T-L and L-T orientations for the middle section, similarities in the CTOD values and their scatter led to the conclusion that the notch orientation with respect to the rolling direction did not have an effect on cleavage fracture toughness. For the top section, similar conclusions were drawn.

4.3.1.2 Low constraint condition (*a/W* = 0.25)

A similar trend was observed in the low constraint condition (*a/W* = 0.25). For the middle section T-L orientation, out of 15 specimens that were tested 4 specimens presented high CTOD values and may be considered outliers. After excluding the outliers and comparing T-L and L-T orientations for the middle section, it was concluded that the notch orientation with respect to the rolling direction did not have an effect on cleavage fracture toughness. Both notch orientations presented high scatter in the the top section.

In general, the specimens in low constraint condition were observed to be stronger than the specimens in the high constraint condition. This can be attributed to low hydrostatic stresses at the crack tip for the low constraint condition with reduced triaxiality [77, 100]. A high stress triaxiality is the most critical condition for fracture toughness [55]. A study has shown that the DBTT curve may shift due to the reduction in (*a/W*) [101]. It is likely that for the low constraint condition the DBTT curve was shifted, resulting in the testing temperature of -130 °C being transferred from the lower shelf to the transition region, which also explains the high scatter for both notch orientations in the top and middle sections [10].

4.3.2 Heat treated material: High constraint condition (*a/W* = 0.5)

The fracture toughness of the heat treated material from the middle section in T-L orientation was improved by 41%. The improvement in fracture toughness is consistent with the interpretations of the Hall-Petch equation, where toughness increases with grain refinement [25]. It is important to notice that the high scatter in this condition was retained, and can be attributed to the consistent morphology of randomly distributed segregation bands in both as-received and heat treated material.

4.3.3 Fractographic analysis

Fractographic analysis revealed that microstructural characteristics can contribute to cleavage fracture. SEM in combination with EDS revealed the presence of secondary phase constituents in the fracture initiation zones, likely influencing cleavage fracture. The cleavage fracture initiation zones were identified by following the characteristic river lines. In all cases cleavage facets were observed in the fracture initiation zones, originating from secondary phase constituents and propagating with river pattern steps. The following subsections show and describe the fracture surfaces of specimens with lowest CTOD values.

4.3.3.1 As-received material: High constraint (a/W = 0.5)

SEM micrographs of fracture surfaces of the as-received material at T-L and L-T orientations in high constraint condition (a/W = 0.5) are given in Figure 4.19 and Figure 4.20. In the top T-L surface EDS measurements in the initiation zone (CTOD = 0.01) revealed a O,C-rich region which is characteristic of the type of inclusions found in the as-received S690QT. Although no particles were seen visually, a void-like appearance was observed suggesting that a particle may have been pulled out. The initiation zone was measured to be located 58 μm from the pre-crack. In the top L-T surface the initiation zone (CTOD = 0.03) showed the presence of a particle and EDS measurements revealed a (Ca)(O,C) composition. The particle was measured to be located 166 μm from the pre-crack. In the middle T-L surface river line patterns suggested the fracture initiation zone (CTOD = 0.01) was at the pre-crack front. EDS measurements revealed a O,C-rich region and although no particles were seen visually, a void-like appearance was observed suggesting that a particle may have been pulled out. The initiation region was measured to be located 3 μm from the pre-crack. In the middle L-T surface river line patterns did not converge to a localized region and caused difficulty in identifying the fracture initiation zone. The initiation zone (CTOD = 0.005) appeared to be located at the pre-crack front and EDS measurements revealed a O,C-rich region and a particle was observed which had a deformed appearance. The initiation region was measured to be located 20 μm from the pre-crack. For the specimens with high CTOD values the initiation zones were measured to be farther away (at least 300 μm) from the pre-crack.

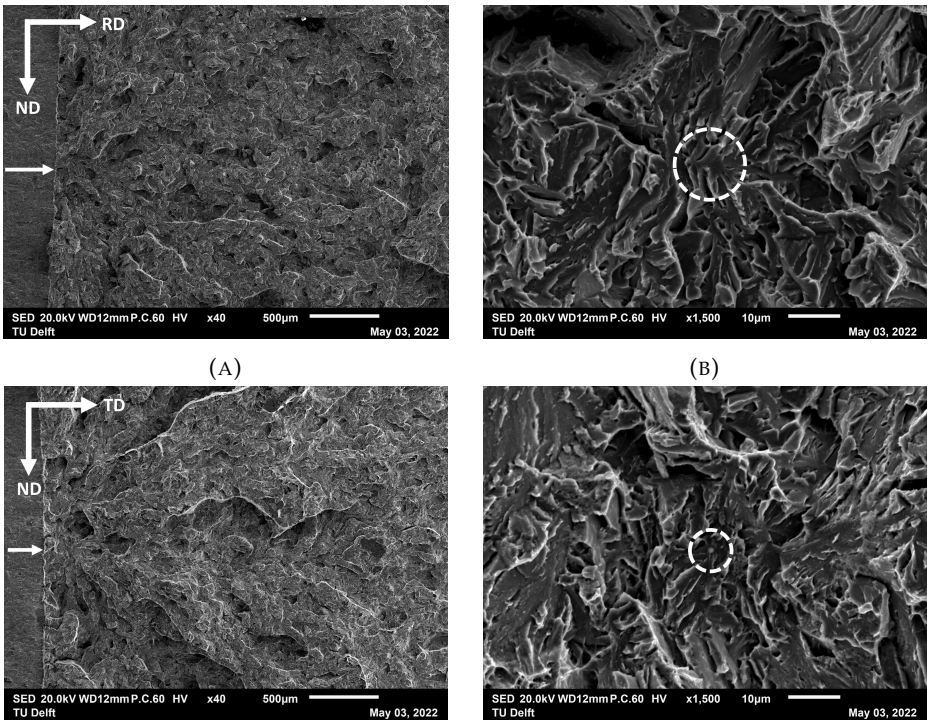

(A) (B)

(C) (D)

FIGURE 4.19: Top section fracture surface micrographs of as-received S690QT in high constraint condition (*a/W* = 0.5) (A),(B) T-L orientation (CTOD = 0.01); (C),(D) L-T orientation (CTOD = 0.03)

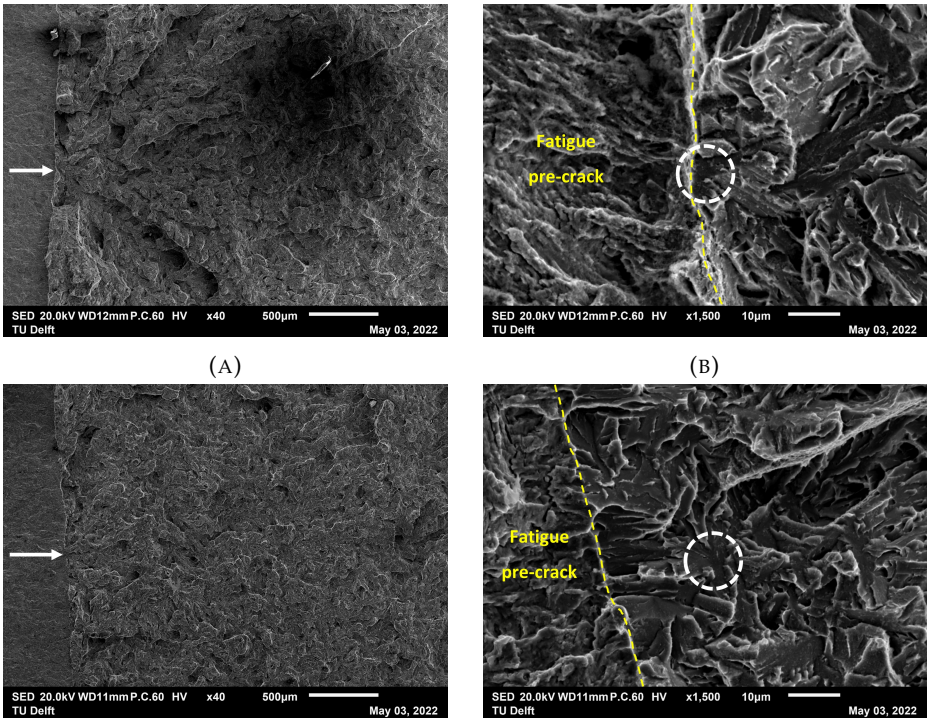

(A) (B)

(C) (D)

FIGURE 4.20: Middle section fracture surface micrographs of as-received S690QT in high constraint condition (*a/W* = 0.5) (A),(B) T-L orientation (CTOD = 0.01); (C),(D) L-T orientation (CTOD = 0.005)

4.3.3.2 As-received material: Low constraint (a/W = 0.25)

SEM micrographs of fracture surfaces of the as-received material at T-L and L-T orientations in low constraint condition (a/W = 0.25) are given in Figure 4.21 and Figure 4.22 respectively. In the top T-L surface EDS measurements revealed multiple points rich in C with traces of O. Although no particles could be visually observed, void-like appearances were observed in a few points suggesting particles may have been pulled out. The initiation zone (CTOD = 0.02) was measured to be located 95 μm from the pre-crack. In the top L-T surface EDS measurements revealed a point rich in C. The point where all the cleavage facets converged was observed to be depleted in Fe and showed no presence of other elements. The initiation region (CTOD = 0.09) was measured to be located 140 μm from the pre-crack. Similar to the high constraint condition, the river line patterns in the middle T-L surface suggested the fracture initiation zone (CTOD = 0.01) was very close to the pre-crack front. EDS measurements in the region were cleavage facets converged revealed a C-rich Fe-depleted region. The initiation region was measured to be located 12 μm from the pre-crack. Similarly the river line patterns for the middle L-T surface suggested the fracture initiation zone (CTOD = 0.01) was at the pre-crack front. EDS measurements revealed Fe-depleted zones rich in C. The initiation zone was measured to be located 5 μm from the pre-crack. In these surfaces the Fe-depletion observed through EDS is likely due to the presence of nano-carbides, which are too small to be observed in detail. Similar to the high constraint condition the initiation zones in specimens with high CTOD values were measured to be farther away (at least 300 μm) from the pre-crack. These initiation zones were also observed to be O,C-rich, similar to the initiation zones in the high constraint condition.

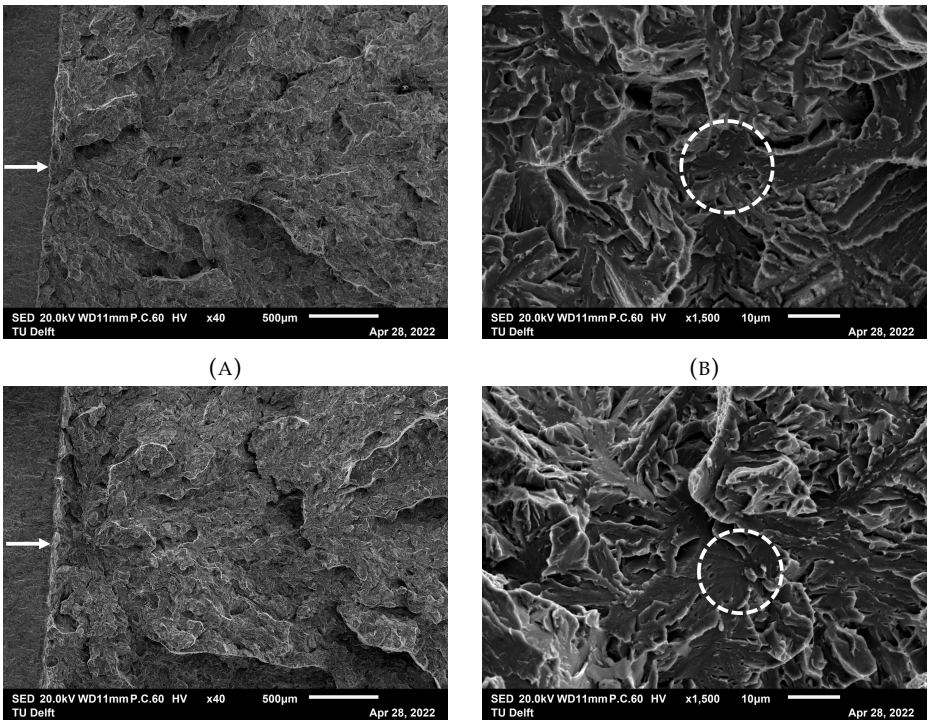

(A) (B)

(C) (D)

FIGURE 4.21: Top section fracture surface micrographs of as-received S690QT in low constraint condition (*a/W* = 0.25) (A),(B) T-L orientation (CTOD = 0.02); (C),(D) L-T orientation (CTOD = 0.09)

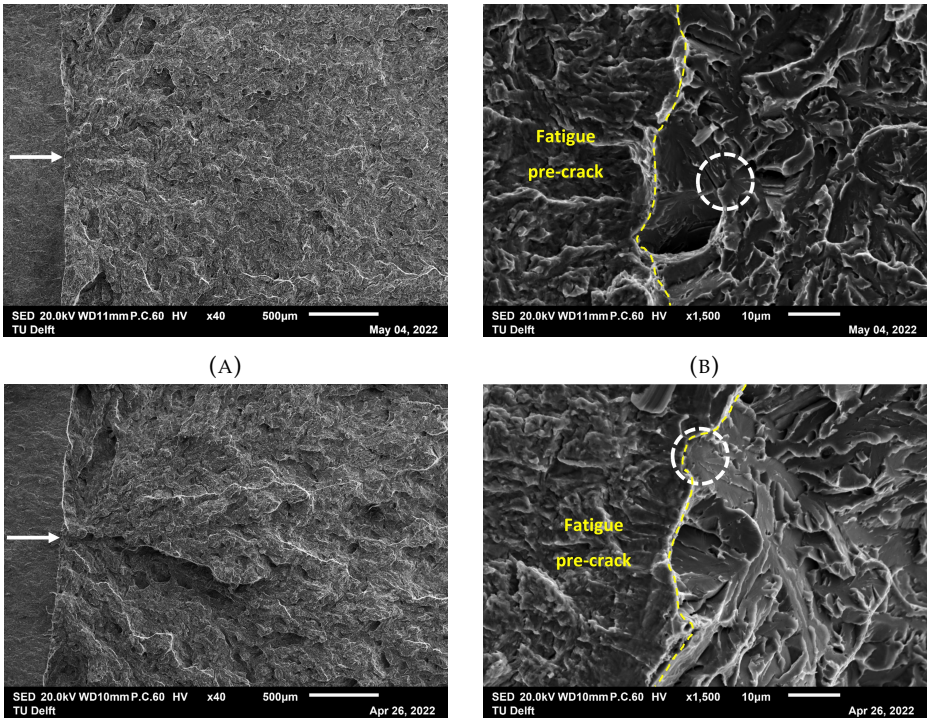

(A) (B)

(C) (D)

FIGURE 4.22: Middle section fracture surface micrographs of as-received S690QT in low constraint condition (*a/W* = 0.25) (A),(B) T-L orientation (CTOD = 0.01); (C),(D) L-T orientation (CTOD = 0.01)

4.3.3.3 Heat treated material: High constraint (a/W = 0.5)

SEM micrographs of the fracture surface of the heat treated material in T-L orientation (CTOD = 0.02) in high constraint condition (a/W = 0.5) are shown in Figure 4.23. EDS measurements revealed a C-rich point, but no Fe-depletion was observed. The initiation zone was measured to be located 75 μm from the pre-crack.

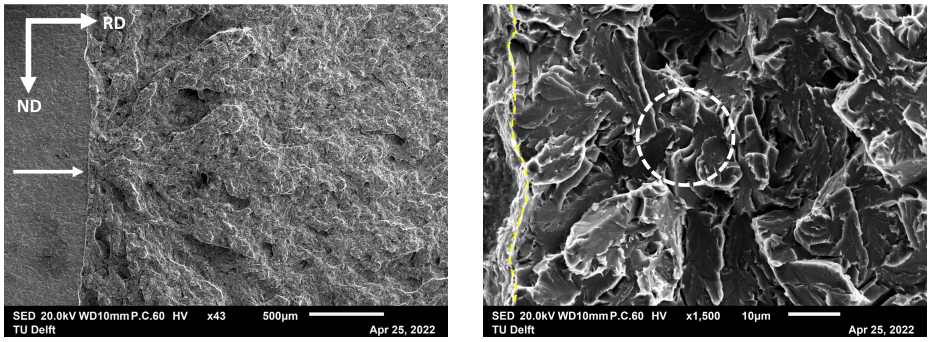

(A) (B)

FIGURE 4.23: Middle section fracture surface micrographs of the heat treated material in a high constraint middle T-L orientation (CTOD = 0.02)

It is evident that the dissimilarities in fracture behaviour for the as-received material at -130 °C can not simply be explained by examining fracture surfaces. Although the fracture initiation regions were characterized by the presence of O,C-rich regions which are known to promote brittle behaviour [44, 102], the constant presence of these secondary phase constituents do not explain the dissimilarities in fracture behavior. Underlying micro-mechanisms which promote cleavage fracture such as crack nucleation may depend on not only the presence of secondary phase particles, but also the orientation of the crack with respect to the rolling direction. It is likely that cracks started to nucleate in secondary phase constituents with high density of dislocation pileup, where local stresses are high and the failure criterion was critical plastic strain [55]. The low constraint condition proved to be stronger than the high constraint likely due to low hydrostatic stress at the crack tip which reduces triaxiality, improving toughness.

4.4 Summary

A brief comparison of the results from the middle section of the as-received and heat treated material is given in Table 4.5.

TABLE 4.5: Brief comparison for the as-received material and heat treated material from the middle section

Feature	As-received material	Heat treated material
Phases	Tempered martensitic-bainitic. Clear demonstration of the three-level hierarchy of laths, packets and blocks	Tempered martensitic-bainitic. Large blocks with laths observed to be aligned in a single direction
PAG size (μm)	23.7 ± 0.1	13.9 ± 0.1 (41% reduction)
Grain boundary misorientations	Large frequency of high angle misorientations, favorable for high fracture toughness	Large frequency of low angle grain boundaries, likely due to formation of sub-structure boundaries
Hardness (HV_3)	273 ± 7	309 ± 9 (13% improvement)
-130 °C tensile properties (MPa)	$RP_{0.2}$: 988 ± 3 UTS: 1048 ± 3	$RP_{0.2}$: 1036 ± 1 (5% improvement) UTS: 1182 ± 6 (13% improvement)
-130 °C CTOD (mm) High constraint (a/W = 0.5), T-L orientation	0.03 ± 0.03	0.05 ± 0.04 (41% improvement)
Fractographic analysis	O,C-rich regions in initiation zone, known to promote brittle behaviour	No Fe-depletion; C-rich region, known to promote brittle behaviour

Chapter 5

Conclusions and future recommendations

5.1 Conclusions

Based on the research objectives proposed in chapter 2, the following conclusions are drawn in this study:

- **Characterize the microstructure of the as-received S690QT HSS, and determine the tensile and fracture properties by testing at subzero temperatures.**

    1. Both top and middle sections were comprised of a tempered martensitic-bainitic microstructure, with the middle section likely containing a larger fraction tempered bainite.
    2. The middle section contained larger and more densely distributed inclusions than the top section. The most commonly found inclusions were of (Al,Mg)(O,N) composition.
    3. Segregation bands as a result of solute segregation of alloying elements were observed in the middle section. These bands were observed to be dispersed throughout the middle section.
    4. The PAG size increased at the middle section of the plate, due to the lower cooling rates experienced by the middle section during solidification. No significant grain refinement was observed inside the segregation bands.
    5. Through thickness micro-hardness measurements revealed a lower hardness at the middle section of the plate. This is attributed to the larger PAG sizes and lower fraction of tempered martensite in the middle section. Segregation bands did not appear to influence micro-hardness characteristics.
    6. Low temperature (-130 °C) tensile tests in the lower shelf revealed a weak middle section. This is attributed to larger PAG sizes, larger area and number fraction of inclusions, and presence of segregation bands in the middle section. The tensile properties were found to be independent of specimen orientation with respect to the rolling direction.
    7. Low temperature (-130 °C) fracture toughness tests in the lower shelf revealed a weak middle section. This is also attributed to larger PAG sizes, larger area and number fraction of inclusions, and presence of segregation bands in the middle section.

- **Investigate the microstructural, orientation and constraint effects on cleavage failure through fracture toughness tests.**

    1. In the high constraint condition (a/W = 0.5) for both top and middle sections, no significant differences were observed in for the different notch orientations with respect to the rolling direction.
    2. The low constraint condition (a/W = 0.25) which has a better representation of shallow defects found in offshore structures was associated with a higher fracture toughness compared to the high constraint condition. This is attributed to low hydrostatic stresses at the crack tip, which reduced triaxiality.
    3. In the low constraint condition for the middle section, the notch orientation with respect to the rolling direction did not have an effect on fracture toughness. For both top and middle sections, a high scatter is observed. It is likely that the reduction in a/W caused the DBTT curve to shift from the lower shelf towards the transition region.
    4. No conclusions could be drawn from fractographic analysis of both constraint conditions. The constant presence of O,C-rich constituents in the initiation zones did not allow for fractography to be used as a means to distinguish the fracture behaviour between specimens with high and low fracture toughnesses from the same test conditions.
    5. It is likely that cracks nucleated in secondary phase constituents with a high density of dislocation pileups. In these particles, the critical failure criterion is the plastic strain.

- **Perform isoparametric grain refinement to study the effect of grain size on cleavage fracture behavior.**

    1. Isoparametric grain refinement by 41% was successfully achieved in the middle section. The microstructure was observed to be a tempered martensitic-bainitic microstructure, composed of large blocks with laths aligned in a specific direction. This is contrary to the as-received material where the three-level morphology composed of laths, packets and blocks within the martensite were observed.
    2. The grain refinement improved micro-hardness by 13%. Similar to the as-received material, a large scatter was observed in the hardness results and is attributed to the presence of segregation bands, which were found to be dispersed throughout the middle section. The width of these bands was found to remain unchanged after the grain refinement.
    3. Low temperature (-130 °C) tensile and yield strengths were improved by 5% and 13% respectively. It is likely that the refined grains and large fraction of low angle misorientations contributed to the tensile strengthening mechanism by restricting transgranular dislocation motion.
    4. Low temperature (-130 °C) average fracture toughness was improved by 41% in the high constraint condition (a/W = 0.5) and T-L orientation. Although the improvement seemed to be significant, it was not sufficient to shift the failure from the lower shelf towards the upper shelf, likely due to the presence of secondary phase constituents which function as crack nucleation zones. A large scatter was observed which suggests that the improvement in fracture toughness may not be significant.

5. A large fraction of low angle misorientations were observed in the refined grains, accompanied by a reduction in high angle misorientations compared to the as-received material. Refined grains and high angle misorientations are favorable for high strength and toughness. It is likely that the effects of grain refinement may have compensated for the loss in toughness due to lower fraction of high angle misorientations, and thereby contributing to a small improvement in cleavage fracture toughness.
6. Fractographic analysis revealed the presence of a C-rich region, likely a carbide in the fracture initiation zone. The specimens with lowest fracture toughness were distinguished by initiation zones located close to the pre-crack front while the initiation zones were far from the pre-crack in the specimens with high fracture toughness. No conclusions could be drawn on the fracture behaviour purely on the basis of secondary phase constituents due to their constant presence in initiation zones.

- **Provide a basis on microstructure-cleavage fracture relationship of high strength steels for future work to improve the performance of these steels.**

1. Microstructural features such as grain size, inclusions and segregation bands influence cleavage fracture toughness.
2. The notch and specimen orientations with respect to the rolling direction do not affect the fracture toughness and tensile properties
3. The crack depth to width ratio (a/W) has an effect on the cleavage fracture toughness. Reduction in a/W may cause a shift from the lower shelf towards the transition region, resulting in cleavage fracture becoming harder to predict and control.
4. Even with isoparametric grain refinement, constant presence of secondary phase constituents can promote brittle behaviour.

5.2 Future recommendations

In order to further extend the knowledge, some recommendations are made to aid in further research:

- Nano-indentation may provide a better estimate of the hardness within the segregation bands. In this study the segregation bands were measured between 25 to 200 μm and diagonal of the micro-indent measures in the range of 140 μm. It is evident that micro-hardness does not provide an accurate estimate of hardness within these bands.
- The stress fields within and around segregation bands may play an important role in the fracture toughness. Further analysis on the fracture surfaces of the outliers may reveal insights.
- Investigate the effect of larger inclusions (5 - 10 μm) to understand if inclusions are the main driving force behind cleavage failure.
- Grain boundary engineering may be applied in order to engineer misorientations which are favorable for certain applications. It is possible to generate high or low angle misorientations through mechanical deformation during heat treatments. For a high fracture toughness high angle misorientations are desirable. In this study, a large fraction of low angle misorientations were observed in the heat treated material. Grain boundary engineering can be performed to generate high angle misorientations, which may have a complementary effect with refined grains to further increase fracture toughness.
- Additionally, study the effects of increasing grain size to observe if the effects are reversed. It is likely that a higher fraction of high angle misorientations may form in coarsened grains, which can contribute to increased toughness.

Chapter 6

Annex

6.1 Cross-head travel to extensometer strain conversion

Results from tensile tests are typically processed using stress and strain data from the extensometer. Although the cross-head also provides strains in the form of cross-head travel, the Young's modulus for a test specimen may not be calculated from these displacements due to elasticity contributed by the test setup. Therefore, for the specimens with invalid extensometer data, a method was designed to eliminate elasticity contributed by the test setup to the specimen strain. A comparison of tensile curves for valid and invalid extensometer data are shown in Figure 6.1.

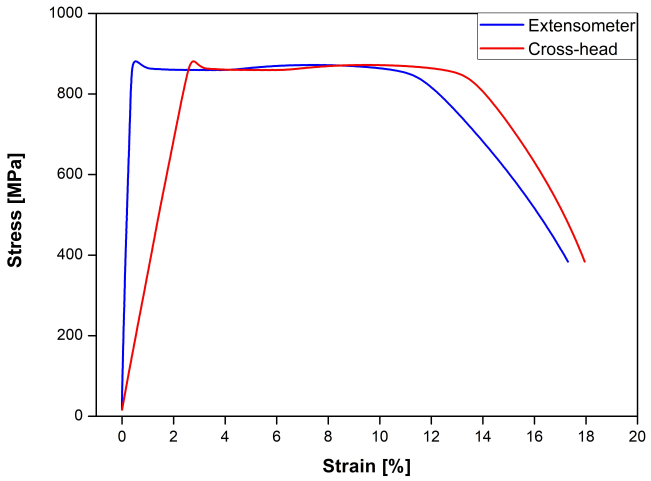

(A)

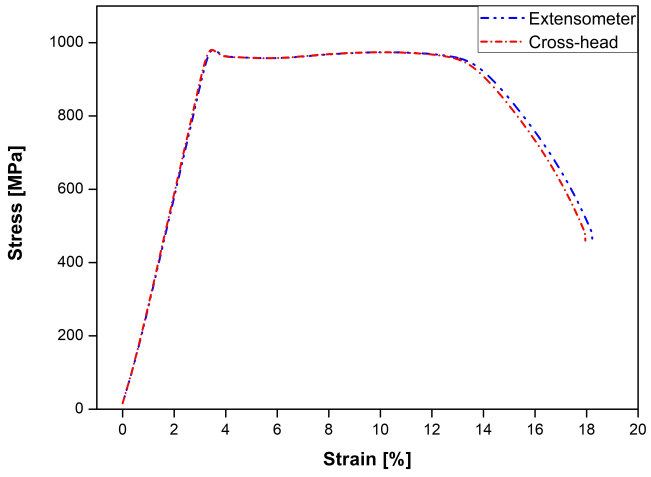

(B)

FIGURE 6.1: Comparison of tensile curves (A) valid extensometer data (B) extensometer data reads the cross-head displacement

1. In order to eliminate the elasticity contributed by the test setup, specimens with valid extensometer data were used to develop the method. An important feature in this method is that force and displacement curves were used instead of stress and strain because the area of components inside the test setup are unknown. First, the displacement of the entire specimen which includes the region outside the extensometer clips (gauge) was obtained by multiplying the extensometer strain with the total specimen length. This is shown in Figure 6.2.

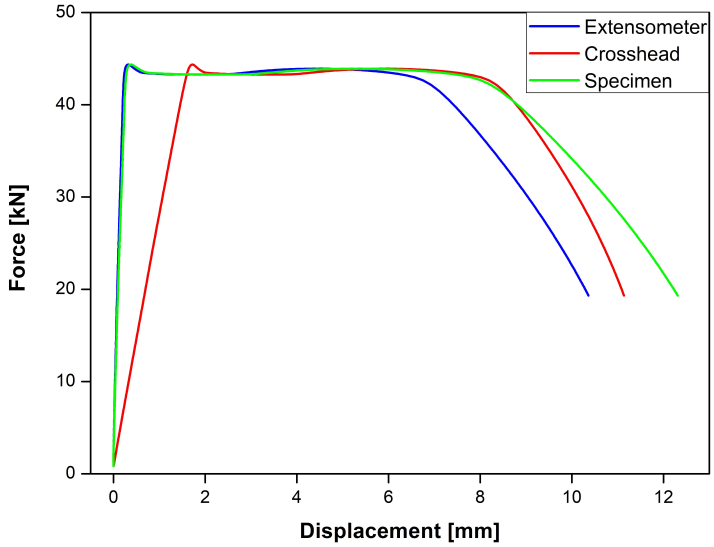

FIGURE 6.2: Displacement for the entire specimen after multiplication by total length

2. Subsequently, the specimen displacement is subtracted from the cross-head travel in order to obtain the displacement of the test setup. The resulting elastic region is shown in Figure 6.3.

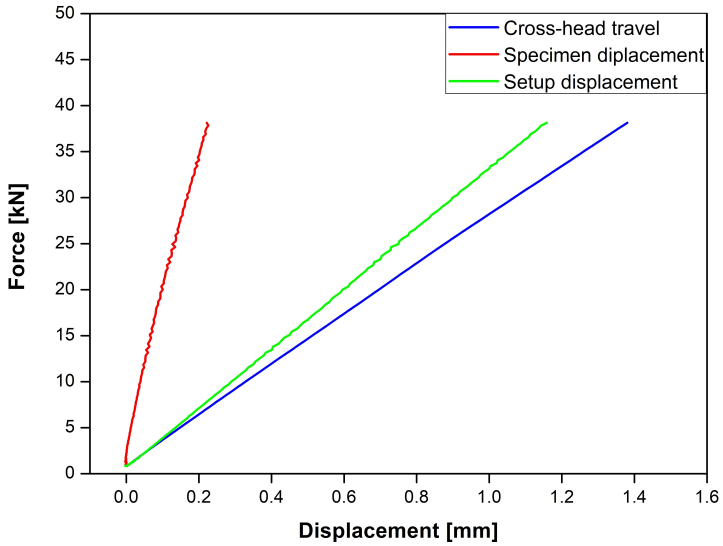

FIGURE 6.3: Linear region illustrating displacement of the test setup

3. The slope of the elastic region from the displacement of the test setup provides a measure of the elasticity of the test setup. This elasticity is not to be confused with Young's modulus. The corrected specimen displacement is subsequently calculated by subtracting the elasticity of the test setup from each displacement data point in the cross-head travel. This is described in Equation 6.1

$$d_{corrected} = d_{cross} - \left(\frac{F}{m}\right) \tag{6.1}$$

Where $d_{corrected}$ is the corrected specimen displacement data point, d_{cross} is the cross-head travel displacement data point, F is the force at the specified data point and m is the slope of the elastic region from the displacement of the test setup. Since this displacement is for the entire length of the specimen, it is reverted to the gauge by dividing by the total length of the specimen.

4. The result is a shift in the cross-head travel curve towards the extensometer stress-strain curve which allows for the calculation of Young's modulus. The corrected stress-strain curve is shown in

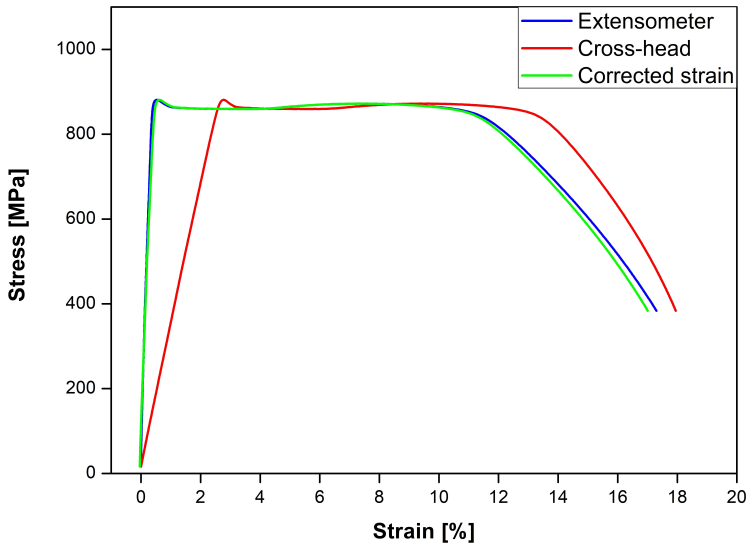

FIGURE 6.4: Comparison of middle section CTOD results at -130 °C for as-received and heat treated material in high constraint condition ($a/W = 0.5$) and T-L orientation

5. This method was followed for all specimens with valid extensometer data. To have the estimate of average elasticity of the test setup, the mean of all values of the slope m were taken. For the specimens with invalid data, Equation 6.1 was used directly with cross-head travel displacement.

Bibliography

[1] Huiyong Ban and Gang Shi. A review of research on high-strength steel structures. In Proceedings of the Institution of Civil Engineers: Structures and Buildings, volume 171, pages 625–641. ICE Publishing, 2018.

[2] Jian Xun Fu, Le Chen, Chang Jin Wu, and Yan Xin Wu. Marine engineering steels—properties requirements and evaluation. Applied Mechanics and Materials, 692:465–469, 2014.

[3] J Billingham, J. V Sharp, and J Spurrier. Review of the performance of high strength steels used offshore. Technical report, Cranfield University.

[4] R Kuziak, R Kawalla, and S Waengler. Advanced high strength steels for automotive industry. Archives of Civil and Mechanical Engineering, 8(2), 2008.

[5] Tapas Kumar, Roy Basudev Bhattacharya, Chiradeep Ghosh, S K Ajmani, and Applications Processing. Lecture Notes in Mechanical Engineering Advanced High Strength Steel. Technical report.

[6] Smith Metal. EN8 Technical Data Sheet. Technical report, 2014.

[7] Kate Hickey. Schematic showing amount of springback is proportional to stress.

[8] ArcelorMittal. Industeel Steel Solutions for high strength applications. Technical report, 2016.

[9] Raghu Shant, Tushal Kyada, and Rajesh Goyal. Understanding the Delamination and Its Effect on Charpy Impact Energy in Thick Wall Linepipe Steel. Journal of Materials and Metallurgical Engineering, 4(1), 2014.

[10] V. A. Popovich and I. M. Richardson. Fracture toughness of welded thick section high strength steels and influencing factors. In TMS Annual Meeting, pages 1031–1038. Minerals, Metals and Materials Society, 2015.

[11] Fujian Guo, Xuelin Wang, Jingliang Wang, R. D.K. Misra, and Chengjia Shang. The significance of central segregation of continuously cast billet on banded microstructure and mechanical properties of section steel. Metals, 10(1), 1 2020.

[12] Huibin Liu, Hanqian Zhang, and Jinfu Li. Thickness dependence of toughness in ultra-heavy low-alloyed steel plate after quenching and tempering. Metals, 8(8), 8 2018.

[13] Abdul Maleque Mohd and Sapuan Salit. Materials Selection and Design. Springer, 2013.

[14] Geralf Hütter. Multi-Scale Simulation of Crack Propagation in the Ductile-Brittle Transition Region. PhD thesis, Technische Universität Bergakademie Freiberg, 2013.

[15] J. O. Aweda, T. A. Orhadahwe, and I. O. Ohijeagbon. Rapid Cyclic Heating of Mild Steel and its Effects on Microstructure and Mechanical properties. In IOP Conference Series: Materials Science and Engineering, volume 413. Institute of Physics Publishing, 9 2018.

[16] Bo Jiang, Meng Wu, Mai Zhang, Fan Zhao, Zhigang Zhao, and Yazheng Liu. Microstructural characterization, strengthening and toughening mechanisms of a quenched and tempered steel: Effect of heat treatment parameters. Materials Science and Engineering A, 707:306–314, 11 2017.

[17] Eleni Gogou. Use of High Strength Steel Grades for Economical Bridge Design. Technical report, 2012.

[18] Kurt Lange. Handbook of Metal Forming - Society of manufacturing engineers. McGraw-Hill, Inc., 1985.

[19] Sakari Pallaspuro. On the factors affecting the ductile-brittle transition in as-quenched fully and partially martensitic low-carbon steels. PhD thesis, University of Oulu, 2018.

[20] Siddhartha. Ray. Introduction to Rolling Process. Technical report, Cambridge University Press, Cambridge, 2016.

[21] George. E Totten and Rafael Colas. Encyclopedia of Iron, Steel, and their Alloys. CRC Press, 2016.

[22] George. E Totten. Steel Heat Treatment: Metallurgy and Technologies. CRC Press, 2006.

[23] Enda Keehan. Effect of Microstructure on Mechanical Properties of High Strength Steel Weld Metals. Technical report, 2004.

[24] G. B. Olson. Martensite: a tribute to Morris Cohen. Number SPEC. ISS. ASM International, 1992.

[25] Günter Gottstein. Physical Foundations of Materials Science. Springer Berlin Heidelberg, 2004.

[26] J W Morris. The Influence of Grain Size on the Mechanical Properties of Steel. Technical report, University of California, Berkley, 2001.

[27] Chandra Prakash, Hongsuk Lee, Milad Alucozai, and Vikas Tomar. An analysis of the influence of grain boundary strength on microstructure dependent fracture in polycrystalline tungsten. International Journal of Fracture, 199(1):1–20, 5 2016.

[28] Jeongho Han, Alisson Kwiatkowski da Silva, Dirk Ponge, Dierk Raabe, Sang Min Lee, Young Kook Lee, Sang In Lee, and Byoungchul Hwang. The effects of prior austenite grain boundaries and microstructural morphology on the impact toughness of intercritically annealed medium Mn steel. Acta Materialia, 122:199–206, 1 2017.

[29] Y Prawoto, N Jasmawati, and K Sumeru. Effect of Prior Austenite Grain Size on the Morphology and Mechanical Properties of Martensite in Medium Carbon Steel. Technical Report 5, 2012.

[30] Muhammad Aatif Irshad, Christer Burman, and Jens Bergström. The effect of prior austenite grain size on the machinability of a pre-hardened mold steel. Technical report, 2011.

[31] S. Morito, H. Tanaka, R. Konishi, T. Furuhara, and T. Maki. The morphology and crystallography of lath martensite in Fe-C alloys. Acta Materialia, 51(6):1789–1799, 4 2003.

[32] S. Morito, X. Huang, T. Furuhara, T. Maki, and N. Hansen. The morphology and crystallography of lath martensite in alloy steels. Acta Materialia, 54(19):5323–5331, 11 2006.

[33] Wen Lan Li, J. C.M. Li, and Wen Lan Li. The effect of grain size on fracture toughness. Philosophical Magazine A: Physics of Condensed Matter, Structure, Defects and Mechanical Properties, 59(6):1245–1261, 1989.

[34] Meysam Naghizadeh and Hamed Mirzadeh. Effects of Grain Size on Mechanical Properties and Work-Hardening Behavior of AISI 304 Austenitic Stainless Steel. Steel Research International, 90(10), 10 2019.

[35] André Luiz Vasconcellos Da Costa E Silva. The effects of non-metallic inclusions on properties relevant to the performance of steel in structural and mechanical applications, 4 2019.

[36] Edgar. C Bain. Functions of the Alloying Elements in Steel. American Society for Metals, 1939.

[37] Changsheng Li, Guojun Cai, Dongge Wang, and Yongkang Zhou. Effect of precipitates on mechanical properties for annealed Fe-19Cr-2Mo-Nb-Ti ferritic stainless steel. In Procedia Manufacturing, volume 15, pages 1604–1611. Elsevier B.V., 2018.

[38] Pierre Michaud, Denis Delagnes, Pascal Lamesle, M H Mathon, Christophe Levaillant, P Michaud, D Delagnes, P Lamesle, MH Mathon, and C Levaillant. The effect of the addition of alloying elements on carbide precipitation and mechanical properties in 5% chromium martensitic steels. Acta Materialia, 55(14):4877–4889, 2007.

[39] M. Venkatesh Kannan, N. Arivazhagan, M. Nageswara Rao, and G. Madhusudhan Reddy. Effect of inclusions on microstructure and mechanical behavior of multi-pass welded naval grade steel. Proceedings of the Institution of Mechanical Engineers, Part L: Journal of Materials: Design and Applications, 234(8):1071–1083, 8 2020.

[40] V. M. Bertolo, Q. Jiang, C. L. Walters, and V. A. Popovich. Effect of microstructure on cleavage fracture of thick-section quenched and tempered S690 high-strength steel. In Minerals, Metals and Materials Series, volume PartF1, pages 155–168. Springer, 2020.

[41] Lei Zhang and Thomas Kannengiesser. Austenite grain growth and microstructure control in simulated heat affected zones of microalloyed HSLA steel. Materials Science and Engineering A, 613:326–335, 9 2014.

[42] Joseph Maciejewski. The Effects of Sulfide Inclusions on Mechanical Properties and Failures of Steel Components. Journal of Failure Analysis and Prevention, 15(2):169–178, 4 2015.

[43] Hyung-Ha Jin, Jae-Hyoek Shim,) Young, Whan Cho, and Hu-Chul Lee. Formation of Intragranular Acicular Ferrite Grains in a Ti-containing Low Carbon Steel. Technical report, 2003.

[44] J. R. (Joseph R.) Davis. Alloying : understanding the basics. ASM International, 2001.

[45] Takashi Matsuoka and Kakluwosuke Yamamori. Metallurgical Aspects Strength Steel Sheets in Cold Rolled High. Metallurgical Transactions A, 6, 1975.

[46] Benjamin Josef Schäfer, Petra Sonnweber-Ribic, Hamad Ul-Hassan, and Alexander Hartmaier. Micromechanical modeling of fatigue crack nucleation around non-metallic inclusions in martensitic high-strength steels. Metals, 9(12), 12 2019.

[47] T. Sakai, N. Oguma, and A. Morikawa. Microscopic and nanoscopic observations of metallurgical structures around inclusions at interior crack initiation site for a bearing steel in very high-cycle fatigue. In Fatigue and Fracture of Engineering Materials and Structures, volume 38, pages 1305–1314, 11 2015.

[48] D P Fairchild, D G Howden, and W A T Clark. The Mechanism of Brittle Fracture in a Microalloyed Steel: Part I. Inclusion-Induced Cleavage. Metallurgical and Material Transactions A, 31A(642), 2000.

[49] Chao Gu, Junhe Lian, Yanping Bao, Wei Xiao, and Sebastian Münstermann. Numerical study of the effect of inclusions on the residual stress distribution in high-strength martensitic steels during cooling. Applied Sciences (Switzerland), 9(3), 1 2019.

[50] Hsuan Han Lai and Weite Wu. Practical examination of the welding residual stress in view of low-carbon steel welds. Journal of Materials Research and Technology, 9(3):2717–2726, 2020.

[51] Michael Janssen, Jan Zuidema, and Russell Wanhill. Fracture Mechanics: Second edition. Spoon Press, 2017.

[52] P J G Schreurs. Fracture Mechanics. Technical report, Eindhoven University of Technology, 2012.

[53] C Briant. Intergranular Fracute In Metals. Kournal de Physique Colloques, 49, 1988.

[54] Fracture processes of aerospace materials. In Adrian .P Mouritz, editor, Introduction to Aerospace Materials, pages 428–453. Woodhead Publishing, 2012.

[55] Vivien J. H. Chen and R. Cao. Micromechanism of cleavage fracture of metals. 2015.

[56] A. A Griffith. The phenomena of rupture and flow in solids. Philosophical Transactions of the Royal Society of London, 221, 1921.

[57] A. A Wells. Application of fracture mechanics at and beyond general yielding. British Welding Journal, 10, 1963.

[58] T. L Anderson. Fracture Mechanics - Fundamentals and applications. Taylor & Francis, 2005.

[59] Philippa Moore and Geoff Booth. The Welding Engineer's Guide to Fracture and Fatigue. Woodhead Publishing, 2015.

[60] E8/E8M-16a: Standard Test Methods for Tension Testing of Metallic Materials. Technical report, ASTM International.

[61] Jia Bao Yan, J. Y.Richard Liew, Min Hong Zhang, and Jun Yan Wang. Mechanical properties of normal strength mild steel and high strength steel S690 in low temperature relevant to Arctic environment. Materials and Design, 61:150–159, 2014.

[62] WeeLiam Khor. Crack tip opning displacement (CTOD) in single edge notched bend (SEN(B)). PhD thesis, Brunel University London, 2018.

[63] ISO:12135: Metallic materials - Unified method of test for the determination of quasistatic fracture toughness. Technical report, International Standard, 2015.

[64] E1820-11: Standard Test Method for Measurement of Fracture Toughness.

[65] Zuopeng Zhao, Pengfei Xu, Hongxia Cheng, Jili Miao, and Furen Xiao. Characterization of microstructures and fatigue properties for dual-phase pipeline steels by gleeble simulation of heat-affected zone. Materials, 12(12), 6 2019.

[66] Gleeble simulator. Https://www.gleeble.com/500-series.html.

[67] Shu-Qing Xing, Chen Zheng-Zong", and M A Yong-Iin;. High Temperature Rapid Tempering Process of SS400 Steel With Thermomechanical Simulation Tester. Journal of Iron and Steel Research, International, 19(2):43–49, 2012.

[68] Qingfeng Ding, Yuefeng Wang, Qingfeng Wang, and Tiansheng Wang. Simulation study on thermo-mechanical controlled process of 800 MPa-grade steel for hydropower penstocks. Metals, 6(9), 9 2016.

[69] Martin Detrois, Joshua McCarley, Stoichko Antonov, Randolph C. Helmink, Robert L. Goetz, and Sammy Tin. Comparative study of high-temperature grain boundary engineering of two powder-processed low stacking-fault energy Ni-base superalloys. Materials at High Temperatures, 33(4-5):310–317, 6 2016.

[70] Virgínia Bertolo, Quanxin Jiang, Sebastian Scholl, Roumen H. Petrov, Ude Hangen, Carey Walters, Jilt Sietsma, and Vera Popovich. A comprehensive quantitative characterisation of the multiphase microstructure of a thick-section high strength steel. Journal of Materials Science, 57(13):7101–7126, 4 2022.

[71] V. Sinha, E. J. Payton, M. Gonzales, R. A. Abrahams, and B. S. Song. Delineation of Prior Austenite Grain Boundaries in a Low-Alloy High-Performance Steel. Metallography, Microstructure, and Analysis, 6(6):610–618, 12 2017.

[72] E1245-03: Standard Practice for Determining the Inclusion or Second-Phase Constituent Content of Metals by Automatic Image Analysis. Technical report, ASTM International.

[73] E112-13: Standard Test Methods for Determining Average Grain Size. Technical report, ASTM International.

[74] Cyril Cayron. ARPGE: A computer program to automatically reconstruct the parent grains from electron backscatter diffraction data. Journal of Applied Crystallography, 40(6):1183–1188, 11 2007.

[75] Sasan Sattarpanah Karganroudi, Bahman Hatami Nasab, Davood Rahmatabadi, Mina Ahmadi, Mohammad Delshad Gholami, Mehdi Kasaeian-Naeini, Ramin Hashemi, Ahmad Aminzadeh, and Hussein Ibrahim. Anisotropic behavior of Al1050 through accumulative roll bonding. Materials, 14(22), 11 2021.

[76] BS 7910:2013+A1:2015: Guide to methods for assessing the acceptability of flaws in metallic structures. BSI Standards Publication, 2015.

[77] Inoslav Rak. CTOD toughness evaluation of hyperbaric repair welds made under severe conditions. Structural Intergrity and Life, 2016.

[78] Lauralice de Campos Franceschini. Canale, R. A. (Rafael Agnelli) Mesquita, and George E. Totten. Failure analysis of heat treated steel components. ASM International, 2008.

[79] Sumit Ghosh and Suhrit Mula. Thermomechanical processing of low carbon Nb-Ti stabilized microalloyed steel: Microstructure and mechanical properties. Materials Science and Engineering A, 646:218–233, 10 2015.

[80] Myeong Heom Park, Akinobu Shibata, and Nobuhiro Tsuji. Challenging Ultra Grain Refinement of Ferrite in Low-C Steel Only by Heat Treatment. Frontiers in Materials, 7, 11 2020.

[81] Zheng Lv, Xue Ping Ren, Zhi Hong Li, Zi Ming Lu, and Min Min Gao. Effects of two different cyclic heat treatments on microstructure and mechanical properties of Ti-V microalloyed steel. Materials Research, 18(2):304–312, 3 2015.

[82] Javier Hidalgo and Maria Jesus Santofimia. Effect of Prior Austenite Grain Size Refinement by Thermal Cycling on the Microstructural Features of As-Quenched Lath Martensite. Metallurgical and Materials Transactions A: Physical Metallurgy and Materials Science, 47(11):5288–5301, 11 2016.

[83] Igor Vieira and Emmanuel De Moor. Tempering response of bainitic and martensitic microstructures. In Minerals, Metals and Materials Series, number 9783319521312, pages 791–799. Springer International Publishing, 2017.

[84] R N Caron and G Krauss. The Tempering of Fe-C Lath Martensite. Technical report.

[85] Hiromoto Kitahara, Rintaro Ueji, Nobuhiro Tsuji, and Yoritoshi Minamino. Crystallographic features of lath martensite in low-carbon steel. Acta Materialia, 54(5):1279–1288, 3 2006.

[86] M. Tamizi, M. Pouranvari, and M. Movahedi. Welding metallurgy of martensitic advanced high strength steels during resistance spot welding. Science and Technology of Welding and Joining, 22(4):327–335, 5 2017.

[87] Carola Celada-Casero, Jilt Sietsma, and Maria Jesus Santofimia. The role of the austenite grain size in the martensitic transformation in low carbon steels. Materials and Design, 167, 4 2019.

[88] Xiang Wang, Hatem S. Zurob, Guang Xu, Qibin Ye, Olivier Bouaziz, and David Embury. Influence of microstructural length scale on the strength and annealing behavior of pearlite, bainite, and martensite. Metallurgical and Materials Transactions A: Physical Metallurgy and Materials Science, 44(3):1454–1461, 3 2013.

[89] Giancarlo Sanchez Chavez, Segen Farid Estefen, Tetyana Gurova, Anatoli Leontiev, Lincoln Silva Gomes, and Suzana Bottega Peripolli. Redistribution of grain boundary misorientation and residual stresses of thermomechanically simulated welding in an intercritically reheated coarse grained heat affected zone. Metals, 11(11), 11 2021.

[90] Xiucheng Li, Guangyi Lu, Qichen Wang, Jingxiao Zhao, Zhenjia Xie, Raja Devesh Kumar Misra, and Chengjia Shang. The effects of prior austenite grain refinement on strength and toughness of high-strength low-alloy steel. Metals, 12(1), 1 2022.

[91] Spyros Papaefthymiou, Marianthi Bouzouni, and Roumen H. Petrov. Study of carbide dissolution and austenite formation during ultra–fast heating in medium carbon chromium molybdenum steel. Metals, 8(8), 8 2018.

[92] Z. Lv, X. Zhang, X. Huang, and N. Hansen. EBSD characterization of deformed lath martensite in if steel. In IOP Conference Series: Materials Science and Engineering, volume 219. Institute of Physics Publishing, 8 2017.

[93] Chunfang Wang, Maoqiu Wang, Jie Shi, Weijun Hui, and Han Dong. Effect of microstructural refinement on the toughness of low carbon martensitic steel. Scripta Materialia, 58(6):492–495, 3 2008.

[94] S Morito, H Saito, T Ogawa, T Furuhara, and T Maki. Effect of austenite grain size on the morphology and crystallography of lath martensite in low carbon steels. ISIJ International, 45, 2005.

[95] Tadashi Furuhara, Tadachika Chiba, Takeshi Kaneshita, Huidong Wu, and Goro Miyamoto. Crystallography and Interphase Boundary of Martensite and Bainite in Steels. Metallurgical and Materials Transactions A: Physical Metallurgy and Materials Science, 48(6):2739–2752, 6 2017.

[96] Dilip Kumar Singh, Vikram Sharma, Ritwik Basu, and Mostafa Eskandari. Understanding the effect of weld parameters on the microstructures and mechanical properties in dissimilar steel welds. In Procedia Manufacturing, volume 35, pages 986–991. Elsevier B.V., 2019.

[97] Semih Engun, Orhan Uzun, Servet Turan, and Oguz Gunduz. Effect of Grain Boundary Characteristics on the Impact Properties of Thermomechanically Rolled API X70 Pipeline Steels. In 3rd Iron and Steel Symposium, 2017.

[98] Dongying Xu and Hao Yu. Effects of low-angle grain boundaries on the yield-strength ratio of high grade pipeline steels. In Advanced Materials Research, volume 168-170, pages 1581–1585, 2011.

[99] Ningyu Du, Hongwei Liu, Paixian Fu, Hanghang Liu, Chen Sun, Yanfei Cao, and Dianzhong Li. Microstructural stability and softening resistance of a novel hot-work die steel. Crystals, 10(4), 4 2020.

[100] T Anderson. Effect of crack-tip region constraint on fracture in the ductile-to-brittle transition. 1984.

[101] J. A Smith and S. T Rolfe. The effect of crack depth (a) and crack depth to width ratio (a/W) on the fracture toughness of A553-B steel. Journal of Pressure Vessel Technology, 116, 1994.

[102] Paul Kah and Pavel Layus. Influence of alloying elements on the low-temperature properties of steel. In Twenty-fifth International Offshore and Polar Engineering, 2015.